Università degli Studi di Firenze

Dottorato di ricerca in Fisica e Astronomia

Ciclo XXXII

Coordinatore: Prof. Raffaello D'Alessandro

Complete isotopic characterization of projectile fragments in Ca+Ca reactions at Fermi energies with the FAZIA array

Settore scientifico disciplinare: FIS/04 Fisica Nucleare e Subnucleare

Tutori

Dott. Giovanni Casini

Prof. Andrea Stefanini

Dottorando

Dott. Alberto Camaiani

Coordinatore

Prof. Raffaello D'Alessandro

Anni 2016-2019

CONTENTS

INTRODUCTION

Heavy ion collisions in the Fermi energy regime (20-100 MeV/u) allow to explore a various range of phenomena, ruled both by the nuclear mean field contribution and by the nucleon-nucleon collisions, whose contribution increases with increasing bombarding energy [1]. The associated phenomenology is thus extremely rich moving from peripheral towards more central reactions [2]. In particular in peripheral and semi-peripheral collisions it is well known that the exit channel is mainly binary, with two heavy fragments (called QP, for "Quasi-Projectile" and QT for "Quasi-Target", see chap. 1). Moreover, during the primary interaction between projectile and target a diluted neck region is expected to be formed [3] which can be the source of fast emissions and/or can breakup due to dynamical instabilities: particles and fragments emitted from such a region (called mid-velocity emission) show peculiar characteristics, more related with the dynamics of the collision, as for instance the neutron enrichment with respect to the standard evaporation from QP and QT.

Reactions in the Fermi domain can be interpreted in the framework of the nuclear Equation of State (nEoS), which describes the properties of nuclear matter in terms of macroscopic variables such as density, pressure, temperature, volume[1]. In particular two issues are still under study: the dependence of the nEoS on the density and on the nucleonic asymmetry [4, 5]. Heavy ion collisions can be used as a tool to study these topics because once two nuclei collide the nEoS rules the isospin[2] transport phenomena, *i.e.* the motion of both protons and neutrons during the primary interaction throught the neck [6]. Two principal processes are supposed to occur: the first, called isospin diffusion, acts in presence of isospin asymmetry, the second, called isospin drift, arises if

[1]The nuclear Equation of State is a theory made around nuclear matter, *i.e.* an infinite system of nucleons, and thus, once dealing with nuclei, finite size effects can change its properties. For instance, in infinite nuclear matter, the binding energy per particle is 16 MeV whereas it is about 8 MeV in a finite nucleus. Finite size effects, such as surface and Coulomb effects, are properly taken into account in the simulation codes used in this work.

[2]In the literature, especially in experimental papers concerning the study of the isospin related phenomena, the isospin parameter is often defined as N/Z

a density gradient develops. Consequently, once the excited QP and QT emerge after the primary interaction their "chemical" composition is determined by the nEoS. Such effects can survive the QP/QT de-excitation, so the identification both in charge Z and mass A of the produced fragments becomes crucial in order to extract information on the nEoS parametrization.

The present work fits in this landscape exploiting the FAZIA multitelescope array, which represents the "state of art" from the point of view of the isotopic identification of nuclear fragments without using a mass spectrometer [7]. FAZIA is the result of a R&D phase which allowed to push near their limit the identification capabilities of the silicon detectors, reaching the isotopic identification up to $Z \sim 25$ with ΔE-E Si-Si telescopes. By means of four blocks of the FAZIA detector we investigated reactions involving Ca ions, *i.e.* ^{40,48}Ca+^{40,48}Ca at 35 MeV/u: such combinations allowed us to span a rather wide isospin asymmetry, from 1 for the n-deficient reaction, up to 1.4 for the neutron rich nuclei.

The experiment analyzed in this work, the so-called FAZIA-SYM experiment, is dedicated at the investigation of peripheral and semi-peripheral collisions, aiming to the complete isotopic identification of QP remnants. By means of the imbalance ratio method [8, 9], we investigated the isospin diffusion as a function of the reaction centrality, and the consequently neutron-proton equilibration. In order to extract some information about the nEoS, the experimental results have been compared with the prediction of a transport model simulation: we adopted the Antisymmetrized Molecular Dynamics (AMD) [10] coupled with the statistical code GEMINI [11] used as afterburner. For the first time to our knowledge, the same analysis on the isospin equilibration with the imbalance ratio, has been extended in a coherent and homogeneous way, to various QP breakup channels that have shown essentially the same trend of relaxation as a function of the impact parameter. As for the mid-velocity emission, effects compatible with the isospin drift have been evidenced. By means of a detailed analysis of the isotopic composition of fragments emitted in the breakup channels, we explored the possible relationship of the neutron enrichment of a fragment, emitted from the neck, with the associated neutron depletion of the partner. Remarkably, we followed such phenomenon from peripheral collisions to more central ones, highlighting an increase as a function of the reaction centrality.

This thesis is organized as follows: in chapter 1 we introduce the physics case presenting the state of the art of heavy ion collisions in the Fermi energy domain; chapter 2 contains a complete description of the FAZIA multitelescope array evidencing the main features that allowed for the analysis presented in this work. Chapter 3 is dedicated to the description of the FAZIA-SYM scientific goal and to the data reduction; in chapter 4 the theoretical models used in this work are presented, together with isospin sensitive observables adopted in this analysis. Chapter 5 is dedicated to the description of the event selections and to the presentation of the main general reaction characteristics. In chapter 6 the more original results of the analysis are reported and summarized in the conclusions reported at the end of this thesis.

CHAPTER 1

PHYSICS CASE

Heavy ion reactions allow to investigate the properties of the nuclear matter in extreme conditions of temperature and density, depending on the reaction energy domain. For this reason, heavy ion collisions are an important tool to study the nuclear Equation of State (nEoS).

The interaction between nucleons, inside two colliding nuclei, depends on the bombarding energy (E_b/A) and on the impact parameter b (fig. 1.1). At beam energies[1] below $20\,\mathrm{MeV}/u$ the kinetic energy transferred to the nucleons during the collision is low, and the Pauli exclusion principle is very effective[2], thus reducing the nucleon-nucleon collisions and the possibility to populate a nucleon-free state. Moreover, the *de Broglie* wavelength λ of the nucleon inside the projectile is greater than the nucleon average distance inside the target ($R \approx 1.2\,\mathrm{fm}$): consequently, the interaction can be described by means of a mean field theory. The interaction time is relatively long ($\sim 10^{-21}$s) with respect to the nucleus crossing time ($\sim 10^{-23}$s at $20\,\mathrm{MeV}/u$ of bombarding energy) and the complete chemical and thermal equilibrium can be reached. Especially in central collisions, a thermodynamical equilibrated source can be formed, from the fusion of both projectile and target, highly excited and without memory of the entrance channel. This source, called Compound Nucleus (CN), de-excites according to the different statistical weights of the various decay channels available in the phase-space (particle emission, γ-decay or fission). In more peripheral collisions the Deep Inelastic process (DIC) almost saturates the cross section; in this case only a part of the available energy is transferred to the internal degrees of freedom, and the reaction products keep memory of their initial characteristics. The more peripheral the reaction, the less effective the energy dissipation. At the end of the interaction phase two heavy fragments emerge from the reaction, called Quasi-Projectile (QP) and Quasi-Target (QT).

[1] We are considering fixed target experiments where an accelerated ion beam collides on a target material. The experiments at the collider are here neglected.

[2] It is necessary also to add to the incident energy also the energy of the Fermi gas at $T = 0$: this contribution is large, but it cannot be used via nucleon-nucleon collision due to the Pauli blocking.

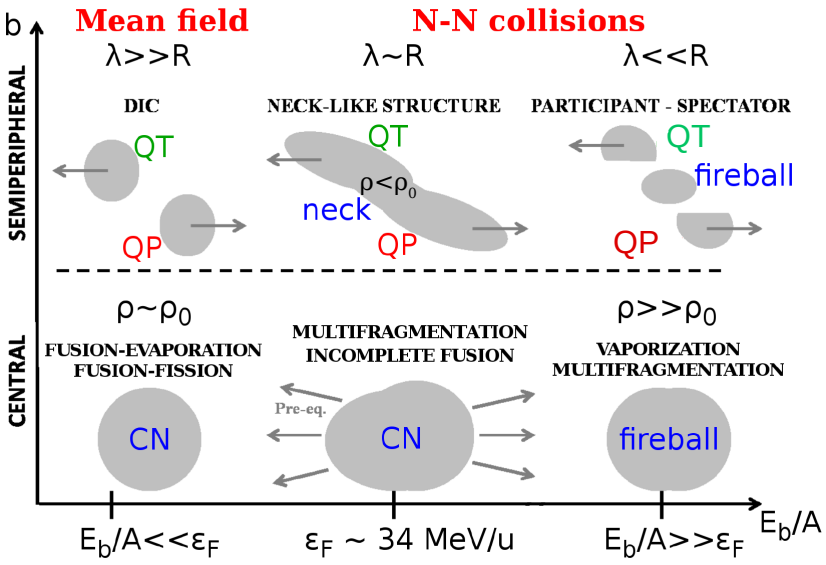

Figure 1.1: *Schematic diagram of the possible evolutions of a nuclear collision depending on bombarding energy per nucleon (E_b/A) and impact parameter b. The relation between the de Broglie wavelenght λ and the average distance R between the nucleons in the nuclei determines the different interactions between the reacting nuclei (mean field or nucleon-nucleon).*

.

On the contrary, at beam energies above 100 MeV/u, the high kinetic energy transferred to the nucleons allows them to reach free states: the Pauli exclusion principle can be neglected and the interaction is largely ruled by nucleon-nucleon collisions (N-N collisions in fig. 1.1). The wavelength λ is smaller than the nucleon average distance inside the nuclei and the nucleon binding energy in the nuclei becomes negligible: the reaction can be schematized as colliding nucleon bunches, according to the "participant-spectator" scenario [1]. The participants form a "fireball" of dense hot nuclear matter which travels at the center of mass (CM) velocity, and then explodes and/or emits energetic nucleons; the spectator pieces (from QP and QT) form less excited fragments which decay by statistical multi-fragmentation or evaporation depending on the reached excitation regime. The region in between these two domains is called "Fermi region"; it represents a transition region and it requires a more complex description. Indeed, both the mean field and the nucleon-nucleon collisions play an important role and features typical of both low and high energy domain appear.

In this work the study of the reactions of ^{40,48}Ca+^{40,48}Ca at 35 MeV/u is presented and therefore more details about the intermediate energy domain will be given in the following, while the scientific goals of this investigation are presented in sec. 3.1

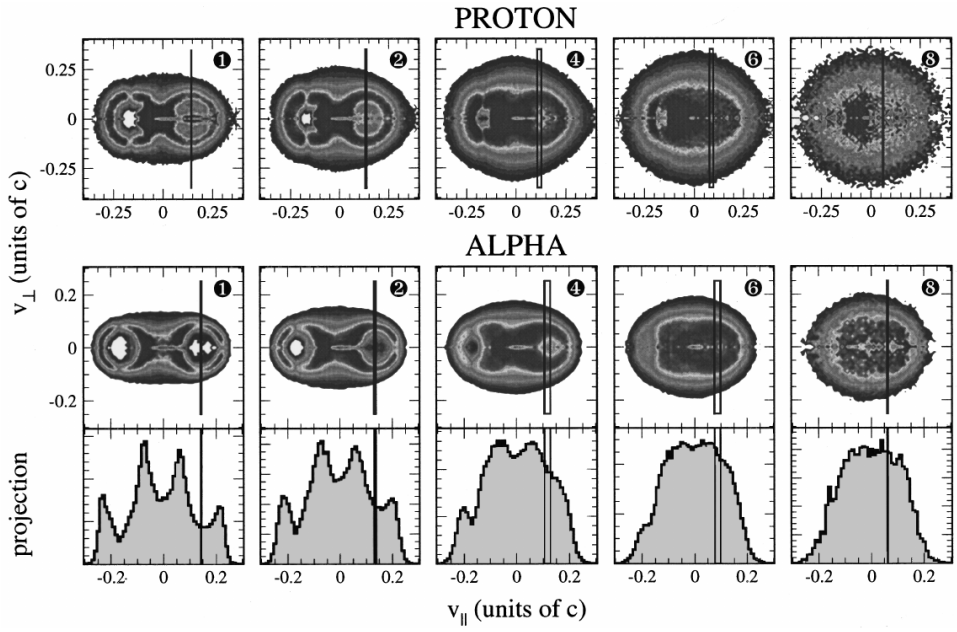

Figure 1.2: *Invariant CM velocity plots for protons (top) and α particles (bottom) for different bins of centrality, from the most peripheral (1) to the the most central (8). Data refer to Xe+Sn at 50 MeV/u. Taken from ref.[2].*

.

1.1 The Fermi energy domain

In the Fermi energy domain the *de Broglie* wavelength is comparable to the mean distance of the nucleons inside the nuclei. Both the mean field interaction and the nucleon-nucleon collision play in determining the collision features. In this regime the interaction times can be of the order or less than those needed to relax several nuclear degrees of freedom and thus the phenomena cannot be interpreted within the general concept of the compound nucleus. For example, the emission of light particles or clusters, can already occur during the interaction of projectile and target when a dinuclear deformed object is evolving. In this case, for instance, the sources cannot be considered spherical nuclei. Moreover, during the interaction, nucleon populations are reorganized in the system and different forces act to lead the system equilibrium from the point of view of the neutron-proton content. If the interaction is very fast, the reaction products re-separate before that chemical equilibrium in the whole system is reached. All above is well represented in many aspects of peripheral and semi-peripheral collisions. Here we well know that the reaction cross section (for not too light nuclei) is almost saturated by the DIC channel, where the formation of a QP and a QT is observed, as in the low energy regime. As the impact parameter becomes smaller the probability of multi-fragmentation increases. If the energy deposited in the central source is above 3.5 MeV/u (see fig. 6 of ref [12]), the system can break down in Intermediate Mass Fragments (multi-fragmentation) then, if the energy deposited is further increased up to 8 MeV/u, in Light Charged Particles (vaporization) [1].

This is clearly represented in the example of fig. 1.2 (taken from an experiment [2] with the INDRA multi-detector) where the protons (top) and α particles (bottom) invariant CM velocity plots for different bins of centrality are shown (see the caption). A QP (pointed out by the rectangle) and a QT sources are visible in the most peripheral collisions, pointed out by the two Coulomb rings corresponding to the emission pattern of the particles mainly[3] evaporated by these sources. Moving towards central reactions, a unique central source arises. Both statistical and dynamical features are present in the decay products of such sources: in particular particles and fragments forward (backward) emitted with respect to the QP (QT) come from the statistical decay of the source, while those emitted towards CM (mid-velocity region) are more linked to the dynamics of the reaction[4].

It is thus clear that once the bombarding energy is fixed, the characteristics of the reaction strictly depend on the impact parameter. In this thesis we aim at following the evolution of Ca+Ca reactions as a function of the reaction centrality so as to proper catalogue different events. For this purpose we will deeply exploit the predictions of the AMD transport model simulation (we postpone to chap. 4 its description) since the impact parameter is not a variable experimentally accessible. In sec. 6.1 the procedure adopted to extract information on the collision violence from the experimental observable is presented.

According to experimental observations [2, 13, 14] and theoretical models [3, 4], an elongated low density region between the projectile and the target, sometimes referred to as "neck", is formed in peripheral and semi-peripheral mechanisms. The neck zone is subjected to fast breakup due to the rise of nuclear mechanical instabilities caused by temperature and pressure effects. Emission of Light Charged Particles (LCP) and Intermediate Mass Fragment (IMF) [13], moving away from the neck also due to the Coulomb repulsion, has been observed in the literature. The remaining excited QP and QT further decay following the statistical weights of the open exit channels.

Independently of the reaction mechanism, the products of the dynamical phase of the collision are called *primary* fragments and they usually are excited fragments. In peripheral and semi-peripheral reactions there are two main fragments (QP and QT) plus neutrons, LCP and/or IMFs, possibly emitted from (or having formed) the neck. We must underline that we speak of excited fragments in a loose sense. Indeed the excitation can be of internal degrees of freedom (*e.g.* the excitation energy of the nucleons within the nuclear potential) or of collective variables (*e.g.* the shape of the nucleus or the rotational energy). In general, in this thesis, we consider the excitation in a general sense, except when specifically indicated. Only by means of a proper simulation one can access to the properties of the primary fragments just at the end of the projectile-target interaction, *i.e.*

[3] A small contribution from pre-equilibrium particle emission can populate the same QP/QT Coulomb circles.

[4] The cross section in a statistical emission is uniformly or, for non zero spin, forward-backward symmetrically distributed in the solid angle. The higher cross section measured in the mid-velocity zone with respect to the statistical forward/backward emission in the QP/QT frame comes from a dynamical component.

when the excited QP and QT emerge after the collision: in sec. 6.4 a procedure exploiting the AMD simulation will be proposed.

The standard statistical decay of a nucleus is modelled according to the Bohr independence principle. According to that, a CN is a systems in internal equilibrium, which has lost the memory of its formation. At the extent that the primary fragments can be considered more or less CNs, their decay can be modeled independent of their origin (cfr. chap. 4). Indeed, their decay towards more stable states is strictly related to their initial properties, i.e. the charge Z, the mass A, the internal excitation energy E^* and the total angular momentum J. By means of the Fermi golden rule the transition probability from the entrance channel to one of the possible final states can be computed, and thus the branching ratios among the open channels can be evaluated [15]. Particles and fragments obtained at the end of the statistical emission are called *secondary* fragments. In any experiment only secondary fragments can be detected due to the relatively long time (nanosecond scale with respect to the emission time scale of at least 10^{-18} s) required to the particles to reach the detectors. For this reason a statistical model is usually employed as "afterburner" to be coupled with the simulation codes describing the dynamical phase in order to obtain model predictions comparable to the experimental data. As mentioned, in this work we adopt AMD dynamical code combined with the GEMINI statistical model (both described in some detail in chap. 4).

1.2 Nuclear Equation of State

Nuclear matter is a theoretical concept assuming an infinite number of neutrons and protons interacting via nucleon-nucleon interaction, which is a residual interaction with respect to the strong interaction among quarks in a nucleon. In that respect, the nucleon interaction can be represented as a Van-der-Waals-like force. The behavior of the nuclear matter in terms of thermodynamic observables (like density, temperature, pressure, volume or isospin) can be described by the nuclear Equation of State (nEoS). In particular, a nucleus in its ground state is a system at temperature $T = 0\,\mathrm{MeV}$ and density $\rho_0 = 0.16\,\mathrm{fm}^{-3}$ (called saturation density). Heavy ion collisions in Fermi energy regime can be though as a path in the nEoS where the system can explore different regions of density and temperature far from the normal ones. Indeed, in the early stage of the reaction (20 fm/c) the system can reach supra-saturation ($\rho/\rho_0 > 1$) densities and then it expands to sub-saturation densities ($\rho/\rho_0 < 1$).

The first attempt to describe a nucleus in macroscopic way was the Bethe-Weizsäcker formula, which, starting from the liquid drop model, describes the binding energy of a nucleus with charge Z, neutron number N and mass $A = N + Z$ [16]. The Bethe-Weizsäcker formula works well for nuclei in the ground state, i.e. in standard condition of temperature and density, but it cannot describe the energy of an excited nucleus.

The nEoS is aimed at describing the energy per nucleon of a nucleus far from ground state conditions. It can be expressed as a function of the density ρ and of the asymmetry

Table 1.1: *Synthesis of the expected values for the nEoS parameters and their associated uncertainties. Values taken from ref. [5]*

P_α	E_{sat} (MeV)	K_{sat} (MeV)	E_{sym} (MeV)	L_{sym} (MeV)	K_{sym} (MeV)
$\langle P_\alpha \rangle$	-15.8	230	32	60	100
σ_{P_α}	$\pm$0.3	$\pm$20	$\pm$2	$\pm$15	$\pm$100

parameter (called also *isospin*) δ, defined as:

$$\delta = \frac{\rho_n - \rho_p}{\rho_n + \rho_p} = \frac{\mathrm{N} - \mathrm{Z}}{\mathrm{A}} \tag{1.1}$$

where ρ_i $(i = n, p)$ are the neutron and proton density with respect to the total nucleon density $\rho = \rho_n + \rho_p$. $\delta = 0$ represents symmetric nuclear matter (N=Z), while $\delta = 1$ defines pure neutron matter. The energy per nucleon can be written as [4]:

$$\frac{E}{A}(\rho, \delta) = \frac{E}{A}(\rho) + \frac{E_{sym}}{A}(\rho)\delta^2 \tag{1.2}$$

The first term represents the binding energy for a symmetric nuclear matter (i.e. $N = Z$); the second defines the symmetry energy.

Both terms are usually expanded in a Taylor series around the saturation density [5]:

$$\frac{E}{A}(\rho) = E_{sat} + \frac{1}{2}K_{sat}x^2 + ... \tag{1.3}$$

$$\frac{E_{sym}}{A}(\rho) = E_{sym} + L_{sym}x + \frac{1}{2}K_{sym}x^2 + ... \tag{1.4}$$

where x is defined as $x = \frac{\rho - \rho_0}{3\rho_0}$. The parameters entering in the expansions are the saturation energy E_{sat}, the incompressibility modulus K_{sat} and high order terms; E_{sym} defines the symmetry energy at ρ_0[5], L_{sym} and K_{sym} the slope and the curvature parameters, plus high order terms. An updated estimation of these parameters is reported in tab. 1.1 (taken from ref. [5]).

The L_{sym} parameter is known with large uncertainties, and today many efforts are spent in order to increase its knowledge. For instance in ref. [17] 28 different analyses of terrestrial experiments and astrophysical observations are summarized aiming at the estimation of L_{sym}. The results of such compilation are shown in fig.1.3. K_{sym} parameter is still unknown. Various experiment are planned to try to shed light on it, mainly looking at the study of the isoscalar giant monopole resonances [5].

[5]It coincides with the symmetry term of the Bethe-Weizsäcker formula [16].

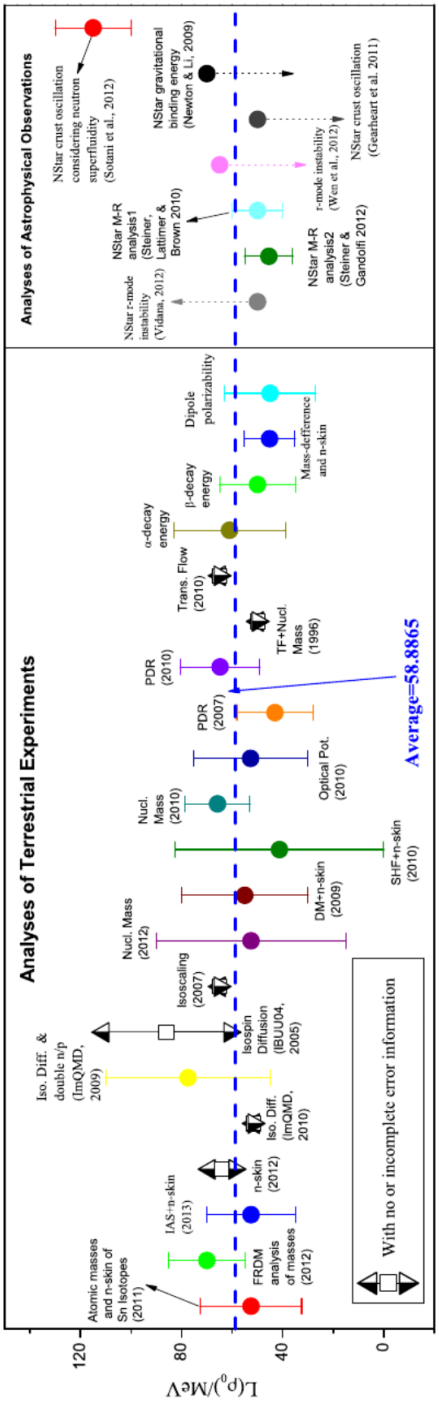

Figure 1.3: *$L_{sym}(\rho_0)$ extracted from 28 different analyses of terrestrial experiments and astrophysical observations. Picture taken from ref.[17]*

.

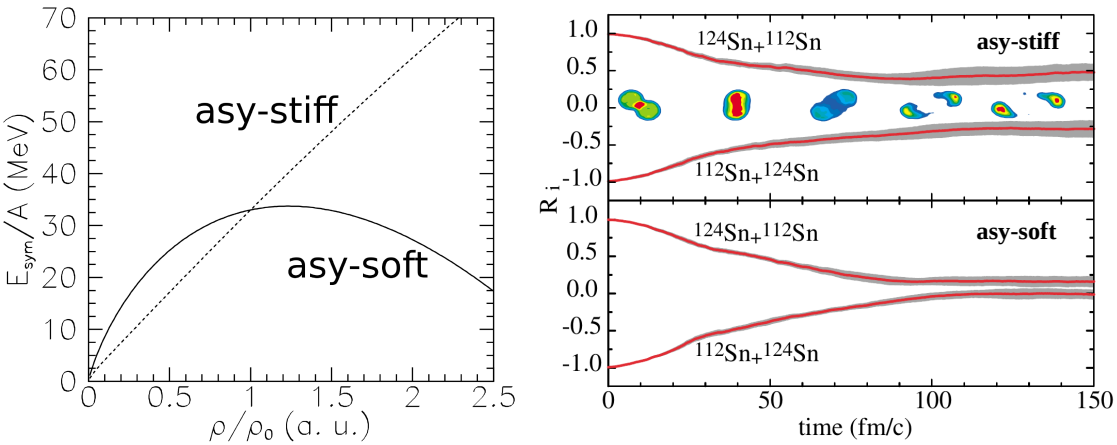

Figure 1.4: *Left Panel: density dependence of the symmetry energy. Two opposite parametrizations are shown: asy-stiff which always increases, as the density increases, and asy-stiff, which decreases for high values of density. Right panel: calculation of n-p equilibration in Sn+Sn collisions due to isospin diffusion as a function of the primary interaction time of the collision, for an asy-stiff (top) and asy-soft (bottom) recipe. No equilibration for $R_i = \pm 1$, full equilibration if $R_i = 0$. Picture adapted from ref. [9]*

.

1.2.1 Isospin transport phenomena

During the collision between two nuclei, the symmetry energy rules the isospin transport phenomena. As already said, in peripheral and semi-peripheral collisions at Fermi energies the reaction evolves mainly through a binary mechanism, which is characterized by the formation of a QP and a QT. Isospin transport phenomena describe the nucleon exchange between the projectile and the target during the dynamical phase. Some old studies on that can be found for instance in ref. [18, 19].

Protons and neutrons, during the collision, experience different forces due to their different chemical potentials [6]. In presence of asymmetry ($\nabla\delta$) and/or density ($\nabla\rho$) gradients, the difference between the neutron and proton currents $\mathbf{j}_n - \mathbf{j}_p$ can be written as [4]:

$$\mathbf{j}_n - \mathbf{j}_p \propto \frac{E_{sym}}{A}(\rho)\nabla\delta + \frac{\partial\frac{E_{sym}}{A}(\rho)}{\partial\rho}\nabla\rho \tag{1.5}$$

i.e. two different contributions to the neutron and proton migration can be distinguished. The first is called **isospin diffusion** and the second **isopin drift** (also known as *isospin migration*). Hence, in presence an asymmetry gradient, mainly the strength of the symmetry energy is tested, while, when density gradients are encountered along the dynamical path, one predicts a drift of neutrons toward the low-density regions, ruled by the derivative of the symmetry energy [6].

Nuclear reactions in the Fermi energy domain are thus a good tool to explore the properties of the symmetry energy, because it is expected that the system explores regions of different density during the collision. The diffusion phenomenon arises in presence of a

difference in the neutron content of projectile and target: for instance, the diffusion of neutrons from neutron rich Sn isotopes towards neutron deficient ones has been observed [9, 20]. The neutron-proton equilibration is sensitive to the behavior of the symmetry energy. To better illustrate this point two parametrizations with different dependence on the density are reported in fig. 1.4 (left panel): an asy-stiff one, which monotonically increases as a function of the density, and an asy-soft one, which decreases at high density values. In particular, we are interested in sub-saturation regions that can be reached in our collision regime. The isospin diffusion following asy-soft parametrization leads the system toward the equilibration of neutron and proton faster than that of asy-stiff one. In the right panel of fig. 1.4 a calculation showing the isospin damping as a function of the interaction time of the collision is reported (taken from ref. [9]) for the Sn+Sn collision. Results referring to two different asy-stiffness of the symmetry energy are shown: an asy-stiff one in the top panel, an asy-soft one in the bottom panel. $R_i = 0$ represents the full equilibration, while $R_i = \pm 1$ the no equilibration line. As the time of the collision increases the system evolves towards the equilibrium. The asy-softer the nEoS, the faster the isospin diffusion equilibration. One of the main goals of this work will be the investigation of the neutron-proton (n-p) equilibration in Ca+Ca collisions. It is important to note that the primary interaction time of the collision is not an observable experimentally accessible. However, the interaction time is related with the impact parameter. As anticipated, in chap. 6 we will try to investigate the n-p equilibration as a function of the reaction dissipation. In particular, thanks to the FAZIA, identification capabilities, we can isotopically resolve up to the QP remnants, and, for the first time, compare the isospin diffusion in such channel with the QP breakup channels (sec. 6.4).

On the contrary, the drift mechanism can manifest, independently to the n-p asymmetry. In particular, as long as the energy of the reaction and the size of the system is large enough, in a binary collision a neck region between projectile and target is formed [2, 13, 14, 21, 22]. Different model calculations predict that the neck region is more diluted with respect to the saturation density [3]. For instance, fig. 6.9 of sec. 6.3, shows the onset of a density gradient, within the AMD model calculation, between the diluted neck and the other regions (at saturation or supra-saturation). According to eq.(1.5) thus a net flux of neutrons towards the neck region is expected, and from the experimental side, a neutron enrichment of fragments compatible with an emission from the neck has been observed [13, 21–24], also in coincidence with the neutron depletion of the donor QP [14, 25]. In the following of this work we will deal with this hot topic, the chance of formation of some neck structure in the Ca+Ca systems, as well as its emission (sec. 6.5), on a experimental ground.

The careful presentation of isospin sensitive observables is postponed in chap. 4, since to properly introduce them we will exploit the simulated data by the AMD transport model.

1.2.2 Neutron stars

As discussed, isospin transport phenomena are then good probes to constrain the parameters of the symmetry energy and an improvement on their knowledge would have also an astrophysical impact. Indeed, the description of the Neutron Stars (NS) is strongly affected by the knowledge of the symmetry energy parameters.

Discovered in 1967 as periodically pulsating sources, Neutron Stars are compact astrophysical objects bound by gravity, where, above density of $\rho \sim 10^7\,\mathrm{g/cm^3}$, the matter density induces electron capture on nuclei and free protons and prevents neutron β-decay [26]. Typical values of mass M and radius R lay at $M \sim 1 - 2\,M_\odot$[6] and at $R \sim 10 - 15\,\mathrm{Km}$. The former can be measured if NS is bound in a binary system, while the second one can be obtained only by means of indirect measurements: thus both measurements can have large errors. The average density of such objects is comparable with the saturation density of the nuclear matter ρ_0. The smaller the NS, the higher the average density. However, in order to stabilize the NS against the gravitational collapse, a steep pressure and density gradient are necessary. Thus, larger central densities are expected with respect to the average NS density. Consequently, NS are super-dense matter, namely nucleons compressed by gravity well beyond the nuclear saturation density.

The neutron star mass and radius and can be obtained solving the Tollman, Oppenheimer, Volkoff (TOV) equations. [27]. The key input to solve the TOV equations is the knowledge of the equation of state of dense matter, $P = P(\rho)$, up to very high density. For instance, under the simple hypothesis of a perfect fluid[7] in a cold ($T = 0$) and catalyzed matter[8], the expected pressure is:

$$P = P(\rho) = \rho^2 \left(\frac{\partial E/A}{\partial \rho} \right) - \rho \frac{E}{A} \tag{1.6}$$

where $\frac{E}{\mathrm{A}}$ is the total energy per nucleon (cfr. eq.(1.2)). Consequently, the NS description is nEoS dependent, and asy-stiff or asy-soft recipe of the symmetry energy can change its characteristics. In particular there is a maximum value for the gravitational mass of a NS that a given nEoS can support. This mass is called the Oppenheimer-Volkoff mass: the maximum mass of a reliable nEoS must be greater than all the measured NS masses. The stiffer the nEoS, the larger the maximum mass.

The impact of different nEoS recipes on the NS characteristics can be seen looking at the $M - R$ diagram, which shows the dependence of the NS mass as a function of its radius. An example of such a diagram is shown in fig.1.5 (adapted from [27]). Each panel shows the variation testing different values of E_{sym}, L_{sym} and K_{sym}, according to the nEoS proposed in ref. [5]. In particular, the softer the nEoS, the lower the NS mass at a given radius. The major effects are due to the L_{sym} and K_{sym} terms, while the effects

[6] $M_\odot$ represent the solar mass of about $1{,}989 \times 10^{30}\,\mathrm{kg}$

[7] This assumption has been already done for to derive the TOV equation.

[8] The ground state (minimum energy per baryon) of a system of hadrons and leptons with respect to their mutual strong and weak interactions at a given total baryon density ρ and temperature T[28]

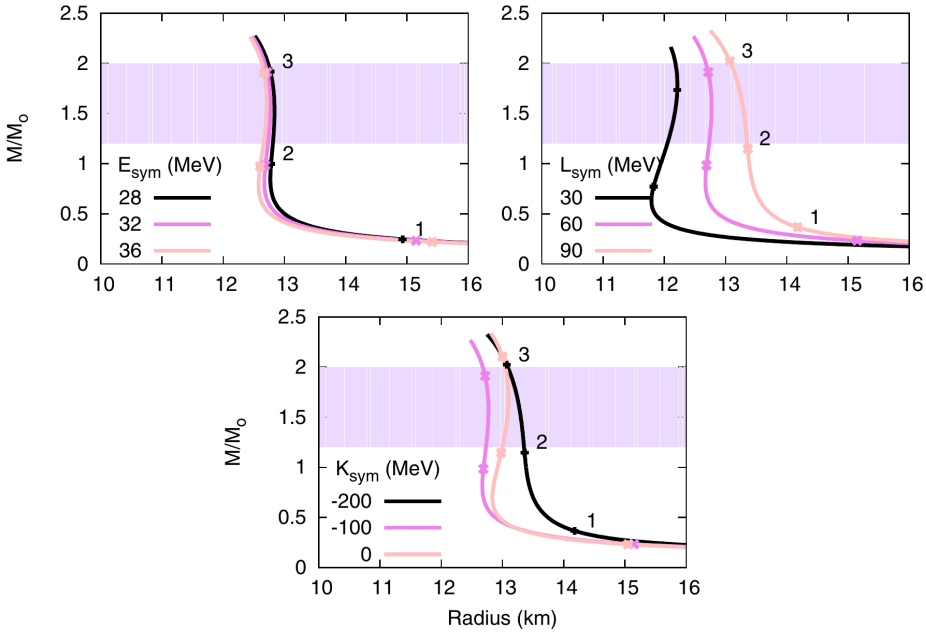

Figure 1.5: *Mass-Radius diagram with the nEoS recipes proposed in ref.[5, 27], varying the parameters of the symmetry energy. Picture adapted from ref. [27]. See ref. [27] for more details.*

.

of E_{sym} are quite small (also because the uncertainty on this parameter is rather small compared to the others). The uncertainty of L_{sym} leads to an uncertainty of about 2 km at low NS mass, 1 km at high NS mass; the effect of K_{sym} is also quite large: about 1 km at low NS mass and 500 m at high NS mass [27]. Consequently, such observations justify the interest around a reliable nEoS, as its understanding allows a better description of NS.

CHAPTER 2

THE FAZIA MULTITELESCOPE ARRAY

FAZIA (*Forward-angle A and Z Identification Array*) is an experimental apparatus for charged particles dedicated to the isotopic identification of fragments produced in nuclear reactions in the Fermi energy domain. It is a portable and modular detector, in order to measure in various laboratories and to be coupled with other experimental apparatuses. A FAZIA module, called "block", is based on three stage ΔE-E telescopes fully readout by digital electronics. A block consist of 16 telescopes, organized in a 4×4 matrix, as shown in the rendering of fig. 2.1.

The FAZIA telescope is made of two silicon detectors with thickness ∼300 μm and ∼500 μm, followed, as third stage, by a Cesium Iodide doped with Thallium 10 cm thick. In the following, the telescope stages are labelled Si1, Si2 and CsI, respectively. A single telescope has an active surface defined by the Si1 area of 2×2 cm^2, therefore the whole block covers approximately 8×8 cm^2 (a solid angle of 0.01 sr at 80 cm far from target). As shown in fig. 2.1, all the electronics is located near the detector. This choice has been done for two reasons: first, to avoid signal distortion due to the cable length, second, to realize a very modular and transportable detector where both the detectors and all the electronics are grouped together and placed in vacuum, minimizing the connections needed between the vacuum chamber and outside. In particular the preamplifiers, the digitizing and the shaping electronics are bundled inside a FAZIA block (cfr. Sec. 2.1.2).

After an R&D phase, starting from 2015 the FAZIA collaboration performed a series of experiments at the INFN Laboratori Nazionali del Sud (LNS) with a FAZIA demonstrator made by four, up to six, blocks. The first experiments were ISO-FAZIA (^{80}Kr+^{40,48}Ca at 35 MeV/u) [30] and FAZIA-SYM(^{40,48}Ca+^{40,48}Ca at 35 MeV/u), followed by FAZIA-COR(^{32,36}S+^{12}C at 25,50 MeV/u) in 2017. More recently in 2018, a six block configuration was mounted, and used in the FAZIA-PRE (^{40,48}Ca+^{12}C at 25,40 MeV/u) experiment. The conclusion of LNS campaign was the FAZIA-ZERO(^{12}C+^{12}C at 62 MeV/u) experiment in collaboration with the Isao Tanihata group in July 2018. In this period, different physics topics have been covered, starting from the study of the QP break up

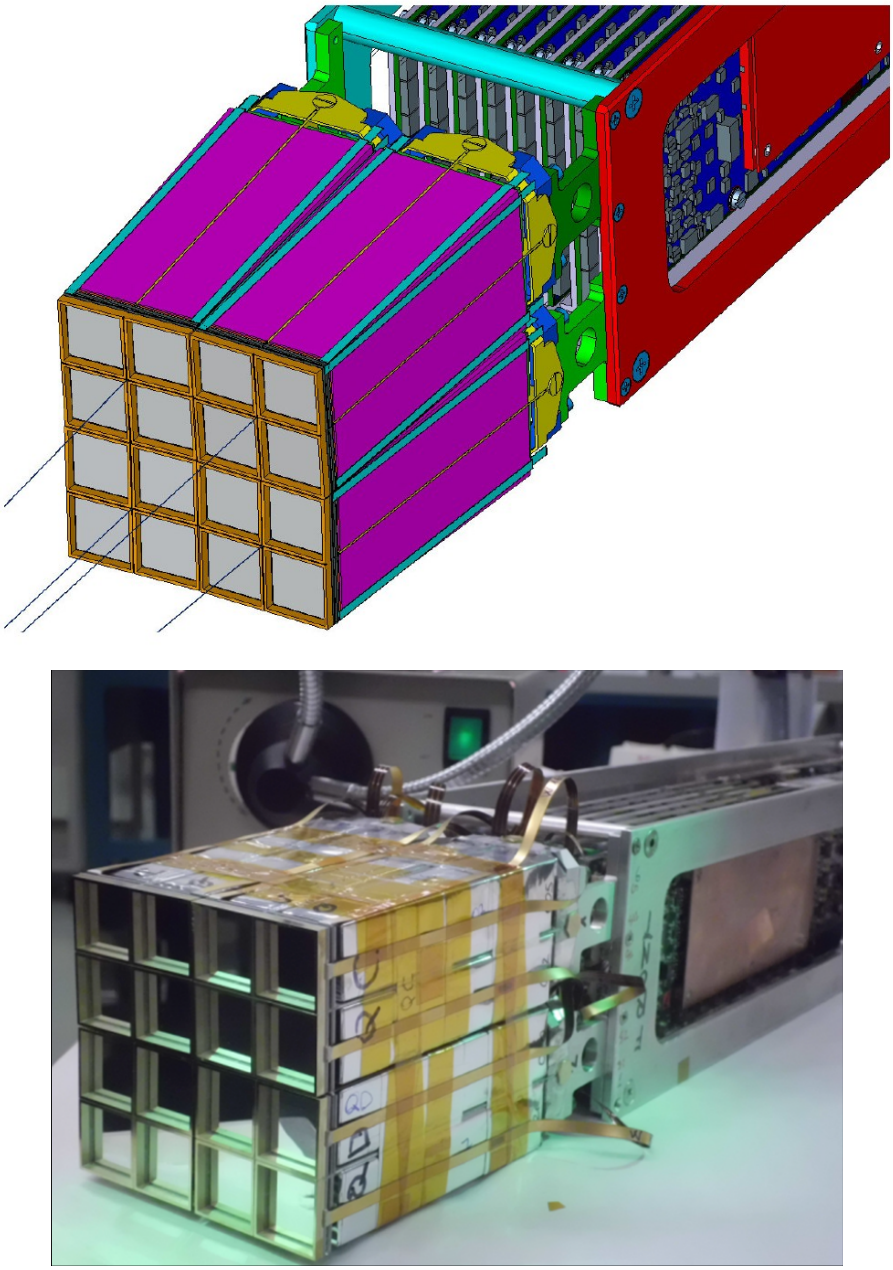

Figure 2.1: *Rendering and picture of a* FAZIA *block. The detectors are connected to the preamplifier inputs by means of flexi cables clearly visible in the picture. The rendering is taken from [29].*

(ISO-FAZIA) to the decay of light cluster in-medium (FAZIA-COR), up to the ^{12}C cross section measurement of the FAZIA-ZERO experiment. In the meanwhile the full FAZIA apparatus (*i.e.* 12 blocks) has been completed, and it is now in operation at GANIL coupled with the INDRA multidetector [31], with a scientific program which will cover the period 2019-2022. In the INDRA-FAZIA configuration, FAZIA aims to isotopically resolve the QP-like fragments, covering the forward angles in the laboratory frame (between 2° and 14°) while INDRA with its large angular coverage (17° and 175°) allows to characterize the centrality of the reaction.

This thesis concerns about the FAZIA-SYM experiment. Before entering into details of the analysis, and of the procedure needed to calibrate and identify fragments and particles, the apparatus characteristics, at the basis of the FAZIA identification performances, will be presented.

2.1 The FAZIA apparatus

During the FAZIA R&D phase the main efforts to improve the identification capabilities of a Si-Si-CsI telescope followed two principal paths: the detectors performances (mainly regarding silicon ones) and the digital treatment of the signal induced by the ionizing particle in the detectors. The main goal was to extend the charge and mass separation of the identification methods, ΔE-E and Pulse Shape Analysis (PSA) techniques[1].

Before moving to the complete description of the FAZIA apparatus, a brief explanation of the identification techniques of the reaction product is appropriate, in order to help the reader in the comprehension. The ΔE-E method is based on in the correlation of the energy deposited in two consecutive detectors: ΔE is the energy deposited in the first active layer, E is the energy deposited in the second one, in which the fragment is stopped. Fragments which stop in the first silicon detector can be identified by means of PSA technique [32], exploiting the information directly extracted from the shape of the induced signal in the detector. The FAZIA collaboration investigated two implementations of PSA for fragments stopped in the silicon layers: the first is the correlation between the rise time of the charge signal and the energy deposited in the detector; the second is based in the correlation of the maximum of the current signal and the energy. A different kind of PSA, mainly useful for the most penetrating light particles (namely Z =1-3), is obtained from CsI crystals.

The signal digital treatment allows considerably improvements in the PSA performances, which requires to extract information directly from the induced signal. Dedicated signal processing can be investigated and applied, not easily (or not at all) implementable with analog electronic.

[1] During the LNS period the FAZIA block have been locate at 80 cm from the target, in order to obtain a sufficient solid angle coverage. This choice discourages the use of the time of flight techniques.

2.1.1 The detectors

Any kind of effect that can spoil the energy resolution also affects the ΔE-E identification capabilities. Analogously, any kind of effect that introduces fluctuations, in the signal shape of ions with the same energy stopped in Si1, worsen the PSA performances. For such reasons many efforts have been spent in order to investigate the parameters to be controlled during the detector construction, with the aim to reduced fluctuations affecting the identification techniques.

First, and obviously, silicon detectors with low point-to-point thickness variation are required to build a good Si1-Si2 telescope: the more homogeneous the thickness, the more constant the energy deposition in the ΔE stage varying the impact position on the telescope. FAZIA silicon detectors have a thickness uniformity of $\pm 1\,\mu$m. Second, dead layers have to be kept low, in order to avoid undesired energy losses, with the correlated energy fluctuations (energy straggling). Third, in crystalline detectors ions tend to follow the direction between two neighboring crystalline planes and/or axes, but at the largest possible distance from each of them: they travel in "channels"[33]. If ions impact on crystal with a pronounced crystallographic symmetry, their range and stopping power (*i.e.* dE/dx) fluctuate. Such channeling effect spoils the experimental energy resolution: in order to avoid it, during the manufacture, the silicon detector are obtained by slicing the parent ingot following specific cutting prescriptions, so as to reduce at minimum the probability of channeling for ions entering perpendicularly in the front face of the final pads [34, 35]. Moreover, in refs [34, 35], it has been shown how channeling effect can affect the signal shape, thus the "random cut" is useful also for the PSA identification performances. With an appropriate careful geometrical mounting, coupled to the aforementioned special cut (random cut), the FAZIA silicons present negligible channeling ion trajectories subtended by their dimensions.

The details of the signal development in Si detectors, strictly related to the charge collection times, are affected by local inhomogeneities of the electric field generated in the diode by the applied voltage. These inhomogeneities are for example due to variations of doping concentration (*i.e.* resistivity) in the material bulk. Therefore silicon detectors with a good dopant homogeneity are required, in order to have a resistivity as much homogeneous as possible in the whole active volume [36]. Indeed, as said, a local variation of the electric field induces different collection times (and thus e.g. the measured risetime), thus jeopardizing the identification performances once the full active area is used. Therefore, the FAZIA collaboration imposed strict constraints on the original ingot resistivity. Typically the best values in term of homogeneity of the resistivity is reached using neutron transmutation doping (nTD) technique. Indeed, most of the sensors mounted in the present telescopes are made of nTD-based silicon pads, allowing inhomogeneities below 5-6% (in most cases better than 3%). This subject resulted to be so important that a non-destructive technique has been implemented by the FAZIA collaboration, based on fast-UV laser pulses[37], in order to verify (randomly) the compliance of the produced pads with the requested values. Another issue that has to be taken under control is the sheet resistance of the silicon detector: in order to minimize it and preserve good timing

properties, an aluminum layer of about 30 nm has been deposited on both sides. We note that the introduction of these very thin dead layers has negligible effects on the energy resolution.

It's worth mentioning that during the data acquisition, the silicon reverse currents are constantly monitored, so as to correct for the increasing voltage drop across the pre-amplificator bias resistance, in order to keep constant the electric field inside of the detector during the whole experiment, permitting to keep constant also the shape of the signal induced in the detector by the impinging particle (Z, A, E) during the whole experiment.

All these efforts can be summarized in what is called "the FAZIA recipe" of the silicon detectors (see ref. [7] and references therein for further details):

- high thickness uniformity ($\pm 1\,\mu$m);
- very low dead layers;
- the detectors obtained cutting the silicon wafer along a direction tilted with respect to the major crystal axis;
- nTD silicon detectors, with a bulk resistivity in the range 2000-3000 Ωcm, in order to obtain non-uniformities ranging from 1% to 6%;
- an aluminum layer of about 20 nm deposited on both sides, enough to ensure very low resistance thus preserving good timing properties, but being at the same time very thin to not introduce dead layer effect;
- during an experiment, online and control of the silicon reverse current as a function of time and its correction, maintaining constant the applied voltage to the diode.

The CsI detectors have a shape close to that of a parallelepiped, with a slight tapering requested by the design distance from the target (optimized to be mounted at 100 cm from the target). They are 10 cm thick with a Tl doping uniformity along its main direction ($\pm 5\%$). Their front face is protected by a reflecting alluminized Mylar foil (1.5 μm thick) while the lateral wrapping consists of a purposely shaped foil of high reflecting polymer (ESR Vikuiti, 3M) finally tightened by an opaque tape. They are directly coupled with PhotoDiode made by CIS [38] and FBK [39] company, with an overall area of $2.17 \times 2.17\,\text{cm}^2$, for a proper matching with the detector back side, and an active area of $19 \times 19\,\text{mm}^2$.

2.1.2 Front End Electronics and Acquisition

All the electronics needed for the extraction of the information from the detectors is embedded in the proximity of the telescope inside the vacuum chamber. A schematic view of the FAZIA electronics and acquisition is represented in fig. 2.2 (taken from [29]). The detectors are directly connected with flexi cable of about 15 cm length to the Front End

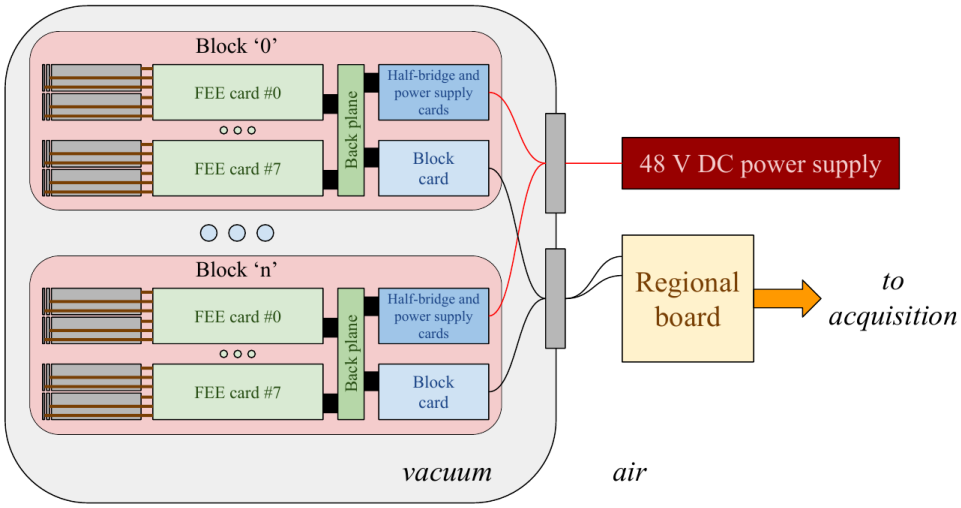

Figure 2.2: *Schematic representation of the* FAZIA *blocks with associated electronic cards inside and outside the scattering chamber. Figure taken from [29].*

Electronics (FEE) cards. Each FEE drives two telescopes (*i.e.* six detectors), supplying the high voltage for the detectors and digitizing the signals. By means of a Back Plane bus the FEE cards are connected with three modules named "Block Card", "Half-Bride" and "HV": the former manages input/output operations and merge data from the FEE; the others produce and monitor the voltages needed to the FEE, pre-amplifiers and detectors on the blocks. Only two connections per block are required to communicated outside the scattering chamber. The first concerns the data I/O and slow control: it is done by means of a two way optical fiber which connect each Block Card to the so-called Regional Board (ReBo), which manages the "event building" and the acquisition (see sec. 2.1.4) and the slow control commands. The second is a connection with a 48 V (6 A) power supply to produce the voltages needed to the boards on the blocks.

Since a single FAZIA block absorbs almost 300 W, a very efficient cooling solution is required to operate under vacuum. The adopted solution consist of a 8 mm thick copper plate, on which all the cards are screwed on. The copper plate has been designed in order to efficiently distribute the liquid flow along the entire surface which holds the the 8 FEE cards. The refrigerate water (with 30% alcohol or glycol) is distributed by a powerful chiller (ACW LP60) and flows through all the blocks. With such expedient the temperature of the electronic components are kept below 60°C.

The FEE cards are the core of the FAZIA block featuring the various stages for the signal processing. Each FEE card contains six Charge Sensitive Preamplifiers (CSP), three per telescope, connected with the three stages of the telescopes. For the three telescope layers the signal treatment is different at the output of the respective CSP. In particular we have three channels for the Si1 stage which gives the richest information: a high range charge channel (QH1), low range charge channel (QL1) and a current channel (I1). We

then have two lines for the Si2 stage: high range charge channel (Q2) and current channel (I2). The CsI stage has only a charge channel (Q3), which then is shaped by means of two trapezoidal filter, with different set of parameters, in order to get the parameters for PSA purposes. In the following, the parameters extracted by shaping the signals of each channel are labelled with proper subscript: for instance $Q3_{slow}$ and $Q3_{fast}$ refer to parameters extracted with a slow and fast filter (see sec. 2.1.3 for more details related to the signal shaping). Both I1 and I2 are obtained by an analogue differentiation of the CSP output, of the Si1 and Si2 stage respectively. The full output dynamics of the CSP is 8 V and must be accommodated to match that of the fast sampling ADC (2V). More precisely, the high range channel (4 GeV for Si1 and Si2), which preserves the complete CSP dynamics, includes a 4x attenuation; instead, the low range channel (only for Si1) is amplified by a factor 4, to obtain more precise information for low energetic particles (up tp 250 MeV). A similar 3x amplification is needed also for the current signals.

Two ADCs with different specifications are present in the FEE card. The first, dedicated to the high range channels and to the CsI charge channel, has a sampling frequency of 100 MS/s with 14 bit resolution and around 11.4 ENOB (Effective Number Of Bits)[2]; low range and current signals are sampled by a 14 bit, 250 MS/s (11.2 ENOB). The sampling at higher frequency and with good resolution of the QL1 allows for excellent timing performances and, in general, for preserving the signal shape.

The sampled signals are read out by two Field Programmable Gate Arrays (FPGA). The FPGAs perform a real time digital filtering of the signals, in order to obtain triggers and energy loss information from each detector. While the trigger information is continuously send by the FEE, the full digitized signal and the on-line calculated energy is sent only when an event validation is transmitted by the ReBo to all the blocks (cfr. sec. 2.1.4). The signal shaping will be described in sec. 2.1.3.

The Block Card manages the communications, both with the FEE cards and with the ReBo. In particular, the collected data from all the eight FEE cards are sorted, so as to build a partial event before the transmission to the ReBo via optical fiber. The ReBo is a VME card and it can manage up to 36 blocks. Its main task is to handle the information coming from every FAZIA blocks completing the event, analyze triggers and send back to the blocks validations signals. The trigger production, event building and how the ReBo manages the coupling of FAZIA with other detectors will be described in sec. 2.1.4. Also the slow controls (e.g. trigger thresholds, HV settings) pass through the ReBo, and they are sent to the single detectors through the Block Card and the bus connection using a dedicated software (FAZIA-GUI).

[2]The Effective Number Of Bits is a quantity which takes into account the effective noise variance (σ^2_{eff}) of an ADC. An ideal ADC, with a number N of bits, produce 2^N output codes. However, the digitizing process introduces a quantization error which is usually described as a white noise, with a variance $\sigma^2 = \frac{1}{12}(\frac{R}{2^N})^2$, where R is the ADC range in Volt. Moreover, the ADC analog input noise and the aperture time jitter also contribute to the total noise level of the ADC, thus further reducing the ADC dynamical range. The ENOB are defined as the effective number of bits which reproduces the effective ADC noise variance: $\sigma^2_{eff} = \frac{1}{12}(\frac{R}{2^{\mathrm{ENOB}}})^2$, where ENOB $< N$.

2.1.3 Digital treatment of the signals

The FAZIA collaboration adopts both online and offline signal processing to extract the information required for the ΔE-E and PSA methods. However, at the time of the FAZIA-SYM experiment, the second experiment after the end of the R&D phase, the implementation of the signal shaping on board of the FPGA was not completely trustworthy especially for the CsI channels, and so on this analysis only results coming from the off-line analysis are used. The signal length and the signal portion used to estimate the baseline (BL) amplitude are reported in tab.2.1: in particular, also the characteristic of the adopted off-line filter are reported.

Table 2.1: *Signal length and signal portion used to estimate the base line amplitude of the digitized waveforms for each channel; parameters extracted with the trapezoidal filtering, as well as the filter parameter.*

Type	Signal Length	BL Length	Parameter	Flat top	Rise Time
QH1	5120 ns	500 ns	$\mathbf{QH1}_{max}$	1 μs	2 μs
QL1	2048 ns	50 ns	$\mathbf{QL1}_{max}$	1 μs	2 μs
Q2	5120 ns	500 ns	$\mathbf{Q2}_{max}$	1 μs	2 μs
Q3	5120 ns	500 ns	$\mathbf{Q3}_{slow}$	10 μs	0.7 μs
Q3	5120 ns	500 ns	$\mathbf{Q3}_{fast}$	0.5 μs	0.7 μs
I1	2048 ns	200 ns	-	-	-

The energy information from the charge signals is obtained in the following way. Using the first portion of the signal the baseline amplitude is evaluated and subtracted from each signal sample [40]. Then the signal is shaped by means of a trapezoidal digital filter and the deposited energy is evaluated as the filter output maximum (for instance $QH1_{max}$ in tab.2.1). It has been found that for the charge signal of the Si layers, the trapezoidal filtering parameters of tab.2.1 guarantee good energetic resolution. For the scintillation signal from the CsI crystals two digital filters (with different rise time and flat top values) must be applied to obtain the desired information. It includes the total deposited energy (as for Silicons) associated with $Q3_{slow}$ and the fast scintillation component ($Q3_{fast}$) necessary to exploit the PSA capability of these inorganic scintillators, as deeply explained below in sec 2.2.2. All the flat top values are set according to the slowest acquired signal in order to avoid ballistic deficit; no pole-zero cancellation is applied, anyway its effect was found to be negligible since the preamplifier constant decay (approximately 260 μs) is much longer than the flat top.

Today, the trapezoidal filter can be implemented on board to the FPGA in the FEE cards, allowing to perform the online signal shaping. Such choice allows to store only the extracted energy information without store the whole signal, thus saving storage space on disc and time during the acquisition, thus decreasing the time in which the apparatus can not receive trigger (see sec. 2.1.4). No differences between the online and offline shaping have been found.

For what concern the information needed to the PSA techniques, the FAZIA collabo-

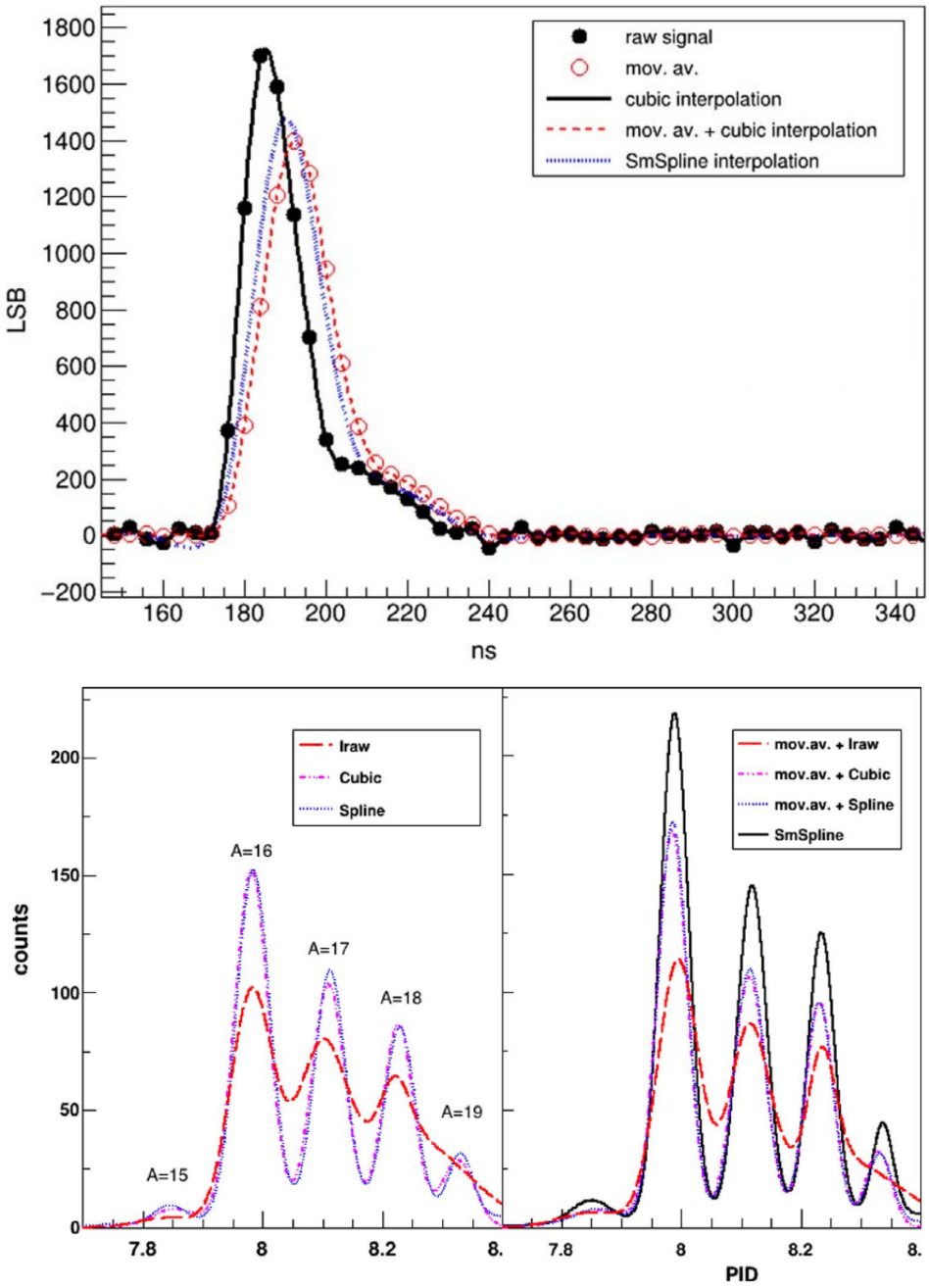

Figure 2.3: *Top) Effect of the smoothing spline interpolation on the raw signal. Bottom) Effect of the various algorithms to estimate the maximum of the current signal on the fragment identification. See the legend for the interpretation. Figure taken from [41].*

ration adopts interpolation methods to extract the charge signal rise (e.g. $QH1_{trise}$) time and the maximum of the current signal ($I1_{max}$). In particular for the extraction of $I1_{max}$, this choice allows to enhance the identification capabilities of PSA methods with respect to the simple search of the maximum sample among the digitized ones. In more details, the collaboration studied various methods in order to get the the maximum of the current signal [41], in order to optimize the identification performances. The adopted procedure consist of a smoothing spline interpolation [42], which uses a spline curve continuous up to the second order derivative [43]. The effect of the smoothing spline interpolation (Sm-Spline) is visible in the top panel of fig. 2.3, where both the raw signal (black circles) and the signal after the interpolation procedure (blue dashed) are shown. This algorithm is not a pure interpolation method, as the interpolated signal does not necessarily pass through the original samples: the smoothing spline interpolation incorporates a moving average filter to reduce the noise fluctuation[3]. Indeed, the smoothing behavior is similar to that of the moving average filter (red open circles). In ref. [41] the enhancement of such procedure with respect to different ones is shown. The effect of the three algorithms is shown in the bottom panel of fig. 2.3, where the Particle Identification distribution (PID, cfr. sec. 3.3.1) is quoted for the Oxygen isotopes. The smoothing spline algorithm give the better isotopic resolution (lower width for each peak with respect to the other methods) and thus has been adopted as standard method for the Si1 PSA. However, the implementation of the chosen interpolation on board of the FPGA is not an easy task, thus the off-line analysis, at today is still mandatory.

2.1.4 The FAZIA trigger

The FAZIA trigger is based on a three step procedure. First, for each telescope a "local" trigger is continuously built by means of an online (on board to the FEE cards) fast trapezoidal filter with 200 ns of both flat top and rise time. A logical signal is produced when the output filter maximum is higher than a threshold: this is called "fast threshold" and can be set by the user. Logical signals from Si1, Si2 and CsI are combined, usually in OR configuration, to create the "local" trigger for each telescope.

Second, for each block the "local triggers" are counted by the Block Card and sent, every 40 ns, to the ReBo. Inside the ReBo the "global" trigger is generated taking into account all the "local" triggers coming from all the Block Cards, which can be combined together requiring for multiplicity conditions and imposing different down-scale reductions.

Finally, the ReBo, checks if there are any alerts coming from the FEE cards, as for instance if the FPGA data buffers are almost full. If there is at least one, a veto flag is issued ("veto out"). On the contrary, if there is a "global" trigger without any veto flag, the ReBo sends a validation signal to all the telescopes with the following effects:

- if the telescope has not generated the "local" trigger and no one of its detector

[3]The moving average is a Finite Impulse Response (FIR) filter which is optimal to reduce the white noise superimposed on the signal, while at the same time keeping the sharpest step response

has passed the slow filter threshold, the telescope is not acquired (zero-suppression, applied for the whole telescope);

- if the telescope has not generated the "local" trigger but at least one detector has passed the slow filter threshold, all the detector signals are acquired;

It's worth mentioning that FAZIA can manage external triggers, working in a "slave" mode, so as to generate the validation signal once an external trigger is on and there are no veto flags. The ReBo manages also the coupling of FAZIA with other detectors: in particular it features some programmable auxiliary connection equipped with the CENTRUM technology [44] to synchronize events coming from different detectors.

As an example, we can illustrate the current coupling of FAZIA with the INDRA multi-detector [31]. From the acquisition point of view [29], the FAZIA coupling with INDRA (more generally with other detectors) is done at different levels. The first is the trigger level: for the INDRA-FAZIA campaign it has been chosen to work in a common dead time mode. This is achieved by properly interconnecting the trigger in/out[4] and veto out connection (see fig. 2.4): in this way neither FAZIA nor INDRA produce a validation signal while the other apparatus is not ready. The generation of a common time-stamp is the second step of the digital acquisition coupling. When a validation is produced, the CENTRUM system dispatches to all the detectors a frame containing a timestamp to label the event. The FAZIA ReBo inserts this timestamp inside the event frame that is sent to the acquisition. Finally, as third step, the NARVAL acquisition system [45] receives data both from INDRA and FAZIA: it recognizes CENTRUM timestamp, merging sub-events with the correct time stamp interval, approximately within 1 μs.

Of course, FAZIA can be coupled with other detectors than INDRA, as long as they supports both CENTRUM and NARVAL. Moreover, both CENTRUM and NARVAL technologies support connection with many apparatus, so FAZIA can be coupled in future with more than one detector.

2.2 Identification techniques

For the completeness of the thesis, in this paragraph we will remind the physical background of the identification methods and we will demonstrate their application through examples referring to the data of the experiment FAZIA-SYM, here discussed.

In particular, FAZIA exploits two different techniques for the fragment identification: ΔE-E method via Si1-Si2 and Si2-CsI telescopes and PSA in Si1 and CsI detector. Moreover, the use of the conventional "energy *vs.* time of flight" method for mass identification of ions stopped in first silicon layer (as done by the CHIMERA collaboration but with analog electronics [46, 47]) is currently under investigation (see ref. [29, 48]) but still not implemented. Some preliminary results obtained in the FAZIA-PRE experiment show that with the proposed version of the time of flight techniques is possible, with respect

[4]The trigger out is true where there is a "global" trigger and no veto flag.

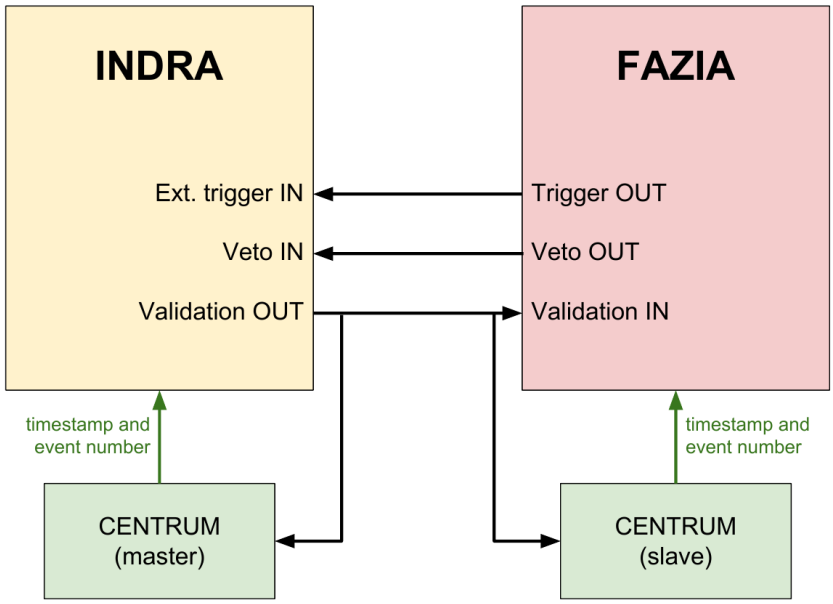

Figure 2.4: *Scheme of the INDRA-FAZIA acquisition. The validation signal coming from INDRA (master) is used to validate* FAZIA *(slave). The timestamp, needed for the event reconstruction, is assigned by the CENTRUM. Picture take from [29].*

to the PSA techniques, to disentangle Hydrogen ions, while for heavier fragments the isotopes separation is comparable. We are not using this techniques in this thesis and we do not mention it anymore.

2.2.1 ΔE-E method

ΔE-E method is based on the correlation of the fragment energy losses in two consecutive active layers, in order to extract its charge and, possibly, mass. Indeed, the energy loss of a fragment with atomic number Z, mass A, and velocity v, through a material with electron number density n and mean excitation potential I, can be expressed by means of the Bethe-Block formula [36]:

$$\frac{dE}{dx} = \frac{4\pi}{m_e c^2}\frac{nZ^2}{\beta^2}\left(\frac{e^2}{4\pi\varepsilon_0}\right)^2 \cdot B \tag{2.1}$$

where

$$\beta = \frac{v}{c},\ n = \frac{N_A\, Z_{abs}\, \rho}{A_{abs}\, M_u} \text{ and } B = \ln\left(\frac{2m_e\, c^2\, \beta^2}{I(1-\beta^2)} - \beta^2\right)$$

N_A is the Avogadro Number, ρ the absorber density, the Z_{abs} and A_{abs} the atomic and mass number of the absorber, M_u the atomic mass unit, m_e and e the electron mass and charge.

At non relativistic energies as those we are interested in, eq. (2.1) can be simplified

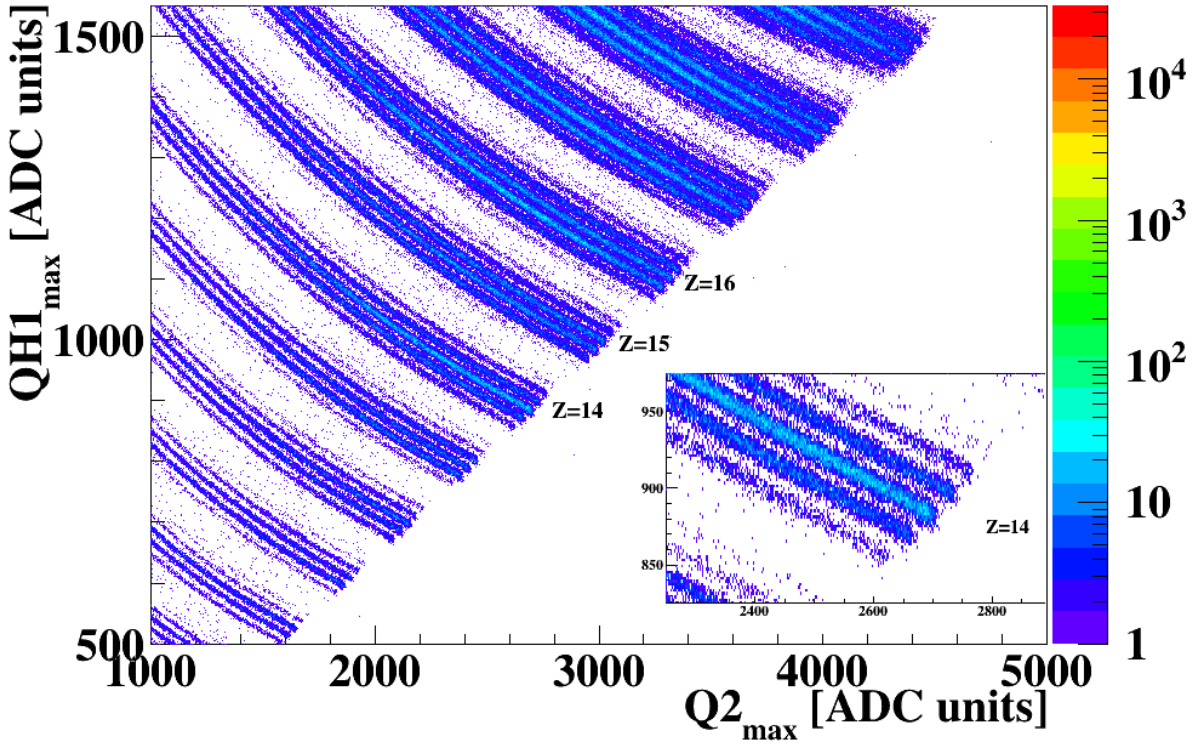

Figure 2.5: *Typical Si1-Si2 ΔE-E matrix of a* FAZIA *telescope. Isotopes which punch through the Si2 stage are not reported, vetoing on the CsI signal. A clear Z and A separation is visible. In the sub-panel the silicon isotopes are shown. Data refer to the* $^{48}Ca+^{48}Ca$ *reaction of the* FAZIA-SYM *experiment.*

in the following way:

$$\frac{dE}{dx} \propto \frac{Z^2}{\beta^2} \propto \frac{Z^2\,A}{E} \tag{2.2}$$

where E is the kinetic energy of the incident fragment, respectively. Thus, as we can deduce from eq. (2.2), correlating the energy loss in two consecutive detectors of a telescope, the detected fragments will be grouped in regions depending on $Z^2\,A$. The isotopic resolution of the fragments is strictly related to the energy resolution of the detector employed in the telescope, mainly to the ΔE stage. In this sense strict specifications about the production of Si1 and Si2 detectors, summarized in the FAZIA recipe, are essential to the quality of the fragment identification, since the silicon layers are the ΔE pairs of Si1-Si2 and Si2-CsI telescope, respectively.

A Si1-Si2 ΔE-E matrix is shown in fig. 2.5: the data refer to the ^{48}Ca+^{48}Ca reaction of the FAZIA-SYM experiment. The loci related to silicon, phosphor and sulfur ions are indicated: in the sub panel, all the silicon isotopes are clearly separated. During the R&D phase, it was demonstrated that the charge separation can be extended with our telescopes up to Z=55, well beyond the range accessible with the present experiment. As

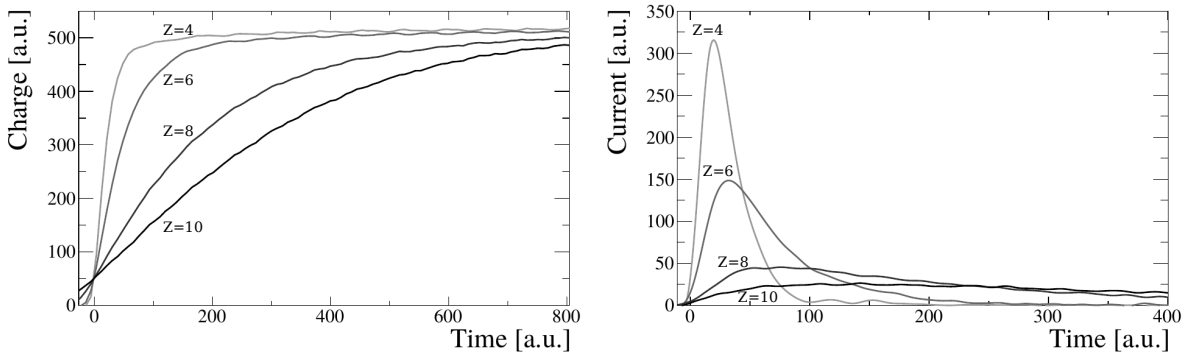

Figure 2.6: *Experimental signals coming from Si1 for different ions (Z=4, 6, 8 and 10) at 95.5 MeV. In the left (right) panel the acquired charge (current) signals are shown. Adapted from ref. [54].*

for mass identification the limit was found to be up to Z=25 [7]. The applicability of the DΔE-E method has of course limits. Towards the low-energy ions, there is the natural threshold corresponding to the punch through of the first layer (see fig 2.10 in sec. 2.2.3). Towards the high-energy domain, especially for low ionizing particles, the amount of energy deposited in the ΔE can become so low that the sensitivity needed to separate different ions is lost. Of course, the latter limit can play a role particularly in experiments with high energy beam (more than 50 MeV/u), especially in the identification of light particles. Both problems can be overcome exploiting PSA technique: the first exploiting PSA in Si1, the second PSA in CsI, where energetic are supposed to be stopped.

2.2.2 PSA techniques

PSA techniques exploit information coming from a single detector, thus, in case of PSA in the Si1 layer, it allows to lower the identification energy threshold of the ΔE-E method.

First proposed by Ammerlaan [49] more than fifty years ago, PSA techniques found a renewed interest with the diffusion of fast sampling digitizers [32, 50–53] in the market. Indeed, it is easier and more flexible to apply PSA to digitized signals with respect to analog ones.

PSA in silicon detectors

PSA in silicon detector relies on the different shape of signals produced by ions with different Z and A but fixed energy E, due to the process of carriers collection inside the detector. For instance, in fig. 2.6, the experimental signals, coming from Si1, for different ions (Z=4, 6, 8, 10) at 95.5 MeV are shown: the signal shapes are very different and depend on the fragment type, both the charge signal (left panel) and the current signal (right panel).

The impinging ion generates, along its path an initially narrow straight clouds of carriers (*i.e.* electron-hole pairs) whose density follows the so-called "Bragg curve": peaked

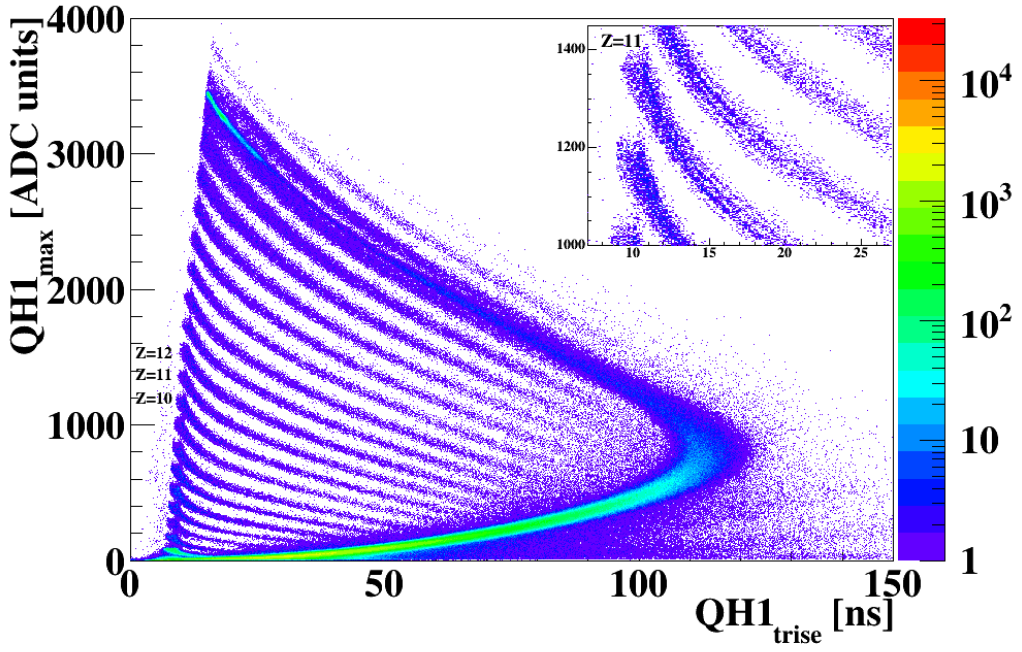

Figure 2.7: *Typical Si1 "charge PSA" of a* FAZIA *telescope: loci related to different Z up to Z=22 are visible. In the sub-panel a zoom on the Z=11 ridge is shown. Data refer to the* $^{48}Ca+^{48}Ca$ *reaction of the* FAZIA-SYM *experiment.*

shape as a function of the penetration depth with its maximum at the end of the track. The carrier density (especially for $Z>3$ and of course nearby the Bragg peak) can be so high that it can behave like a plasma of positive and negative charge. The electric field, which is present inside the depletion region, is locally much reduced (charge space effect) and a variable but long time is needed to start the drift of the carriers (the so-called "plasma time" [55–57]). Towards the respective electrodes. The higher the carrier density, the longer the plasma time. Moreover, the electric field changes going from the junction side to the opposite side of the depletion region, so as the intensity of the original electric field near the Bragg peak depends on the fragment penetration (*i.e.* the ion range) into the detector. As a consequence, the current flux in the detector and the collection time depend on Z and A of the impinging ion, as shown in fig. 2.6, even if they release the same (total) energy E. In particular, fixing the deposited energy, we observe that signals induced by heavier ions have a slower charge rise time (left panel) with respect to light ions; consequently, the corresponding effect is visible in the current signal (right panel), where heavier fragments induce signals with a maximum lower than that of lighter fragments (being the integral, *i.e.* the total charge, the same).

The FAZIA collaboration shows that if the ions impinge on the opposite side with respect to the junction side of the detector, such kind of shape differences are enhanced, without worsen the ΔE-E resolution [58]. In the so-called "reverse mounted" configuration, the carrier plasma tends to be formed in the low field region for heavy fragments, while

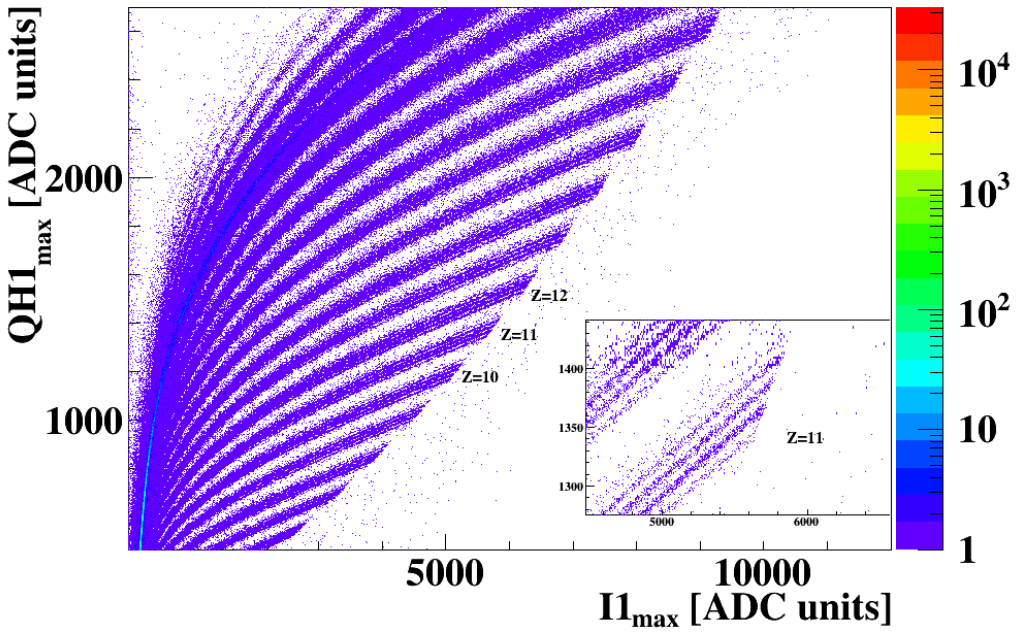

Figure 2.8: *Typical Si1 current PSA of a* FAZIA *telescope. With respect to the Q-PSA a better isotopic separation is visible, as shown also in the sub-panel for the Z=11 isotopes (cfr. fig. 2.7). Data refer to the* ^{48}Ca+^{48}Ca *reaction of the* FAZIA-SYM *experiment.*

it is more produced in the high field region for light fragments[5]. Such configuration thus enhances the plasma time effect, thus favoring the differences in the charge or current signal waveforms for different ions.

The FAZIA collaboration has investigated during the R&D phases several parameters to be used for PSA applications. The final decision has been taken between two candidate correlations:

- "charge PSA" (Q-PSA): it is based on the correlation between the energy deposited in the detector and the charge signal rise time;
- "current PSA" (I-PSA): it is based on the correlation between the energy deposited and the maximum of the current signal.

In order to show the PSA performances obtainable with the FAZIA multidetectors, a comparison of the Q-PSA and I-PSA, from the same detector, is shown in fig. 2.7 and fig. 2.8, respectively: both refer to ^{48}Ca+^{48}Ca reaction.

The loci related to neon, sodium and magnesium ions are indicated, in both figures, as well as a zoom on the sodium region in both sub-panels. During the R&D phase, the heaviest identified fragment, in charge, with both Q-PSA and I-PSA methods was

[5] As the stopping power depends quadratically on Z (see eq.(2.1)), for a fixed energy a light ion has a greater range with respect to the a heavy one.

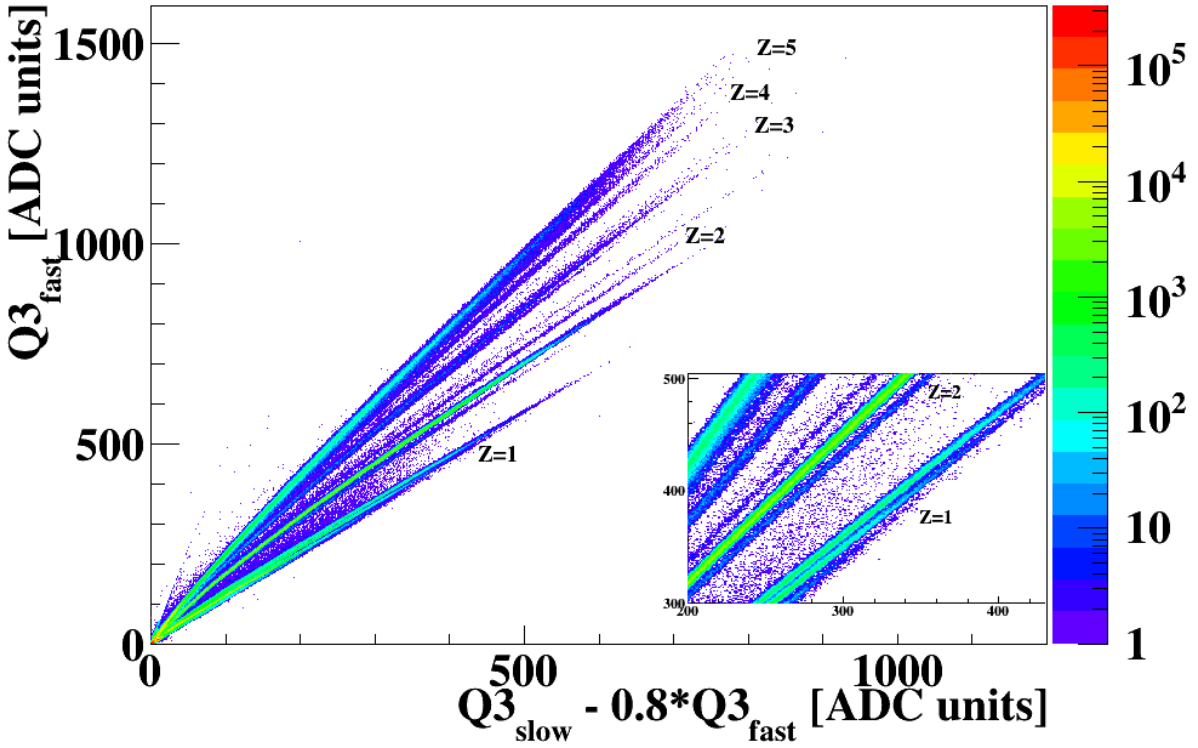

Figure 2.9: *Fast-Slow correlation matrix. Charge identification is obtained up to Z=5, while isotopic identification up to Z=4. In the sub-panel the loci related to proton, deuteron, triton, ^{3}He, α and ^{6}He are shown. Data refer to the ^{48}Ca+^{48}Ca reaction of the* FAZIA-SYM *experiment.*

Z=54 [7], while the isotopic identification performances differ between the two methods. We confirm this in the present case, just comparing the Z=11 lines between Q-PSA in fig.2.7 and I-PSA in fig.2.8, it's clear that the sodium isotopes are better separated in the latter case. In a typical I-PSA matrix the isotopic identification up to $Z \leq 19$ is reached. Since the I-PSA method allows better isotopic separation, while preserving the charge identification, FAZIA adopted this choice already since the first experiments at LNS [30]. For a quantitatively summary of the current identification limits, essentially valid also in this thesis, see sec 2.2.3.

PSA in CsI

PSA techniques are applied since decades to CsI detectors. Indeed, the fluorescence light emission generated by the passage of a particle depends on the nature (Z, A) of the particle and on its energy. The time development of the scintillation light can be modeled as a sum of two exponential functions with different decay constants: a *Fast* component (with a decay constant approximately 1μs) and a *Slow* component (with a decay constant of

few μs). Both the intensity and the decay constant of the two components depend on the Z, A and on the energy of the particles.

This behavior has been at the basis of the typical so called *Fast-Slow* PSA, in the past obtained with analogue electronics using different shaping times of a given split signal, in order to separate as better as possible the two light components. Again, the introduction of high-resolution fast digital electronics has contributed to make the *Fast-Slow* analysis easier and more flexible. As mentioned in sec. 2.1.3, it is possible to disentangle the different components of the scintillation light output by applying two digital trapezoidal filters, which differ in the flat top, so as to extract the *Fast* and *Slow* component. $Q3_{fast}$ and $Q3_{slow}$, defined in sec. 2.1.3, are used to estimated both components. However, in any case, it is impossible to perfectly separate the two components. Indeed, $Q3_{slow}$ necessarily includes a contribution of the former. In order to disentangle these two contributions and obtain a better isotopic separation, usually a fraction of $Q3_{fast}$ is subtracted from $Q3_{slow}$: in this thesis we adopted the variable $Q3_{slow}$-0.8·$Q3_{fast}$ as used by the FAZIA collaboration. As an example of a *Fast-Slow* correlation we present in fig. 2.9 the results for the ^{48}Ca+^{48}Ca reaction of the FAZIA-SYM experiment. A clear charge separation is visible up to $Z \sim 4$, while isotopic separation is nicely achieved for hydrogen and helium ions, as shown in the sub-panel.

2.2.3 Identification energy threshold

The present FAZIA identification capabilities can be summarized in fig. 2.10, where the different regions of identification methods are shown as a function of the charge of the fragments and their energy (per nucleon). Of course, the indicated limits are not strict because they depend on the quality of the different telescopes. We can say that they represent the typical behavior of the FAZIA detectors at the beginning of their use with the beams, verified so far. The presented limits are those obtained at the end of the R&D phase [41, 59].

The white region is the region where no kind identification can be obtained, so it gives the lower threshold of the FAZIA apparatus. This is ruled by the minimum energy to resolve the charge of a fragment by PSA in Si1 (cyan area). With increasing ion energy (orange area), also the mass of the fragment is accessible, up to Z <20. Ions with an energy above the punch through value for silicon layers 300 μm thick are identified with Si1-Si2 method, in charge and mass up to Z ~25 (green area). Finally, fragments that reach CsI are identified via Si2-CsI ΔE-E method, with an isotopic resolution comparable with that of the Si1-Si2 telescope (blue area) [59]. Magenta and red area represent fragments which can be identified only in charge with Si1-Si2 and Si2-CsI ΔE-E method respectively. The identification region competing to *Fast-Slow* correlation is not included in fig. 2.10. Qualitatively, PSA in CsI extends the identification of $Z \leq 2$ fragments above 100 MeV where the energy deposition in the silicon layers is very low and forbids the use of the ΔE-E method.

The identification thresholds obtained in the FAZIA-SYM analysis will be presented in sec. 3.5, at the end of the next chapter where the identification and energy calibration

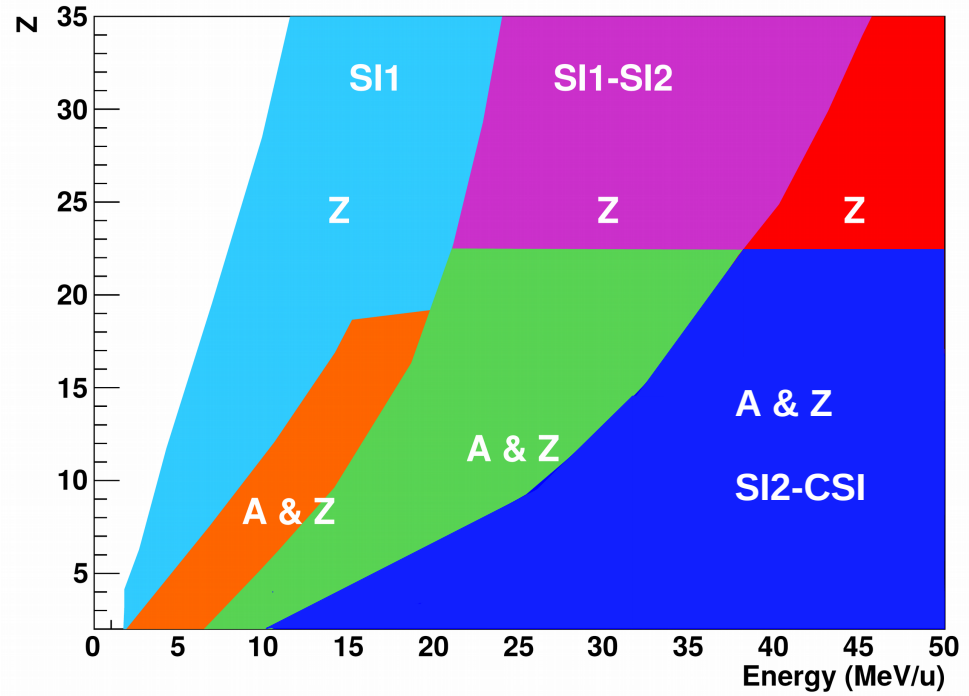

Figure 2.10: FAZIA *identification energy thresholds obtained by combing all the identification methods. The identification via Fast-Slow of CsI has not been included in this plot.*

procedures adopted in this thesis are shown.

CHAPTER 3

THE FAZIA-SYM EXPERIMENT

The FAZIA multitelescope array, thanks to its powerful isotopic identification range, is well suited for studies which aim at the investigation of isospin transport phenomena in order to constrain the asymmetry energy term of the nEoS. A possible experimental method consists in the comparison of the scaling behavior of isospin sensitive variables measured for a set of systems, where most of the reaction dynamics and effects can be considered the same, and the only differences are due to the differing neutron to proton ratio [9, 20, 60–62]. In ref. [9], M. B. Tsang *et al.*, by means of the so-called isoscaling analysis, verified the occurrence of isospin diffusion in peripheral asymmetric ^{112}Sn+^{124}Sn and ^{124}Sn+^{112}Sn systems at 50 MeV/u of bombarding energy. Moreover, comparing experimental observables to theoretical predictions, they investigated the density dependence of the symmetry term of the nuclear equation of state.

For such studies, it is customary to use a combination of different isotopes of same nuclei, in order that effects related to the Coulomb fields can be assumed identical. Most common reactions are based on Ca, Ni and Sn isotopes: indeed these elements present a rather wide range of stable isotopes which are then usable in practice for conventional experiments (see for instance tab. 3.1 for Ca reactions). During the years, the investigation of the isospin dynamics in such reactions followed two main paths. The first exploited detection arrays, that cover a large part of the solid angle but limited in the isotopic resolution of the detected fragments, as for instance the INDRA detector [31] or the Miniball/Miniwall array [63]. The common mass identification performances reach $Z \sim 8$. As a consequence, in such studies [9, 20, 61, 64], only the QP decay products could be used to extract information on the isospin dynamics. On the contrary, the second adopted the employment of mass spectrometer, in order to directly access the isospin of the QP remnants[65, 66]). However, also this second choice has experimental limitations. The covered solid angles is limited, and moreover, only one fragment per event can be detected, thus lacking breakup events or IMFs and/or LCPs accompanying the QP remnants.

In order to try to overcome the limitation of both the experimental approaches, the

INDRA collaboration coupled the INDRA multi-detector [31] with the VAMOS spectrometer [67, 68], so as to exploit strengths of both detectors, namely the mass resolution of VAMOS and the large coverage of INDRA, which is a 4π charged multi-detector. At forward angles, from 7° to 45°, it consists of three stage telescopes made by ionization chamber, silicon detector and CsI(Tl) scintillator; from 45° to 176°, it is made by two stage telescopes of ionization chamber and CsI(Tl) scintillator. VAMOS is a large acceptance magnetic spectrometer with a focal plane detection system composed of a ionization chamber, a silicon detector array and a CsI wall [67, 68] and it allows the precise identification of fragments both in charge and mass. By means of the INDRA detector a good determination of the impact parameter could be obtained, while the VAMOS spectrometer, placed at forward angle, could be used to identify the produced QP remnants (charge and mass). In particular VAMOS covered angles between 2-7°, sampled by twelve magnetic rigidity settings to explore the whole fragment momentum distribution[1]. The main results of this experimental campaign are reported in refs. [69–71].

However, the detection multiplicity limitation of the VAMOS spectrometer have a significant impact also in this campaign. First, LCP emitted at polar angles covered by VAMOS can still not be detected. For instance, this can cause a bias on the impact parameter estimation for the most peripheral events, once LCP information are used, as the LCP total multiplicity or the LCP transverse kinetic energy [1]. Second, the QP breakup channel cannot be accessed, thus no information on the isospin dynamics of this channel can be obtained.

The FAZIA-SYM experiment rises directly from the INDRA+VAMOS experience in order to try to recover both limitations. We aim to measure the four reactions involving calcium isotopes in order to complete the previous study with information not accessible with the INDRA+VAMOS setup. Moreover, many efforts have been spent by the INDRA collaboration to normalize the twelve magnetic rigidity settings and sum the whole acquired statistic. FAZIA can also be used as a reference point in comparable event classes.

3.1 FAZIA-SYM scientific goal

The FAZIA-SYM followed these previous studies and aimed at the investigation of the same two-pairs Ca+Ca reactions in order to extract information on isopin phenomena. As said, the stable Ca-isotopes allow to span a rather wide isospin asymmetry ($\delta = \frac{N-Z}{A}$) which goes from 0, for the $N = Z$ ^{40}Ca, to 0.16 for the neutron rich ^{48}Ca. Tab 3.1

[1] A magnetic spectrometer is based on the deviation of a charged particles with charge Ze, mass A and velocity v by a magnetic field B uniform and orthogonal to the particles motion. Indeed, the particle follow a circular trajectory with a radius ρ defined by:

$$B\rho = 3.107\frac{Av}{Ze} \tag{3.1}$$

$B\rho$ is named magnetic rigidity.

Table 3.1: *List of the* FAZIA-SYM *reaction and their isospin information.*

Reaction	E_{beam} [MeV/u]	Projectile Isospin	Target Isospin	System Isospin
^{48}Ca+^{48}Ca	35	0.16	0.16	0.16
^{48}Ca+^{40}Ca	35	0.16	0	0.09
^{40}Ca+^{48}Ca	35	0	0.16	0.09
^{40}Ca+^{40}Ca	35	0	0	0

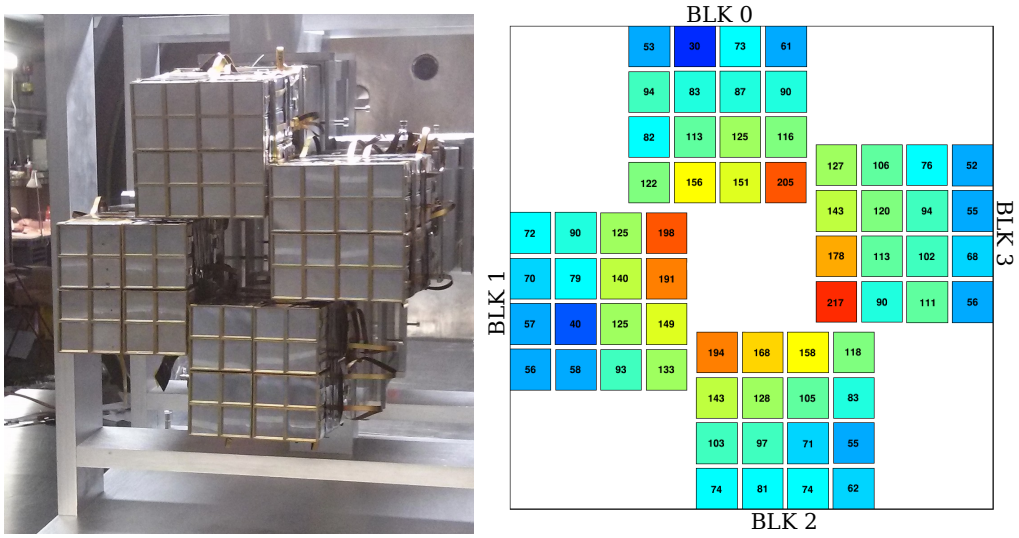

Figure 3.1: *Left Panel: view of the four blocks used during the* FAZIA-SYM *experience, arranged between 2° and 8° around the beam axis. The center of the blocks is located 80 cm far from the target (not visible in the picture). Right panel: scheme of the* FAZIA *blocks. Blocks are labelled from BLK 0 to BLK 4 turning counterclockwise. The number inside each telescope represent the average count/s during the acquisition.*

shows the relevant δ values for the initial reacting nuclei and for the composite system in case of complete charge equilibrium. With these combinations, we can follow the evolution of the neutron to proton equilibration from peripheral to more violent collisions i.e. towards reactions where the overlap is large due to the small impact parameter. This n-p equilibration, driven by the initial unbalance of the n-p content in the asymmetric systems, does not occur in the reference symmetric reactions. In this case one can expect that other processes can develop, as for instance the isospin drift (if a densitity grandient is formed) [4].

In order to cover a similar polar region as covered by VAMOS in the INDRA+VAMOS experiment, four FAZIA blocks have been mounted between 2-8° around the beam axis, arranged in the a wall configuration. A picture of the FAZIA-SYM setup seen from the front side is shown in the left panel of fig. 3.1. Right panel of fig. 3.1 show a schematic representation of the four FAZIA blocks: it has been taken from an online acquisition and the number and the color inside each telescope refers to the average count rate over

a period of 10 s. The center of the four blocks is located 80 cm far from the target.

With this configuration we aim to investigate isospin dynamics in two reaction channels, that can be contemporary resolved for the first time by the FAZIA telescopes: the QP evaporation channel, and the QP breakup channel. Thanks to the FAZIA identification capabilities, comparable with those of a mass spectrometer for Ca-ion beam, we can now look at the n-p equilibration directly detecting the QP remnants with in coincidence the possible accompanying particles. Moreover, we aim to investigate the n-p equilibration in the QP breakup channel and directly compare the results with the QP evaporation channel.

Although with limitations imposed by the scarce angular covering, we can attempt a study of the longly debated evidence of neutron enrichment of LCPs and fragments emitted at mid-velocity which, within some transport models, is attributed to the preferential neutron migration towards regions at subsaturation densities like the neck-region forming during semiperipheral nuclear interactions [4].

All the experimental results will be compared with the predictions of a transport model simulation with a twofold aim. On one side, the predictions of well acknowledged reaction models represent a track to guide and confirm the analysis selections and cuts imposed on the data. On the other side, once the model predictions are checked to faithfully reproduce most experimental observables, the fine tuning of important parameters (for instance those regulating the nEoS far from equilibrium) can be attempted via comparison with data. As theoretical model, as anticipated, we chose to use the AMD transport model [10, 72, 73] coupled with the GEMINI statistical code as afterburner [74], on which we have a deep expertise having used it for the ISO-FAZIA experiment [30], as well as for other experiments [75]. Both AMD and GEMINI will be presented in chap. 4. In the following, the experimental setup and the data reduction procedures will be described.

3.2 Experimental Setup

The FAZIA-SYM experiment was performed in Catania at the Laboratori Nazionali del Sud (LNS) of Instituto Nazionale di Fisica Nucleare (INFN) in December 2015 inside the Ciclope scattering chamber. It was the second physics experiment after the R&D phase. ^{40,48}Ca beam at 35 MeV/u was delivered by the Superconducting Cyclotron impinging on a ^{40,48}Ca targets with a thickness of 500 μg/cm^2: in order to avoid Ca oxidation during the mounting and dismounting phase in air, a carbon backing of about 10 μg/cm^2 on both side was used. Data were also acquired for a ^{12}C target (300 μg/cm^2) to estimate the carbon contamination in the acquired data (see Appendix A.0.1). The vacuum inside the scattering chamber was 2×10^{-5} mbar during the whole experiment.

For the search of clarity and faithful description of the experiment we must here mention some problems unfortunately occurred during the data taking which have impacted on the results of this thesis. First, block number 3 (labelled according to the right panel of 3.1) stopped functioning quite soon, in an early stage of the experiment due to problems on the HV of its FEE. Data coming from this block were not acquired, thus the effective

number of working blocks was 3. However, since each block covers same polar angles (i.e. from 2° to 8°) but at different azimuthal angles, this lack does not bias to much the acquired events, but restricted the available statistics. Second, due to some general accelerator problems during the ^{40}Ca beam delivery and transport, the time assigned for this section was exhausted without acquire enough statistic for the reaction ^{40}Ca+^{48}Ca: the number of collected events is very poor, insufficient to perform any significant analysis. However, the investigation of the isospin diffusion is still possible exploiting the ^{48}Ca+^{40}Ca reaction. Third, also during the experiment with ^{48}Ca, the setting of the beam transport was not completely fine; the beam has been hardly aligned along the vacuum channel and then focussed on the target. Unfortunately, after many checks and trials, we got an experimental condition where a faint beam halo was still present, hitting on a border of the Aluminium support of the target foil. This caused a background of reactions on Al mixed with the data set of the desired Ca target. This background has been put into evidence by exploiting events acquired with specific runs of beam on a blank frame, purposely mounted in the vacuum chamber. The description of the background effects and its correction is described in Appendix A.0.2, but it is important to stress that, as shown in details in the Appendix A, neither the background reactions on the Al target frame, nor those on the ^{12}C target baking have a sensitive impact on the acquired data, and so on the proposed analysis.

3.2.1 KaliVeda software

All the acquired data have been stored at the IN_2P_3 Computing Center of Lyon (FR) [76]. The data reduction, including identification and energy calibration has been performed with an already available C++ library developed for nuclear physics experiment, called KaliVeda [77] and based on the ROOT [78] framework. It is a toolkit for analysis and simulation of Fermi energy heavy ion collisions, developed along the years by people of the INDRA collaboration and recently upgraded to include the FAZIA telescopes and their features, freely available to download. It allows the management and treatment of large datasets, including also energy loss, stopping power and range calculations for $E/A = 1 - 100$ MeV; it includes algorithms and graphical applications dedicated to the fragment identification in ΔE-E and PSA matrices, both in silicon and in CsI detector.

During my thesis work, some months (including a stage at Caen in France) have been devoted to become acquainted with the KaliVeda software that has been used for the most part of the analysis described here. Since the use of KaliVeda for accurate ion identification and energy calibration is important for this thesis, in the following paragraphs, the adopted methods and algorithms will be critically described, also discussing the results obtained in the various calibration steps.

3.3 Identification procedures

In this section the ion identification procedures adopted in KaliVeda to access at the charge and the mass of the detected fragments are described. As reference in the examples, the data of the ^{48}Ca+^{48}Ca system will be used: the same techniques have been applied to the other systems. All the matrices presented in this section refer to the telescope 221 except where otherwise specified. The telescope identification code is defined in the following way. A block is divided in four quartets clockwise numerated from 1 to 4; a quartet is divided in four telescopes clockwise numerated from 1 to 4. The telescope identification code is: #block*100 + #quartet*10 + #telescope. The telescope 221 thus refers to the telescope 1, of the 2 quartet of the block number 2.

In the FAZIA-SYM experiment, three FAZIA blocks[2] were used, for a total of 48 telescope. First of all we had to check the stability of the matrices along the whole experiment, in order to define subsets of stable runs so as to not decrease the identification resolution. For instance we mention that the HV follower of the silicon detector, which was supposed to be automatic, was turned on after almost 500 runs from the beginning of the ^{40}Ca beams. Consequently, it was not possible to add the whole statistics for Si1 PSA matrices for the ^{40}Ca beam system. We also observed a variation in the CsI scintillation response between the ^{40}Ca and ^{48}Ca beam, in particular in the Fast component. Indeed, between the former and the latter runs we observed a raise in the temperature[3], and consequently a variation in the Fast response of the CsI scintillation light output. Last, other minor shifts of the matrices have been observed and taken into account. To summarize more than 400 grids were necessary to the identification of the whole FAZIA-SYM systems: as explained in the following, the realization of the identification grids is a cumbersome and time consuming task, which has required many months of work.

3.3.1 Idenfication of fragments

Independent of the kind of identification technique, the KaliVeda software offers a specific tool to perform ion identification starting from a event correlation matrix. Without loss of generality, we consider here the case of a ΔE-E matrix for the layers Si1 and Si2 of a given telescope, but the same can be repeated for the other methods: Si2-CsI ΔE-E and Si1 PSA matrices.

Fig. 3.2 shows the Si1-Si2 correlation plot for the telescope 221: beyond the data, represented by dots, the figure also shows the grid lines tracked for the identification procedure (see below). The graphical tool allows the user to easily track a grid (using essentially the mouse buttons) made of piecewise segments drawn. The minimum request

[2]We remind that the block number three had a fault at the beginning of the experiment and it has not been used in the data analysis.

[3]The only point where the temperature is read in a FAZIA block is at the level of the FEE cards. Between the two beams it changed from 30° up to 40°. Even if we cannot directly correlate CsI temperature to the FEE temperature, the CsI crystal is the telescope stage closer to the FEE cards, thus it could be affected by this temperature changing.

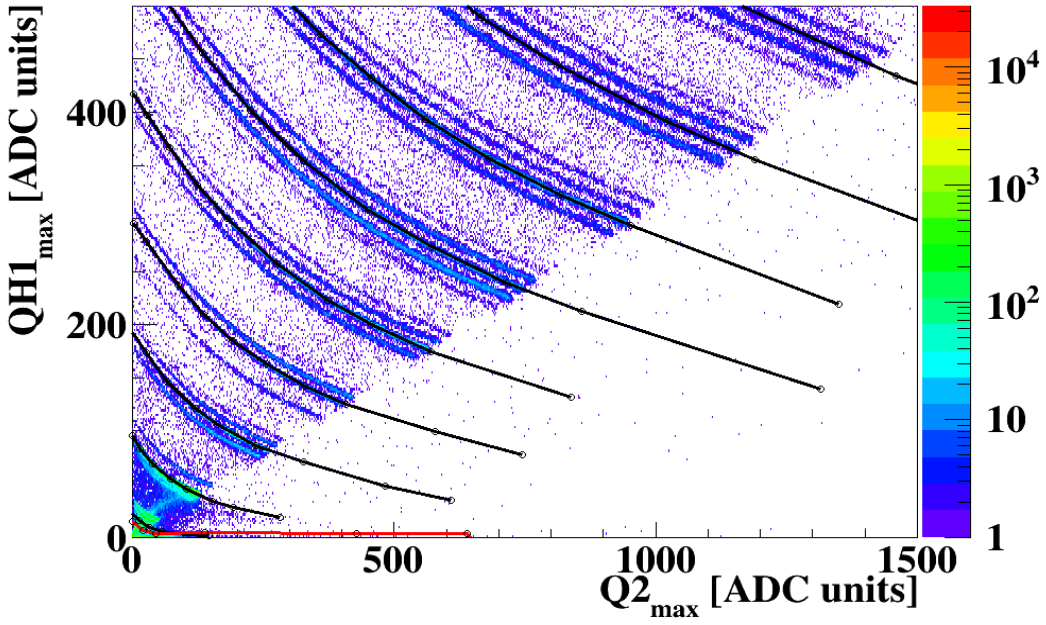

Figure 3.2: *Si1-Si2 ΔE-E correlation matrix with the grid used for the fragment identification superimposed. The region below the proton line corresponds to signal with amplitude comparable with the noise level, and excluded from the identification procedure.*

is to complete a segmented line for each set of isotopes[4]; commonly the users follows as best as possible the ridges, aiming at draw piecewise lines equally spaced. An example of identification grid is shown in fig. 3.2 superimposed on Si1-Si2 ΔE-E correlation: the correlation shown lines from $Z = 1$ up to $Z = 9$ and a black line is drawn for each Z, corresponding to a given mass value.

Regions of the matrix can be excluded from the identification procedure by means of a graphical cut. For instance, in fig. 3.2 a graphical cut has been used to remove the region below the proton line, corresponding to silicon signals with amplitude comparable to the noise level (below the red line in fig. 3.2).

A Particle Identication (PI) number is assigned to each line, corresponding to the atomic number Z of the detected ion. After the grid tracking, the KaliVeda tool allows to produce a PI distribution. This is done by means of an interpolation procedure of the position of the detected fragment in the matrix between the 4 closer lines in the grid. At the end of the interpolation a PI distribution is obtained. An example of such distribution is shown in fig. 3.3, where every peak corresponds to a different isotope. In particular in fig 3.3, peaks below PI=16.5 refer to Sulfur isotopes, while peaks above it

[4]Exceptions, in that respect, are the Si2-CsI ΔE-E and CsI PSA identification procedures. In the Si2-CsI case a second grid is used, limited to $Z = 1$ and $Z = 2$ but containing a line for each isotope. Also in the CsI PSA case a line for each isotepes is drawn. More detail will be given in sec. 3.3.2, for Si2-CsI and Fast-Slow respectively.

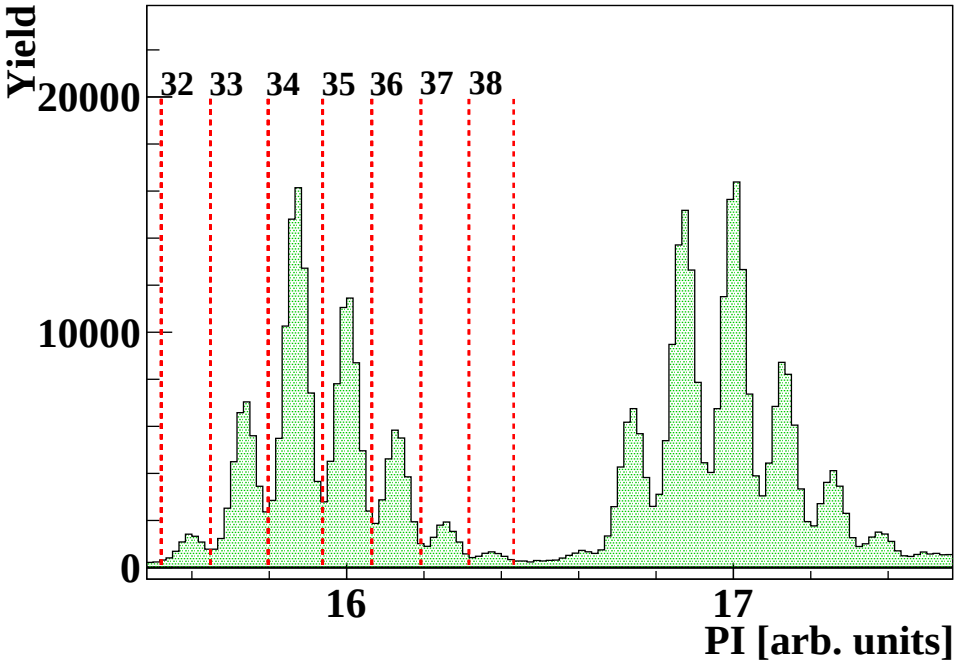

Figure 3.3: *PI distribution for $Z = 16$ and $Z = 17$ ions, obtained after the interpolation of fig. 3.2. Mass intervals are shown for $Z = 16$ with the associated mass number on top.*

to Chloride ones. Starting from such distribution the mass number A can be assigned to each ion. We chose to adopt sharp intervals in correspondence with the minima between two consecutive peaks. In this way the charge and mass assignment is done starting from the stored grids and mass intervals (a set for each telescope and for each homogeneous subset of runs). In fig. 3.3 those related to $Z = 16$ are drawn with red dashed line and the associated mass number on top.

We observe that, in isospin studies the correct evaluation of the mass value of each fragment is important; therefore, to allow for different further checks on the results by imposing more ore less good-quality cuts, an identification quality code is assigned to each identified fragment. The adopted code are the following:

- IDCode=0 - only good Z or good Z, A;
- IDCode=1 - Z is reliable but A can be lower by one unit;
- IDCode=2 - Z is reliable but A can be larger by one unit;
- IDCode$\geq$3 - not identified at all.

In this work, only fragments with IDCode=0 are considered for the analysis. They are 98% of the total identified fragments.

3.3.2 Identification of light charged particles

The LCP identification procedure adopted for Si2-CsI and *Fast vs. Slow* correlations differ slightly with respect to the standard procedure described in sec. 3.3.1. As shown in fig. 3.4 and fig. 3.6, where two Si2-CsI and CsI *Fast vs. Slow* correlation matrices are presented respectively, we chose to draw piecewise lines in correspondence of each Hydrogen and Helium isotopes.

Instead of only one line for each element, in both cases, to each line a PI number is assigned according to the Z and A of the detected particle: for these ions the interpolation algorithm gives better results when all the isotopic lines are drawn. In the case of Si2-CsI, heavier ions ($Z \geq 3$) do not present any significant variations with respect to the method described in the previous section.

It's worth mentioning the presence of a red line at the bottom of the correlation in fig. 3.4. The region below the red line includes particles whose $Q2_{max}$ is comparable with the noise level in Si2 (less than 5 ADC units) but that release a significant value in CsI (up to 400 ADC units). Such cases can then be associated to radiations which deposit energy only in CsI crystals and not in the silicon layers, as neutron or gamma rays [79]. Indeed, the interaction probability in thin silicon layer for neutron and gamma rays is negligible, while an interaction could occur in CsI crystals, thus producing at least a charged particle depositing a sensible amount of energy. Consequently, such events would be seen in the CsI *Fast vs. Slow* correlation ass the charged product of the reaction, thus polluting the true LCP sample. This is proved by the sub-panel of fig. 3.5 where the *Fast vs. Slow* correlation of such particles is reported: loci related to Hydrogen and Helium ions are filled. The spurious effect of such particles can be seen in fig. 3.5, where the $Q3_{slow}$ distribution is shown[5]: in particular, with black line the distribution obtained considering all the products identified as proton (including PSA in CsI), with red line that obtained from protons identified in CsI PSA with a $Q2_{max}$ below threshold (labelled ad "Neutron" in the legend for sake of brevity), with blue line particles identified as proton in ΔE-E Si2-CsI correlation matrix of fig. 3.2. For sake of clarity, summing the red and the blue distribution the black one is obtained. From fig. 3.5 one can note that protons identified in Si2-CsI correlations and protons identified in CsI PSA with $Q2_{max}$ below threshold presents two different shapes, thus suggesting a different origin.

Finally, the region below the red line in the *Fast vs. Slow* correlation of fig. 3.6 corresponds to particles whose do not deposit in the CsI their whole energy. As shown in ref. [79] particles can scatter with the CsI ions and then escape from the crystal without depositing the whole energy. This region is excluded from the identification procedure.

3.4 Energy calibration

The energy calibration lean on the identification results, for both silicon and CsI detectors. Moreover, energy calibration can provide useful cross check on the goodness of the

[5] Only a fraction of the available statistics is used to produce this picture.

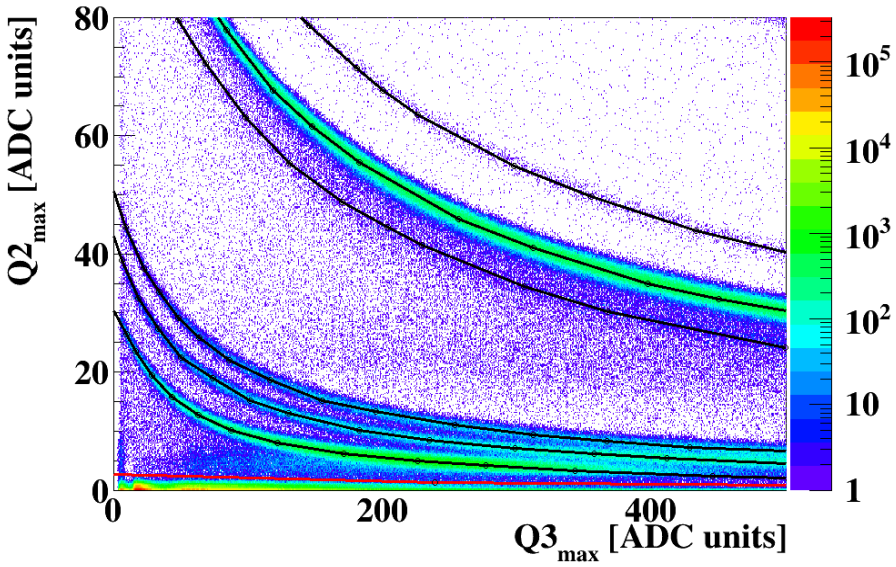

Figure 3.4: *Si2-CsI ΔE-E correlation matrix with the grid used for the Light Charged Particle identification superimposed. The region below the red line includes radiations which deposit energy only in CsI crystals and not in the silicon layers, as neutron or gamma rays [79]. Such region is excluded from the identification procedure.*

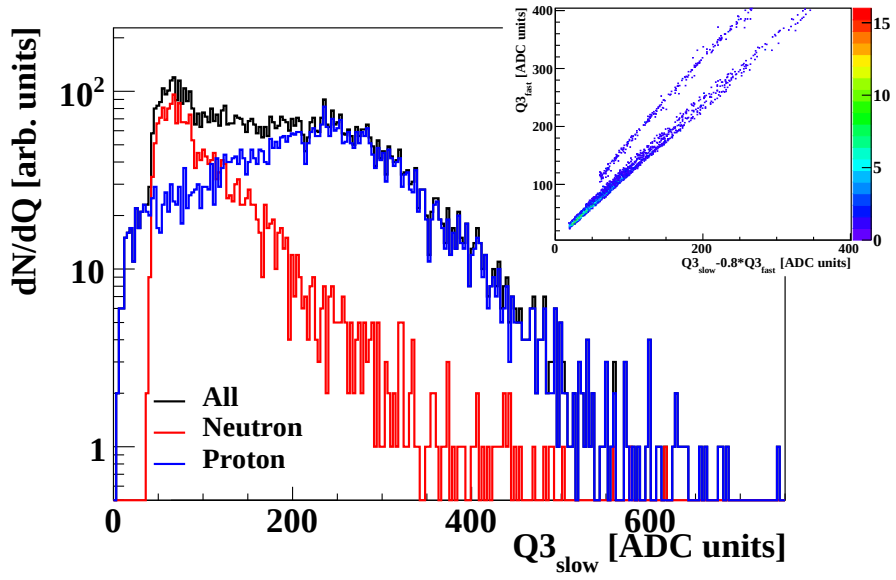

Figure 3.5: *$Q3_{slow}$ distribution of all the products identified as $Z = 1$, $A = 1$ (black), within the proton locus in ΔE-E Si2-CsI of fig. 3.4, and as protons in the CsI PSA matrix but with a $Q2_{max}$ belowe threshold (labelled "Neutron" in the legend for sake of brevity). Sub-panel shows the Fast vs. Slow correlation obtained for particle labelled ad neutron or gamma rays. Only a fraction of the available statistics has been considered.*

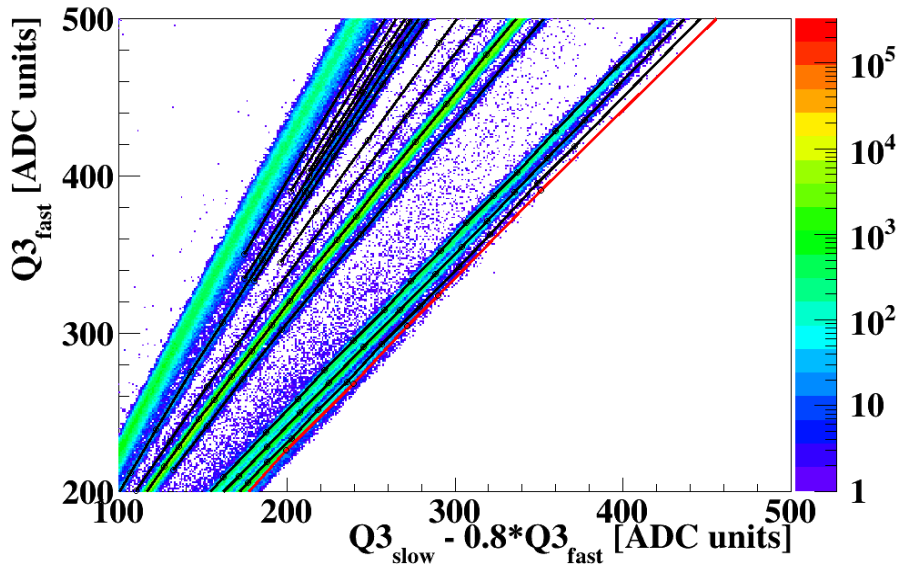

Figure 3.6: *Fast vs. Slow correlation matrix with the grid used for identification superimposed. The origins of both x-axis and y-axis are suppressed, in order to show a region where the H and He ions are better separated. The region below the red line corresponds to particles whose do not deposit in the CsI their whole energy and excluded from the identification procedure.*

identification results. Indeed, we remind that energy calibration and identification are not correlated each other, as all the identification procedures have been performed using matrices in channels (i.e. ADC units) and not calibrated in energy.

In order to show the calibration procedure, data of the reference telescope 221 will be again used (cfr. sec. 3.3.1), except where otherwise specified.

3.4.1 Silicon calibration

The silicon energy calibration exploits the punch-through energy of an ion exiting from the Si2 and entering in the CsI layer. These cases are well identifiable in the experimental matrices Si1-Si2 ΔE-E because they produces various cusps in the plot, and correspond to the energy needed by a ion to cross about 800 μm of silicon (the exact value depends on the specific Si1-Si2 thicknesses). Since the pair (Z, A) of each ion has been assigned by the identification procedures, from reliable energy loss calculations the correlation between the deposited energy and the measured value in channels can be built: in fig. 3.7(a,b) the "ADC units-Energy" correlations are presented, for Si1 and Si2 respectively. In particular, the punch-through cusp points are extracted by means of a dedicated graphic program which store the coordinates, namely the corresponding Si1 and Si2 ADC units. The more the size of the ion, the less the resolution of the cusp. For this reason only ions up to $Z = 16$ are used, as for heavier ions the cusps were not well resolved.

A key ingredient of such procedure is the effective thickness of the detectors, in order

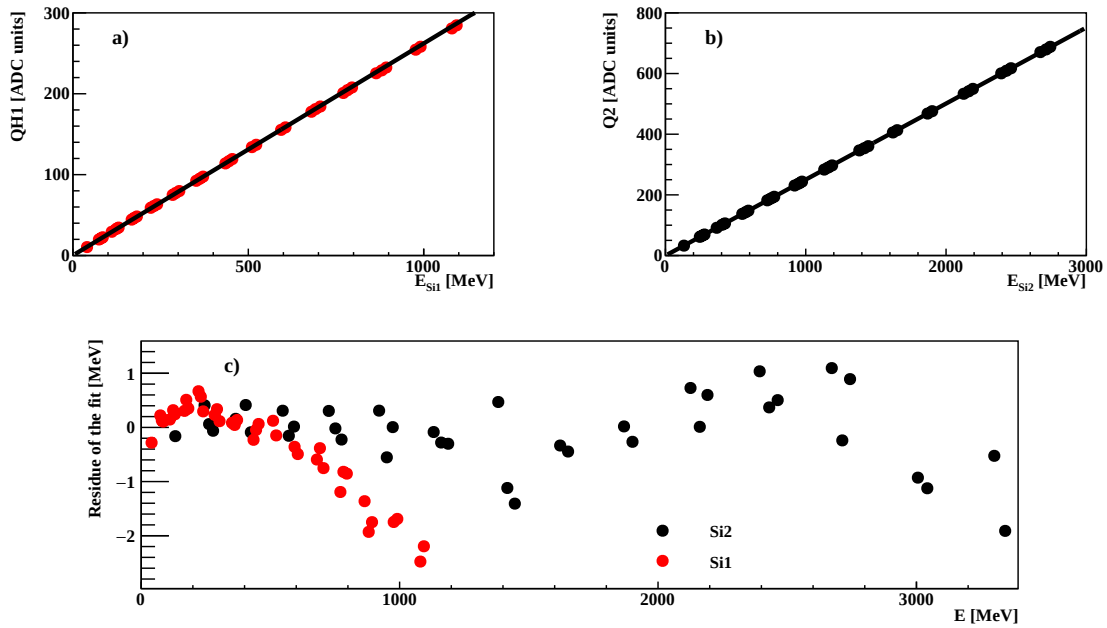

Figure 3.7: *a) Channel-Energy correlation of the Si1 detector with superimposed the fit result. b) Channel-Energy correlation of the Si2 detector with superimposed the fit result. c) Residues of the fit both for Si1 and Si2 according to the legend. Data refer to the representative telescope 221 (cfr. sec. 3.3.1).*

to properly extract the energy deposited in each silicon layer. The detectors thickness has been measured for most of the detectors by means of a micrometer. Where the measured thickness was not available, the nominal thickness of the silicon bulk has been assumed (i.e. 309 and 509 μm).

To extract the calibration parameters we performed a fit with a first order polynomial function[6] and the results of the "ADC units-Energy" fits are superimposed to the experimental punch-through points in fig. 3.7(a,b). The offset is left free during the fit. In tab. 3.2 the calibration parameter for the telescope 221 are shown, calculated from the experimentally measured thickness of 311 and 502 μm, for the Si1 and Si2 respectively. We observe that the offset is in both cases below the unity and very close to zero, as it should be considering the signal baseline subtraction which is performed in digital shaping (cfr. sec. 2.1.3). Moreover, also the calibration parameters calculated from the nominal thicknesses are presented. From this comparison we can evince the sensibility of the calibration parameter to the detector thickness. In particular in this case, assuming the nominal thicknesses would correspond to a variation of the silicon calibration factors

[6]Silicon detectors have a linear response as a function of the deposited energy if the charge collection is optimal. It's worth mentioning that during the whole FAZIA-SYM experiment the silicon revers current of all the detectors maintained below 50 nA: consequently, charge collection effects due to radiation damage were reasonably absent. Moreover, we remind that the trapezoidal filtering used to extract the energy information are long enough to avoid any ballistic deficit (cfr. sec. 2.1.3).

Table 3.2: *Comparison of the silicon calibration parameters of the telescope 221, calculated assuming the measured thicknesses and the nominal ones. A linear function has been used to extract the calibration parameter: $E = ax + b$, where x is in ADC unit and E in MeV.*

Telescope	**Thicknesses**	**Si1**		**Si2**	
		a	b	a	b
221	measured	0.262	0.21	0.251	0.27
221	nominal	0.259	0.20	0.253	0.27

of about 1%.

In fig. 3.7(c) the residues of the fit are presented, with red and black circles for Si1 and Si2 fits respectively. While the Si2 residues are around 0, a decreasing trend is observed for the Si1. We figured out that such trend is related to the energy loss table adopted to extract the punch-through energy: in particular in this work we used the VedaLoss tables [80], based on the Hubert range and stopping-power tables [81]. For instance, with the SRIM tables [82] a different trend of the residues is obtained. However, the minimum residue values are obtained with VedaLoss, and thus we adopted it as reference.

The residues show the good quality of energy calibration that we can obtain with the FAZIA detector in a large range of energies. In particular, we quote an uncertainty of the Si1 calibration of about 0.2% at $E = 1125\,\text{MeV}$, while below 0.1% at $E = 3200\,\text{MeV}$ for the Si2 case. Moreover, the residues of the fit have been used to further check the identification results: Indeed one can see, better at high energies, that the points are grouped in subsets. These correspond to the isotopes of a given element for which the cusps have been resolved. If the mass assignment would have been wrong (this option cannot be excluded a priori for high Z tracks), one would have found strong deviations which is not the case. The obtained results not only prove the quality of the obtained energetic information, but also fix a benchmark for the fragment identification procedures in the range of ions of interest for the present work.

It is worth mentioning that in order to properly calibrate the whole dataset, different calibration parameters have been necessary, corresponding to sub-groups of runs in which the ΔE-E matrix of each telescope does not manifest significant shift (cfr. sec. 3.3.1).

3.4.2 CsI calibration

For most the detected ions the CsI energy calibration is not mandatory. Once the silicon detector have been calibrated the initial energy of the impinging ion can be reconstructed by means of the energy deposited in the silicon layers and energy loss tables. However, as mentioned before in sec. 2.2.1, as the energy of the particles increases, the amount of energy loss in the silicon detectors decreases and tends to become less related to the initial energy. This behavior is particularly evident for the light particles in ΔE-E Si2-CsI correlation presented in fig. 3.4. The loci related to protons, deuterons and tritons, after a tight correlation start to become flatten as the energy deposited in CsI increases.

Consequently, for hydrogen and helium ions the method of using only ΔE in silicon

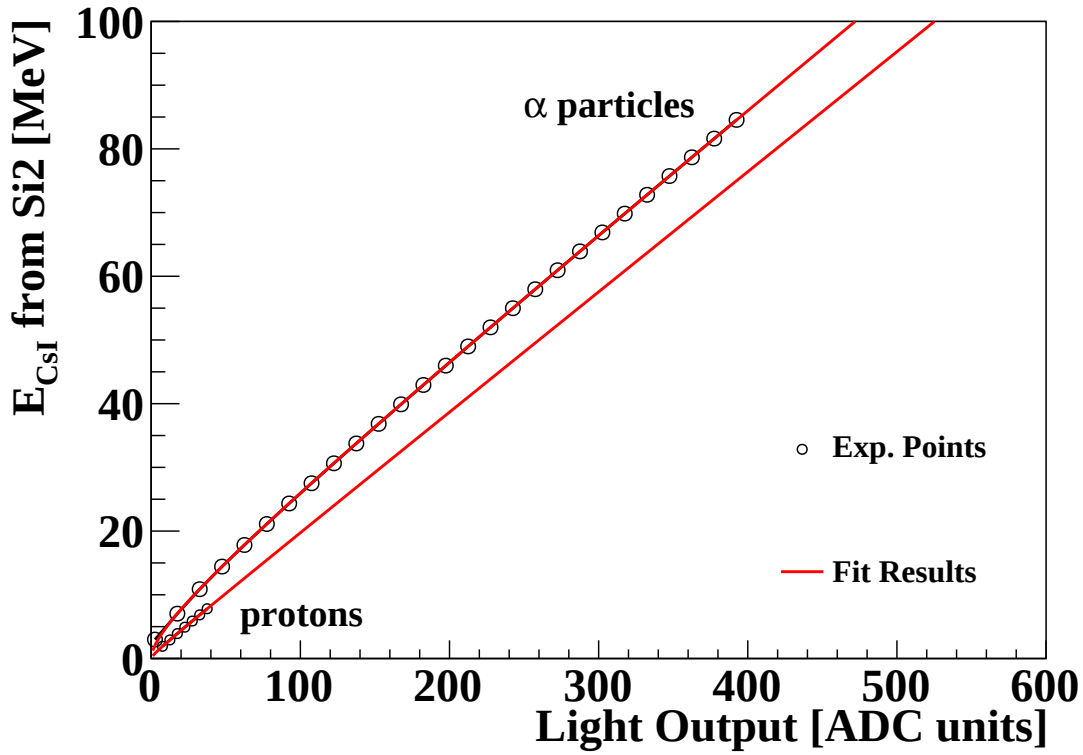

Figure 3.8: *"Energy-Light output" correlation for protons and α particles. The results of the global fit, by means of the analytical formula of the total light output reported in ref. [83, 84], are shown with red lines.*

layers is not applicable and the CsI energy calibration is required, in order to reconstruct their correct initial energy. For such purpose, we exploited the loci in the ΔE-E Si2-CsI matrix where the correlation between the energy deposited in Si2 and CsI is still tight, and, by means of energy loss calculations, we calculated the amount of energy deposited in the CsI crystal. A CsI energy calibration can be extracted from the correlation of the scintillation light output in channels and the calculated residue energy in CsI. An example of such correlation is presented in fig. 3.8 for protons and α particles.

It is well known that the light output calibration function for CsI is not linear with deposited energy. As a first choice we adopted the prescription reported by the INDRA collaboration [83, 84] for their CsI crystals and implemented as an option of the KaliVeda toolkit. According to this recipe, the relation between the light output $L.O.$ of the crystal and the energy E in MeV deposited by a a charged particle with mass A and charge Z

can be approximated by the analytical formula:

$$L.O. = a_0 \Bigg\{ E - AZ^2 a_1 \Bigg[\ln\left(1 + \frac{E}{AZ^2 a_1}\right) - \frac{a_3 \ln\left(\frac{E+AZ^2 a_1}{AZ^2 a_1 + Aa_2}\right)}{1 + e^{(a_3 - E)/8A}} + \frac{a_3}{1 + e^{(Aa_2 - E)/8A}} \ln\left(\frac{AZ^2 a_1}{AZ^2 a_1 + Aa_2}\right) \Bigg] \Bigg\} \tag{3.2}$$

where a_0 is a parameter related to the electronic gain and $a_{1,2,3}$ depend on the crystal properties [83, 84]. The AZ^2 term takes into account the light output dependence of the specific particle. The AZ^2 parametrization has been used by other experimental groups, as for instance the NUCLEX collaboration [85].

The calibration parameters have been determined by fitting eq. 3.2 to the experimental point of fig. 3.8 with a global fit considering both the proton and α particles points. We want to underline that the lack of proton points with energy deposited in the crystal above 10 MeV is not an issue. Indeed, as observed in a recent experiment dedicated to the investigation on the FAZIA crystal light output [79], as well as other experiment [86], the proton light output is practically linear from below 1 MeV up to 100 MeV, and possible non linearity effects show up at high energies, quite probably due to light collection deficit for particles penetrating much in the material [79]. Moreover, such effects are almost negligible in the context of this work. Indeed, also due to the moderate bombarding energy, the proton kinetic energy distribution presents a Maxwell-type tail such that the yield at 120 MeV is 1000 times less that at the maximum, and only a few hits reaches energies around 150 MeV.

Profiting of the fact that most all the detected LCPs are stopped in the CsI crystals[7], to test the quality of the CsI energy calibration we look at the excitation energy of fragments that decay through particle emission, as for instance ^{8}Be, or ^{6}Li that has a first excited state above the α energy threshold emission. Once their excitation energy spectrum has been obtained by means of particle-particle correlation [87–89], the peak position must correspond to the energy level of the reconstructed nucleus, and can be used as benchmark to validate the CsI energy calibration. Fig. 3.9 shows the reconstructed energy spectra for ^{8}Be, via $\alpha - \alpha$ correlation, and for ^{6}Li* via α–d correlation. In the ^{8}Be excitation energy spectrum the ground state level is clearly visible, very close to 0 MeV; also the broad first excited around 3 MeV is present, in agreement with the known level structure of ^{8}Be [90]. In the ^{6}Li case the reconstructed level is located at 2.2 MeV, compatible with the theoretical value of 2.16 MeV. Moreover, such peaks can be described by a Breit-Wigner function convoluted with a Gaussian: the width of the Breit-Wigner depends on the width of the excited level, while the width of the Gaussian takes into account the energy resolution of the detectors and their angular resolution [91]. Once we fix the width of the levels from the known values [90], the extracted Gaussian width is below 5%. The

[7] 88% of the total detected LCPs have been identified in charge by means of the CsI crystals; 92% of this sample is identified in charge and mass.

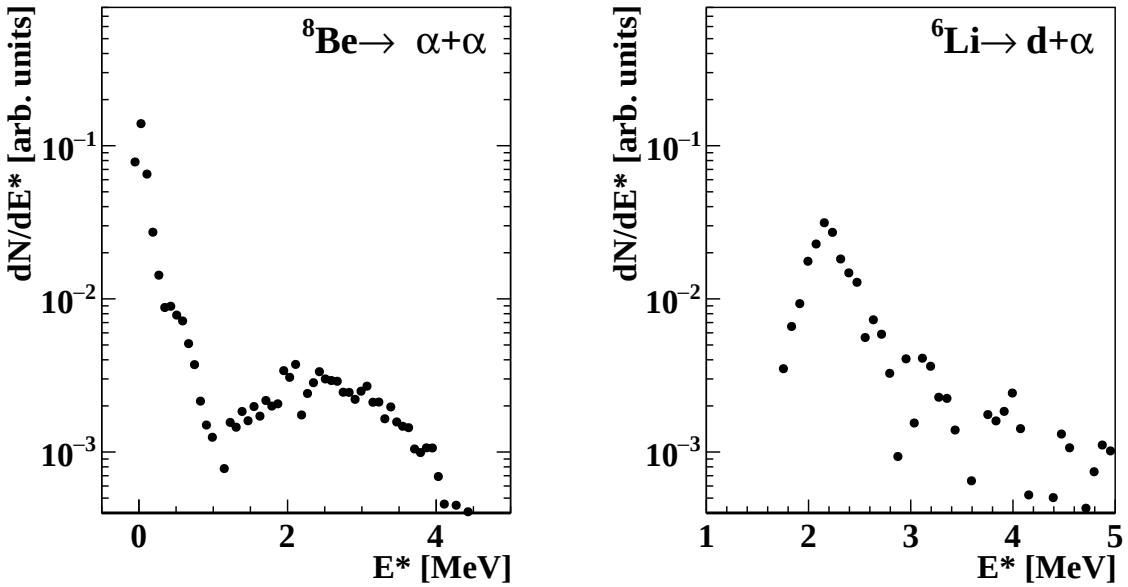

Figure 3.9: *Excitation energy spectra of ^{8}Be and ^{6}Li reconstructed from $\alpha - \alpha$ and $\alpha - d$ correlation. No gate on the backtraced parent ion velocity has been imposed.*

obtained value is comparable with the typical CsI energy resolution, suggesting that the results is dominated by this factor and not from the angular resolution.

In conclusion CsI calibrations are only used to extract the total energy of LCP, while heavier fragments are calibrated starting from the energy loss in the silicon layers since for such fragments the amount of energy deposited in Si1 and Si2 is always tightly correlated with the fragment initial energy.

3.5 The FAZIA-SYM nuclide chart

The identification and the energy calibration results can be summarized looking at the FAZIA-SYM nuclide chart: in fig. 3.10 all the isotopically identified ions are reported, exploiting all the identification methods in the ^{48}Ca+^{48}Ca reaction. Picture contain information from all the detectors.

The quality and the richness of the results is quite satisfactory and comparable, for this experiment, with that obtainable with a mass spectrometer. Indeed, the FAZIA identification capabilities have allowed to identify both in charge and mass from Hydrogen ions up to Titanium ions: $6 \div 7$ isotopes per ion, depending on its size, have been resolved. In particular we want to underline that the whole phase-space region expected to be populated by QP residues is isotopically resolved, from $Z = 10$ up to $Z = 20$ and even more, thus allowing the very exclusive analysis on the QP that we aim at.

To better illustrate the phase-space region covered by the different identification meth-

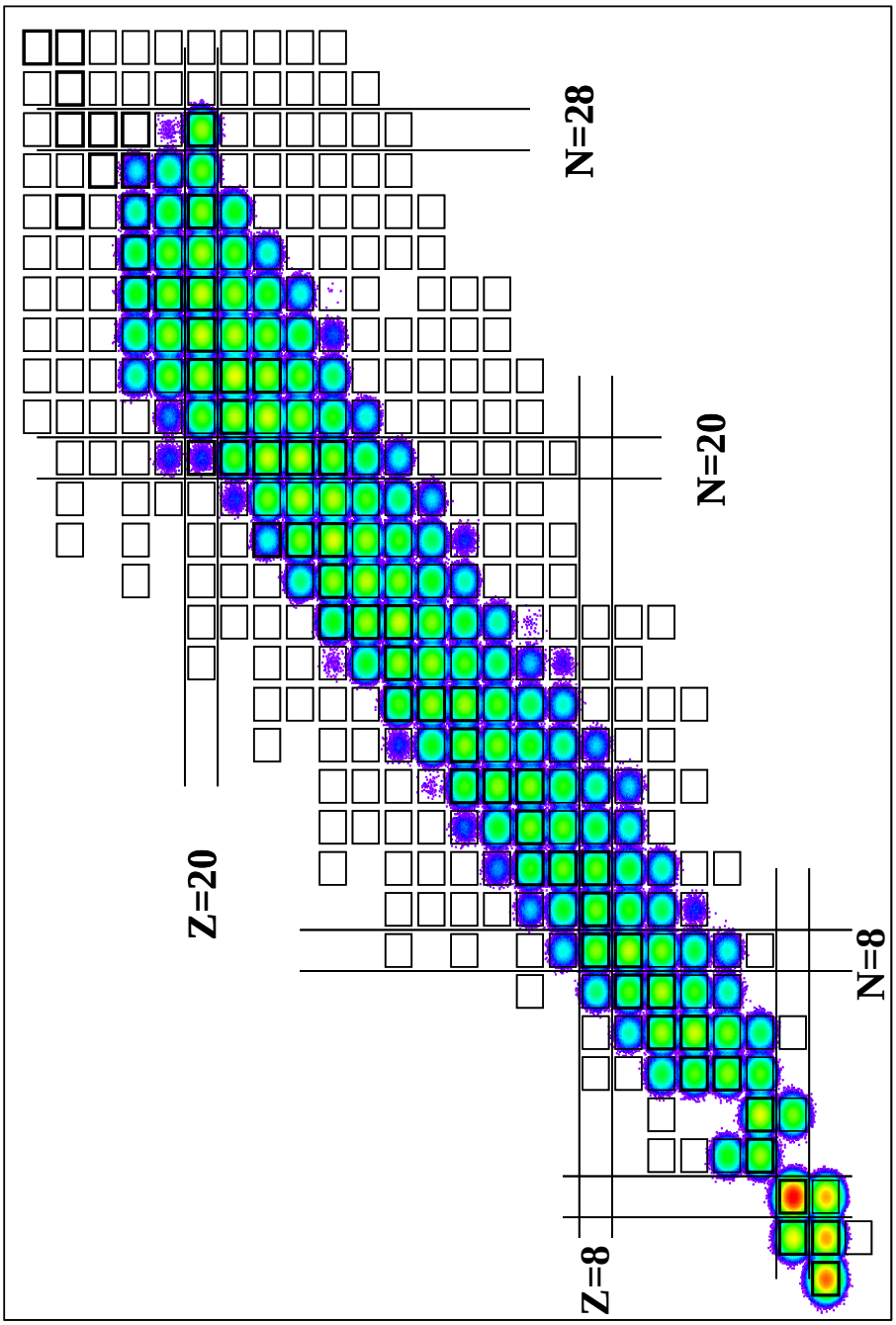

Figure 3.10: *Nuclide chart for the ^{48}Ca+^{48}Ca obtained summing the ions identified through any identification method and by all telescopes. Only ions identified both in charge and mass have been considered. Data from the ^{48}Ca+^{48}Ca reaction.*

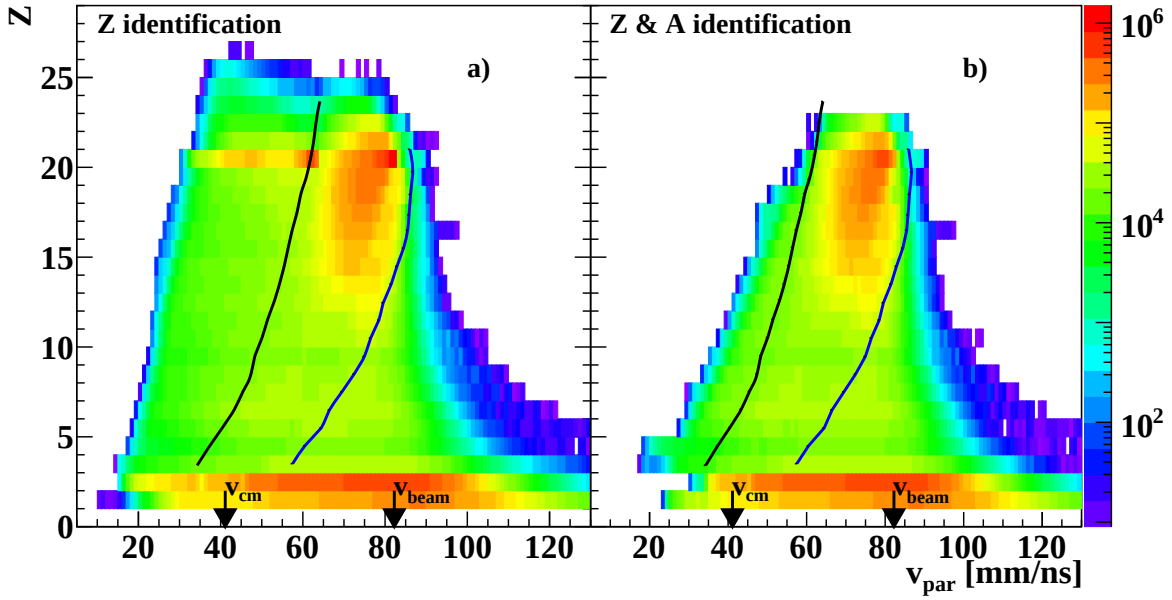

Figure 3.11: *a) Charge v.s. parallel velocity in the laboratory frame correlation for the ions identified in charge. b) Charge v.s. parallel velocity in the laboratory frame correlation for the ions identified both in charge and mass. The black line represents identification cross between PSA in Si1 and ΔE-E Si1-Si2, while blue line the one between Si1-Si2 and Si2-CsI ΔE-E. Data from the ^{48}Ca+^{48}Ca reaction.*

ods, in fig. 3.11 the correlation charge *vs.* parallel velocity in the laboratory frame is shown: panel a) contains fragments identified in charge, while in panel b) both charge and mass identification have been required. The black line represent the average energy threshold[8] between PSA in Si1 and Si1-Si2 ΔE-E, while the blue line the one between Si1-Si2 and Si2-CsI ΔE-E. Looking at fig. 3.11(a), we observe that the PSA identification allows to identify fragments with a parallel velocity slightly above the center of mass velocity (v_{cm}) down to 20 mm/ns. The most populated region, mainly fragments between $Z = 12$ and $Z = 22$, are identified by Si1-Si2 ΔE-E method: according to their parallel velocity, slightly lower with respect to the beam velocity (v_{beam}), these fragments are mostly the remnants of a QP. The ΔE-E Si1-Si2 covers the high parallel velocity region of the fragments. Once the isotopic separation is required (see fig. 3.11(b)), one can see the depletion of the low energy region of the plot as a consequence of the higher Energy threshold for mass separation via PSA in Si1 with respect to charge identification (cfr. sec. 2.2.3). Beyond this, no other evident cut in the shape of the correlation is when requiring the mass identification.

We must now comment on the energy tail with some peaked structure for the $Z = 20$ ions (fig. 3.11(a)). These are due to the aforementioned scattering with the Al target frame and detected in Si1 PSA matrices. As explained with more details in the Appendix A,

[8]The energy thresholds displayed in fig. 3.11(a,b) are calculated for a 300-500 μm Si1-Si2 telescope.

the same kind of events identified in the ΔE-E Si1-Si2 matrix, have been easily removed from the analysis with graphical cuts in the correlations (cfr. sec. 3.3.1). Once the mass identification is requested, the Al target frame events detected via Si1 PSA disappear, due to the identification energy threshold (cfr. sec. 2.2.3). In Appendix A.0.2 such events are treated with in more detail, showing that their contribution on the whole data set can be neglected, and their presence do not invalidate the results of this work.

CHAPTER 4

SIMULATION CODES AND ISOSPIN OBSERVABLES

In Heavy-Ion Collisions in the Fermi energy domain (20-50 MeV/u) many reactions can occur depending on the size of target and projectile, bombarding energies and impact parameter. As introduced in chap. 1, in peripheral and semi-peripheral reactions the cross section is almost saturated by the binary channel, where an excited QP and QT, which subsequently undergo a de-excitation process, are formed. In order to describe this kind of process, a two step mechanism is usually assumed. First, there is a dynamical phase which describes the interaction between projectile and target and the formation of the excited primary fragments. Second, a statistical de-excitation of the primary fragments come to play: the produced nuclei are treated as excited thermodynamic systems which tend towards their ground state dissipating energy by means of particle emission or other competitive mechanisms, according to their branching ratios.

Since the statistical decay process is relatively well understood and modelized, in the last years many efforts have been done to explain the primary interaction between projectile and target. Two different kinds of approaches have been adopted to develop transport models for nuclear collisions: a) models based on a mean-field approach, such as Boltzmann-Uehling-Uhlenbeck (BUU) equation (for instance SMF [92] or BLOB [93]); b) models based on molecular dynamics. The latter approach describes the evolution of the nucleon coordinates and momenta and keeps into account the multi-nucleons correlations. An example of model based on the molecular dynamics is AMD (Antisymmetrized Molecular Dynamics) [10], developed since 1992 by A. Ono and collaborators, and constantly updated [72, 73, 94, 95]. Its specific feature is the introduction of the full antisymmetrization of the multi-nucleons wave function; moreover also two-nucleon collisions are take into account by the model. In the recent code versions also the formation of light clusters as seeds for bigger primary fragments is explicitly treated by allowing each of the scattered nucleons to form light clusters such as a deuterons, tritons and α particles [73]: light nuclei, such as Li and Be, can be formed binding several clusters, thus improving the description of IMF emission.

Table 4.1: *Number of primary fragments generated for each system.*

Reaction	asy-stiff	asy-soft
^{48}Ca+^{48}Ca	35379	27633
^{48}Ca+^{40}Ca	34643	34136
^{40}Ca+^{40}Ca	54341	43435

In this work we choose to adopt the AMD model due to its capability to predict in a reliable way the main features of the collisions in the Fermi energy domain, also in semi-peripheral collisions [75, 96–98]. The AMD calculation has been stopped at 500 fm/c, from the onset of the interaction: this is a sufficient long time to assure that the dynamical phase is concluded and to ensure that the primary fragments mutual Coulomb repulsion is negligible [75]. The total amount of produced primary events is shown in tab. 4.1 for our three systems[1], with a triangular distribution up to the grazing impact parameter. The following evolution of all the hot sources in the event can be safely described by means of a statistical model, and to perform this the results of AMD simulation have been used us input for the GEMINI [11] code. For each primary event, 2000 secondary events have been produced. The simulated events have been then filtered through a software replica of the apparatus, in order to keep into account the effects of the limited angular acceptance, energy thresholds and resolutions. The secondary events produced by GEMINI++ are thus filtered to obtain calculated quantities directly comparable to the experimental data. The effect of the detector response is sizable: for instance, we find that for the ^{48}Ca+^{48}Ca system the efficiency of the apparatus is around 20%. In the following we will refer to the original simulated data, i.e. before the apparatus filter, with the label "AMD 4π".

In the following a brief description of both AMD (sec. 4.1) and GEMINI (sec. 4.2) models is presented. Moreover, a characterization of the simulated events will be presented, starting from the QP and QT characterization after the dynamical part of the interaction (*i.e.* AMD output), up to. Further, the imbalance ratio method will be introduced [8, 9] in order to explore the isospin equilibration (sec. 4.3).

4.1 Antisymmetrized Molecular Dynamics (AMD)

AMD [10] describes the nuclear many-body system by means of a Slater determinant of Gaussian wave packets as [72]:

$$\Phi(Z) = \det\left[\exp\left\{-\nu\left(\mathbf{r_j} - \frac{\mathbf{Z_i}}{\sqrt{\nu}}\right)^2 + \frac{1}{2}\mathbf{Z_i}^2\right\}\chi_{\alpha_i}(j)\right] \tag{4.1}$$

[1]We notice that running AMD (and Gemini) is a demanding job as for CPU time. To give an idea, to produce 1000 AMD events at random chosen impact parameters for one of our reaction, requests about one week

where $\mathbf{r_i}$ are the coordinates of the single particles, $Z \equiv \{\mathbf{Z_i}\}_{i=1,\dots,A}$ are complex variables corresponding to the position (real part) and the momentum (imaginary part) of the centroids of A Gaussian wave packets; ν is the width of a packet ($\nu = 0.16\,\mathrm{fm}^{-2}$) and $\chi_{\alpha_i}(j)$ are the spin-isospin states with $\alpha_i = p\uparrow$, $p\downarrow$, $n\uparrow$ or $n\downarrow$.

The time evolution of the wave packet centroids Z is obtained taking into account the mean field contribution (by means of the time dependent variational principle eq.(4.2)), and the stochastic two-nucleon collision process [72]:

$$\delta \int dt \frac{\langle \Phi(Z)| \left(i\hbar \frac{d}{dt} - H \right) |\Phi(Z)\rangle}{\langle \Phi(Z)|\Phi(Z)\rangle} = 0 \tag{4.2}$$

$$i\hbar \sum_{j\tau} C_{i\sigma,j\tau} \frac{dZ_{j\tau}}{dt} = \frac{\partial \mathcal{H}}{\partial Z^*_{i\sigma}} \tag{4.3}$$

where $\sigma, \tau = x,\ y,\ z$ are the labels for the components of $\mathbf{Z_i}(i = 1,\ 2,\ \dots,\ A)$ and $\mathcal{H}$ is the expectation value of the Hamiltonian operator H [73]. The equation of motion eq.(4.3) is solved using the Euler method with a time step $\Delta t = 0.75\,\mathrm{fm/c}$.

The AMD version used in this work implements the mean-field via the effective interaction Skyrme SLy4 [99], using $K_{sat} = 230$ MeV for the incompressibility modulus of nuclear-matter and $\rho_0 = 0.16\,\mathrm{fm}^{-3}$ for the saturation density (cfr. sec. 1.2). Two different parametrizations for the symmetry energy have been tested: the **asy-stiff**, with $E_{sym} = 32.0\,\mathrm{MeV}$ and $L_{sym} = 108\,\mathrm{MeV}$ as slope parameter, and the **asy-soft**, with $E_{sym} = 32.0\,\mathrm{MeV}$ and $L_{sym} = 46\,\mathrm{MeV}$.

The method implemented to estimate the two-nucleon collisions has been presented in a recent publication [75]. It is based on test particles which are randomly generated at every time step, by sampling the exact one-body Wigner function defined for the AMD wave function of antisymmetrized Gaussian wave packets (see Appendix C of ref.[95]). A collision between two test particles is based on geometrical conditions. When two test particles (r_1, p_1) and (r_2, p_2) collide, the collision is performed by changing the momenta of the two physical coordinates ($\mathbf{R_{k_1}}$, $\mathbf{P_{k_1}}$) and ($\mathbf{R_{k_2}}$, $\mathbf{P_{k_2}}$), that are associated with the two test particles. The final momenta $\mathbf{P'_k}(k = k_1,\ k_2)$ are allowed by the Pauli principle when the condition $\nu|\mathbf{R_k} - \mathbf{R_j}|^2 + |\mathbf{P'_k} - \mathbf{P_j}|^2/(4\hbar^2\nu) < 1.46^2$ is satisfied for all $j(\neq k)$ with the same spin-isospin state as k. With this method, the collisions reflect the exact density distribution.

The transition probability depends on the in-medium nucleon-nucleon cross section, which can be considered, within some limits, as a free parameter of the model. In the version of the code used in this work, the parametrization proposed in ref.[100] has been used, i.e. $\sigma = \sigma_0 \tanh(\sigma_{free}/\sigma_0)$, with $\sigma_0 = y\rho^{-2/3}$, where y is a screening parameter, set at $y = 0.85$ (according to [100]). All the other (standard) model parameters have been tuned by the AMD author in the past to approximately reproduce the fragment charge distribution in the central Xe+Sn collisions at 50 and 32 MeV/u [101].

4.1.1 Clusterization within AMD

As stated in ref. [73], the very basic version of AMD does not well reproduce the fragmentation yields in central collisions, underestimating the production of α particles in favor of bare nucleons.

In the AMD version with cluster correlations, when two nucleons N_1 and N_2 collide with a relative velocity v_{NN}, it is considered the case that $N_1(N_2)$ forms a cluster $C_1(C_2)$ with another nucleon $B_1(B_2)$ in the final state:

$$N_1(N_2) + B_1(B_2) \rightarrow C_1(C_2) \tag{4.4}$$

The partial differential cross section for the final channel is given by:

$$v_{NN} d\sigma = \frac{2\pi}{\hbar} |M|^2 \delta(E_f - E_i) \frac{p_{rel}^2 dp_{rel} d\Omega}{(2\pi\hbar)^3} \tag{4.5}$$

where M is the two nucleon scattering matrix with the relative momentum p_{rel}, which does not include cluster formation and $\delta(E_f - E_i)$ enforces the conservation of energy. With this approach the process also includes the collision without cluster formation, where $N_j = C_j$. The final state is still represented by a Slater determinant and the time evolution does not depend on the cluster formation. Moreover, the cluster can be broken once one or more nucleons, forming the cluster, collides with another nucleon in the system.

The addition of the clusterization permitted a relevant improvement in the reproduction of central reactions in a range of beams and energies, as for instance Xe+Sn at 50 and 32 MeV/u [101] and C+C at 95 MeV/u [97].

In this thesis, with respect to the recipe described in ref. [73, 97], a method, presented in ref. [75], is adopted to suppress the cluster correlation in nuclear medium. The probability of attaching a nucleon i to one of the scattered nucleons k (or a sub-cluster k) is reduced by a factor 1-0.3f, where f is an approximate Wigner function, with the contribution from i excluded, at the phase-space point of the center of mass of i and k. Consequently, the chance of binding several clusters is reduced[2].

4.1.2 Symmetry energy within AMD

As stated in the previous section two different parametrizations of the symmetry energy have been tested in this work: the asy-stiff, with $E_{sym} = 32.0$ MeV and $L_{sym} = 108$ MeV as slope parameter, and the asy-soft, with $E_{sym} = 32.0$ MeV and $L_{sym} = 46$ MeV. Such values are in some sense extreme values among those tested in literature [4–6, 17, 20] and we want to better explore the symmetry energy within AMD. We remind (cfr. chap. 1) that L_{sym} represent the derivative of the E_{sym} around ρ_0, where the function assumes the value $E_{sym} = 32$ MeV. The functional behavior of the symmetry energy as a function of

[2]This choice has been introduce by A. Ono from semi-empirical observations, in particular in order to obtain a better reproduction of the data reported in ref. [75]

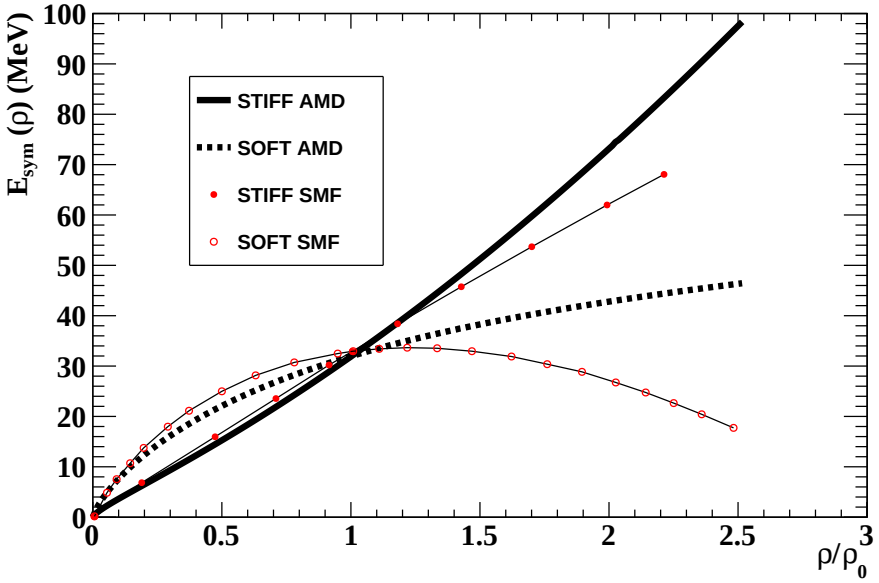

Figure 4.1: *Symmetry energy within AMD (black) and SMF (red) model (extracted from ref.[6]. For each model the asy-stiff (full) and asy-soft (open) parametrizations are shown.*

the reduced density (ρ/ρ_0) is plot in fig. 4.1, both for the asy-stiff (full black dots) and the asy-soft (open black dots).

The former linearly increases with the nuclear density, while the latter corresponds to a flatter behavior of the symmetry energy around and below normal density. In particular, we have to keep in mind that the larger differences arise moving far from the saturation density: the sensitivity to discriminate between different parametrizations is therefore strictly related to the possibility to move away from saturation density during the collisions.

The AMD parametrizations have been compared with the symmetry energy recipes of the SMF model [92], which has been used by the CHIMERA group in a study on ^{112}Sn+^{58}Ni at 35 MeV/u [102]. The asy-stiff recipe has $L_{sym} = 80$ MeV, while the asy-soft $L_{sym} = 25$ MeV [6, 102]; the E_{sym} value is 32 MeV for both of them. The trends as a function of the nuclear density are superimposed in fig. 4.1 (extracted from ref. [6]): colors are according to the legend.

We observe that the L_{sym} value limits used in these two codes differ of about 20 MeV; though, at subsaturation densities the parametrization differences are quite small. On the contrary larger discrepancies arise at supra-saturation densities. We can conclude that the symmetry energy parametrizations within the AMD model, at sub-saturation density, are basically compatible with similar prescriptions already tested and compared to experimental data as found in literature.

4.2 GEMINI statistical code

GEMINI is a Monte Carlo code, developed by R. J. Charity [11], which describes the statistical decay of a nucleus, in a large range of energies, angular momenta, and sizes. It follows the nuclear de-excitation through a series of sequential decays until further decays are forbidden by the energy conservation laws. In this thesis we use the version of the code called GEMINI++ [74], implemented in C++.

GEMINI++ accepts as input a nucleus with charge Z, mass A, angular momentum J and excitation energy E^*. In our Monte Carlo scheme, such nucleus is usually one of the primary reaction product coming from the dynamical simulation code. The GEMINI++ code is run for each primary products to obtain all the secondary fragments which can then be compared with the experimental data (after applying the geometrical filter).

In addition to the evaporation of LCPs and IMFs, GEMINI++ permits also the fission as a possible decay channel. The evaporation is treated within the Hauser-Feshbach evaporation formalism [103]. The total fission probability is calculated in the Bohr-Wheeler formalism [104], except for light systems and for the asymmetric fission of heavier nuclei where the transition state binary decay approach is used[105].

In the simulation of Ca+Ca systems we see that almost 80% of the QP breakups, whatever their nature, are produced within 500 fm/c, *i.e.* during the dynamical evolution of the reaction (by AMD). Consequently, the primary role of GEMINI consists in the evaporation of LCPs and IMFs. In the following we will then briefly describe how this mechanism is implemented in GEMINI (see ref. [74] for more details).

In the Hauser-Feshbach formalism, for the i-th particle evaporated from a nucleus with excitation energy E^* and total angular momentum J_0, the partial decay with is [74]:

$$\Gamma_i(E^*, J_0) = \frac{1}{2\pi\rho_0(E^*, J_0)} \int d\varepsilon \sum_{J_d=0}^{\infty} \sum_{J=|J_0-J_d|}^{J_0+J_d} \sum_{l=|J-S_i|}^{J+S_i} T_l(\varepsilon)\rho_d(E^* - B_i - \varepsilon, J_d) \tag{4.6}$$

where J_d is the total angular momentum of the daughter nucleus; S_i, J and l are the spin, the total angular and orbital momentum; ε and B_i the kinetic and separation energy; T_l the transmission coefficient of the evaporated particle, respectively; ρ_0, ρ_d are the level densities of the compound nucleus and of the daughter nucleus. All the possible angular momentum couplings between the initial and final states are included. This formalism is implemented for n, p, d, t, ^{3}He, α, ^{6}He, $^{6-8}$Li and $^{7-10}$Be.

The level density in the eq.(4.6) is given by the Fermi-gas formula:

$$\rho_{FG}(E^*, J) = \frac{2J+1}{24\sqrt{2}a^{1/4}U^{5/4}\sigma^3} e^S \tag{4.7}$$

$$S = 2\sqrt{aU} \tag{4.8}$$

where S is the nucleus entropy, a the density level parameter. U is the nucleus inner

energy:

$$U = E^* - E_{rot}(J) \quad \text{with} \quad E_{rot} = \frac{J(J+1)\hbar^2}{2I_{rig}} \tag{4.9}$$

obtained as a difference between the excitation energy and the (spherical) rigid rotator energy $E_{rot}(J)$, where I_{rig} is momentum of inertia of a rigid rotator with the nuclear density; $\sigma = I_{rig}T$ defines the spin cut-off term and T the nuclear temperature. Eq. (4.9) is generalized in GEMINI substituting $E_{rot}(J)$ with the Yrast line $E_{yrast}(J)$, in order to take into account the nucleonic collective behavior.

Finally, the transmission coefficient T_l is determined from the experimental available data of the inverse reaction. To fit experimental light-particle kinetic energy spectra, some thermal fluctuations of the Coulomb barrier distribution have been introduced. The barrier fluctuations may be due to fluctuations of the nucleus shape and/or of its density and/or of its surface diffuseness. In particular the transmission coefficient is calculated averaging over the values corresponding to three radii of the nuclear potential, R_0, $R_0 - \delta r$ and $R_0 + \delta r$:

$$T_l(\varepsilon) = \frac{T_l^{R_0-\delta r}(\varepsilon) + T_l^{R_0}(\varepsilon) + T_l^{R_0+\delta r}(\varepsilon)}{3} \tag{4.10}$$

where R_0 is the nuclear potential radius of the initial nucleus and δr is proportional to the square root of the temperature of the daughter nucleus.

In this work the application of the GEMINI code has been done assuming the standard parameters. No attempt has been done to investigate their possible role and to tune them in order to better reproduce the data.

4.3 Primary fragment characterization and isospin sensitive observables

In this section we want to explore the characteristics of the studied systems, ^{48}Ca+^{40,48}Ca and ^{40}Ca+^{40}Ca at 35 MeV/u, simulated by the AMD code and with GEMINI++ as afterburner. In particular, as the main goal of the FAZIA-SYM experiment is the investigation of the n-p equilibration in the QP-QT binary channel (cfr. sec. 3.1), we will focus on the characterization of such events. This section aims at introducing observables which depend on the fragment isospin and testing if they depend on the symmetry energy parametrization. It is important here to remind that AMD event calculations are stopped at time of 500 fm/c but in this time interval part of the evaporation is already performed considering that that the real interaction time, of course depending on the impact parameter, approximately ends within 100 fm/c (cfr. sec. 6.4). In the following we label "primary" fragments those produced at 500 fm/c, well knowing that these fragments have already experienced a part of their de-excitation, with respect to the initial states at the splitting time between the projectile and target. We want to underline that within AMD there is not an evaporator in the standard sense, *i.e.* a decay which follow the statistical weights. However, part of this de-excitation can have comparable characteristics

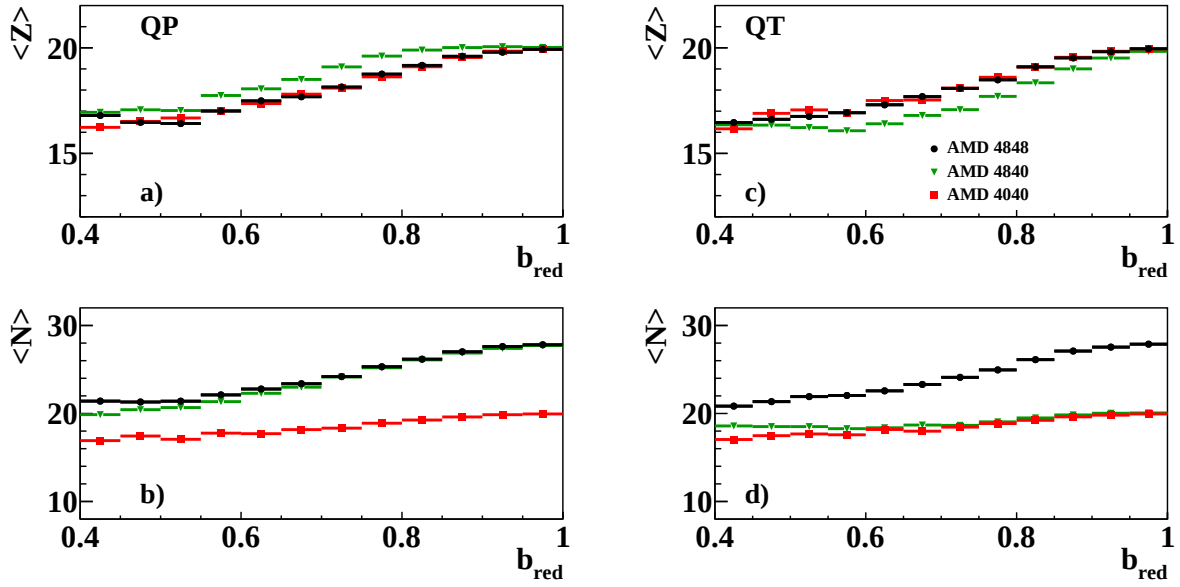

Figure 4.2: *Average characteristics of the primary QP (left column) and QT (right column) produced by AMD in the binary channel at 500 fm/c, as a function of the reduced impact parameter. Proton number (a-c), neutron number (b-d). Black dots refer to ^{48}Ca+^{48}Ca, green triangles to ^{48}Ca+^{40}Ca, and red squares to ^{40}Ca+^{40}Ca.*

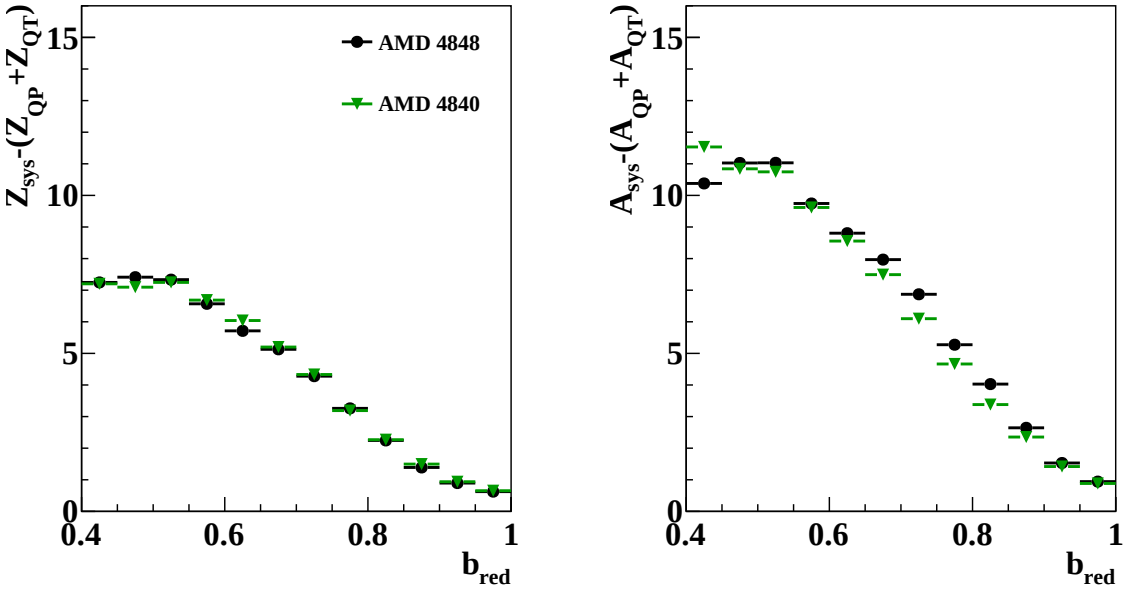

Figure 4.3: *Average charge (left panel) and mass (right panel) not bound in the QP and QT primary fragments at 500 fm/c as a function of the reduced impact parameter, for the ^{48}Ca+^{48}Ca and ^{48}Ca+^{40}Ca system.*

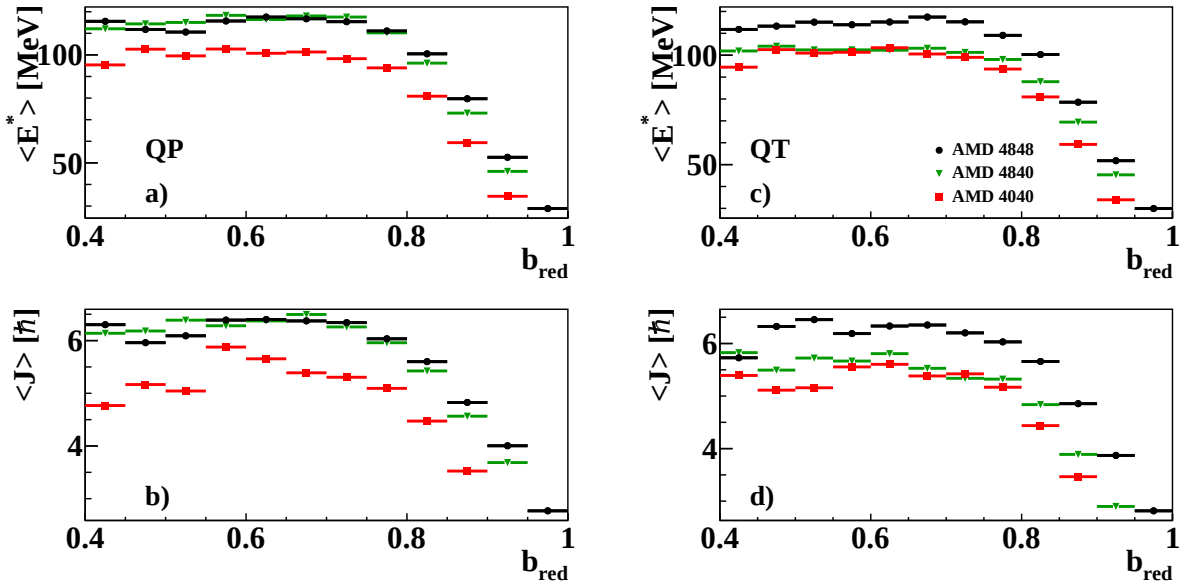

Figure 4.4: *Average characteristics of the primary QP (left column) and QT (right column) produced by AMD in the binary channel at 500 fm/c, as a function of the reduced impact parameter. Excitation energy (a-c), angular momentum (b-a). Black dots refer to ^{48}Ca+^{48}Ca, green triangles to ^{48}Ca+^{40}Ca, and red squares to ^{40}Ca+^{40}Ca.*

with that from a pure statistical evaporator [106].

Fig.4.2 presents the main characteristics of the primary QP (left column) and QT (right column) as a function of the reduced impact parameter $b_{red}) = b/b_{gr}$, *i.e.* the ratio between the impact parameter and the grazing impact parameter; details of the various sub-figures are in the caption. Only events with b_{red}>0.4 will be shown, since in more central collisions large fluctuations are observed due to a lack of statistics. y-axis errors are statistical (if not visible are smaller than the marker size); x-axis errors are the half bin width. In the following, except where otherwise specified, full black dots will refer to ^{48}Ca+^{48}Ca system, full green triangles to ^{48}Ca+^{40}Ca, and full red squares to ^{40}Ca+^{40}Ca. Results refer to the AMD asy-stiff simulation.

The average charge (panel a-c) scales as a function of the centrality, from $Z = 20$ for the most peripheral reactions down to $Z \approx 15$ for the most central ones. As expected, in both symmetric systems the QP and QT charge are identical, while in the mixed system QPs are heavier than QTs, between 0.6< b_{red} <0.9. Rather interesting, in this range, we also observe that in the ^{48}Ca+^{40}Ca reaction the QP charge is higher than in the symmetric systems, while that of the QT is lower. The same observation is not valid for the average neutron number (panel b-d), where the ^{48}Ca+^{40}Ca QP (QT) almost overlaps with the ^{48}Ca+^{48}Ca QP (^{40}Ca+^{40}Ca QT).

In order to shed light in such observation, in fig. 4.3 the difference between the system charge (mass) and the charge (mass) bounded in the QP and QT is quoted, comparing the n-rich and mixed systems. The results for Z (left panel of fig. 4.3) are the same

for the two systems, while a slightly more mass deficit (right panel of fig. 4.3) in the heavier symmetric reaction, as expected, signaling weaker neutron emission. From fig. 4.3 one evinces that AMD suggests a net transfer of proton from ^{40}Ca to ^{48}Ca in the mixed system.

In fig. 4.4 we continue the characterization of the of QP and QT primary fragments at 500 fm/c, showing the average excitation energy (panel a-c) and angular momentum (panel b-d), always as a function of b_{red}. Both reach a saturation value, for b_{red}<0.8, of approximately 100 MeV and 6 $\hbar$ of excitation energy and angular momentum, respectively. We need to mention that the relatively low angular momentum values of fragments produced by AMD has been already pointed out in a recent investigation [98]. Piantelli *et al.* tested a modified version of the AMD code which produces fragment with larger angular momentum: however, since this version of AMD does not produce important changes on the observables considered in this work, we preferred to use the standard code implementation.

We now introduce the neutron to proton ratio N/Z of a fragment type (we limit to only the QP), a variable commonly used in analysis in the Fermi energy domain [24, 102]. Fig. 4.5 shows the evolution of the average N/Z ($\langle N/Z \rangle$ in the following) of the QP as a function of b_{red}, (panel a) with the stiff AMD recipe and (panel b) the asy-soft one. Colors represent the different systems according to the convention previously introduced; full symbols refer to primary QPs, open symbols to secondary QPs. Indeed, we want to control and evidence the distortion on the $\langle N/Z \rangle$ introduced after the secondary decay which are the only experimentally accessible particles.

Concerning the primary events we observe that in each system the average neutron to proton ratio starts from the $\langle N/Z \rangle$ of the respective projectile ($(\frac{N}{Z})_{^{48}Ca} = 1.4$ and $(\frac{N}{Z})_{^{40}Ca} = 1$), and then it decreases (increases) as the centrality increases in the reaction with a ^{48}Ca (^{40}Ca) beam. We observe that the difference of the two ^{48}Ca induced reactions is the evidence of the expected isospin diffusion that the AMD model predicts. Slight differences are present between the asy-stiff and asy-soft parametrization in the n-rich and mixed system: in the former simulation the QP is more neutron rich than in the latter. This can be explained with the less repulsive restoring force for neutron in the (small) regions explored at sub-saturation densities (see fig. 4.1) when using the asy-stiff parametrization. The ^{40}Ca+^{40}Ca system is almost unaffected by the change of the symmetry energy parametrization. The secondary decay, as expected, dramatically changes the trend of $\langle N/Z \rangle$ *vs.* b_{red}. The evolution and hierarchy as a function of the centrality is still preserved, but the QP in the two systems, ^{48}Ca+^{48}Ca and ^{40}Ca+^{40}Ca, collapses to very similar neutron-to-proton ratios. This behavior is quite similar in the two parametrizations.

We also observe that for the most peripheral reactions (b_{red}>0.9) the average neutron to proton ratio of the (secondary) QP in the ^{48}Ca+^{40}Ca system is slightly larger than that in the ^{48}Ca+^{48}Ca. This effect is due to the following reason. Primary QP with b_{red}>0.9 have comparable charge and neutron number in ^{48}Ca+^{48}Ca and ^{48}Ca+^{40}Ca reaction, as shown in fig. 4.2(a,b). However, looking at the multiplicity of evaporated neutrons and hydrogen ions (fig. 4.7), we see that neutrons and neutron rich LCPs are more favorably

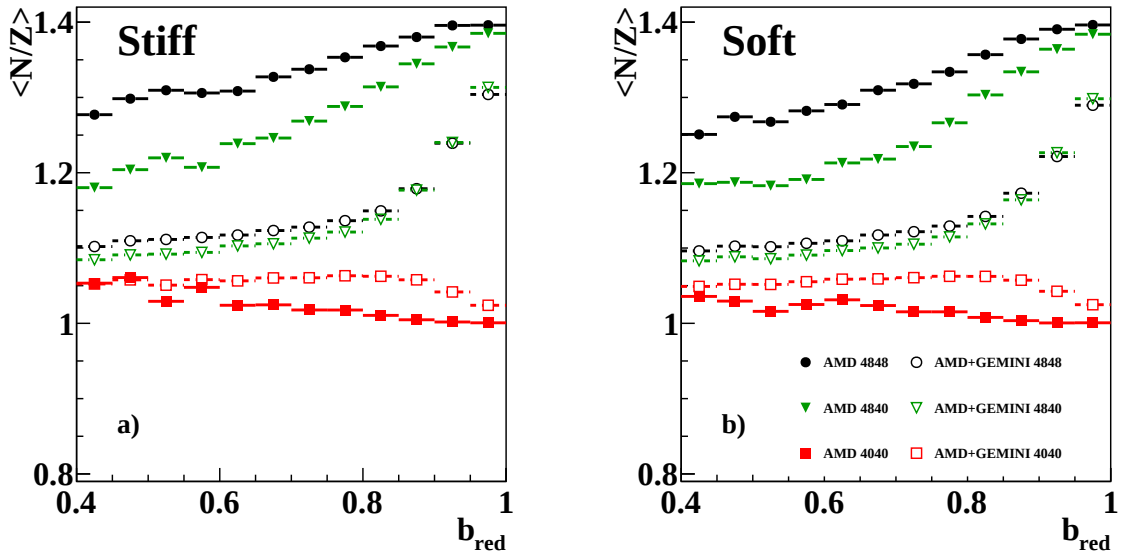

Figure 4.5: *Average neutron to proton ratio of the QP as function of the reduced impact parameter for each system. Full symbols refer to primary events, open symbols to secondary events. Results of the asy-stiff and asy-soft parametrization of the symmetry energy term are shown in panel a) and b), respectively.*

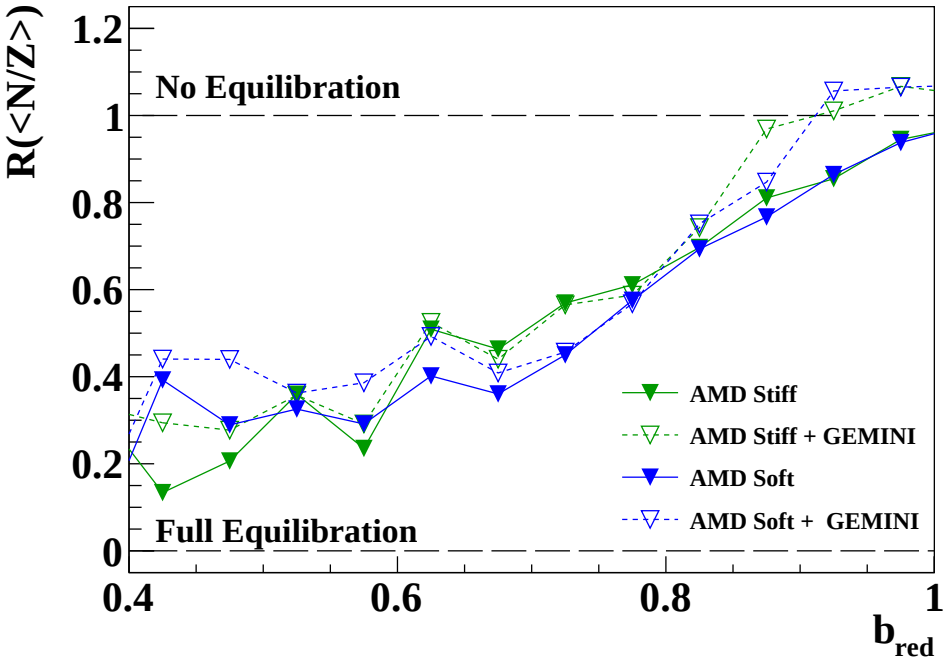

Figure 4.6: *Imbalance ratio of the average neutron to proton ratio of the QP in the ^{48}Ca+^{40}Ca system as a function of the reduced impact parameter. Primary and secondary QP for both the asy-stiff and asy-soft parametrization. Symbols according to the legend. Errors on the x-axis are not shown for clarity. Lines are drawing to guide the eyes.*

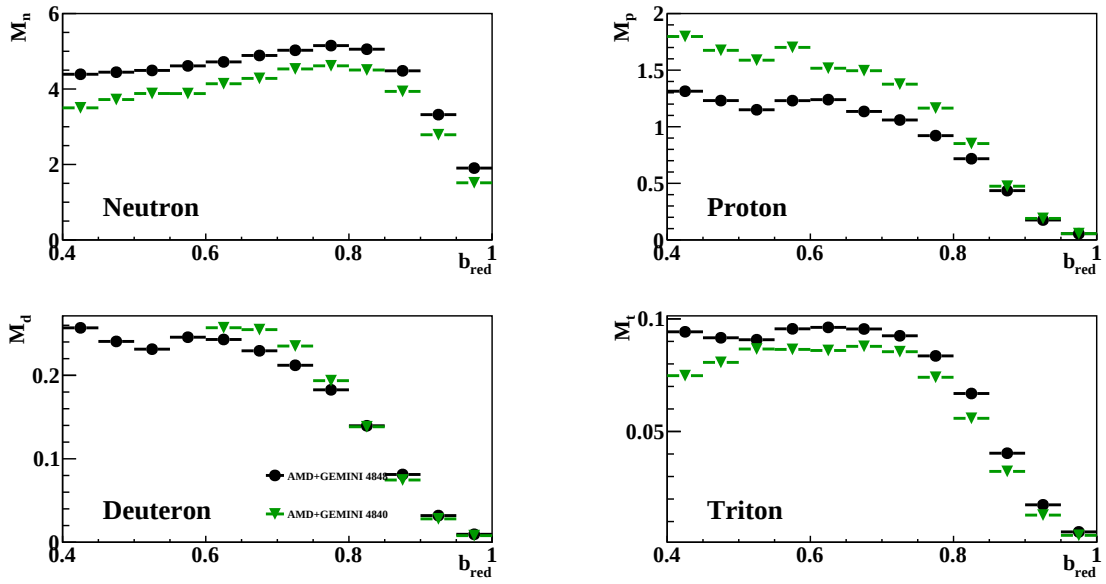

Figure 4.7: *Average multiplicity of neutron and hydrogen ions evaporated from the primary excited QP by GEMINI ad a function of the reduced impact parameter, for the ^{48}Ca+^{48}Ca and ^{48}Ca+^{40}Ca system.*

emitted in the ^{48}Ca+^{48}Ca case than in the ^{48}Ca+^{40}Ca, thus lowering the neutron content of the QP more in the former system than in the latter. This inversion does not occur in more central collisions because the initial difference is larger.

In order to enhance the observation of n-p equilibration process in the ^{48}Ca+^{40}Ca system, we can exploit the so-called imbalance ratio method, which, introduced by Rami *et. al* [8], takes advantage of the combined information of three systems. In particular this technique has been extensively used by the MSU group [9, 20, 61] (and references therein) as a probe for the isospin equilibration between projectile and target. According to the different models, the details of this process are sensitive to the asy-stiffness of the symmetry energy term of the nuclear equation of state [6]. In our case the three reactions are ^{48}Ca+^{48}Ca and ^{40}Ca+^{40}Ca (used as references) and ^{48}Ca+^{40}Ca. The imbalance ratio is defined as

$$R(X) = \frac{2X^{4840} - X^{4848} - X^{4040}}{X^{4848} - X^{4040}} \tag{4.11}$$

where X is an isospin sensitive observable, as the $\langle N/Z \rangle$ variable already introduced. For the two symmetric systems ^{48}Ca+^{48}Ca, ^{40}Ca+^{40}Ca, $R(X)$ is normalized to +1 and -1, respectively. The advantages of this method are the following. First, if the three reactions are investigated under the same experimental conditions, the imbalance ratio is insensitive to systematic uncertainties due to the apparatus; the errors are essentially of statistical nature. In particular, the imbalance ratio remains invariant if the experimental apparatus, or any other perturbation, introduces a linear transformation of the X observable. Second, the imbalance ratio $R(X)$ largely suppresses the effects of pre-equilibrium

emission and enhances the sensitivity to isospin diffusion between projectile and target [6, 9]. In particular, if the chosen variable linearly depends on the isospin of the system $R(X) = 1$ represents the "No Equilibration" limit, while $R(X) = 0$ the "Full Equilibration" line [8]. The closer $R(X)$ to +1, the less the equilibration in ^{48}Ca+^{40}Ca system; the closer $R(X)$ to 0, the more the equilibration. However, it is important to mention that the comparison between different systems is not straightforward. In particular different probes return different equilibration degree [62], and moreover it is strictly related to the dynamics of the collision, thus changing from system to system.

The obtained results, both for the primary and the secondary events, are reported in fig. 4.6, with symbols explained in the legend. We clearly see that the more damped the collision, the higher the level of isospin equilibration. In more details, the equilibration process evolves at an almost fixed pace with centrality, with some tendency to flatten below b_{red}<0.6. As a natural consequence of the independence of N/Z from the asy-stiffness (fig. 4.5), also R results, in the model, insensitive to the choice of the symmetry energy parametrization. This proves that, in the AMD calculation, we are not exploring density region far from the saturation density, where the larger differences between the asy-stiff and asy-soft arise (see fig. 4.1). This could be related to the relatively small size of the system with respect to heavier systems reported in literature, such as the aforementioned Sn+Sn case [9, 20]. Indeed, one can hypothesize that the larger the size of the system, the larger the probability to produce regions at sub-saturation density during the collision.

Finally we underline that, despite the fluctuations, the equilibration rate obtained from secondary events at b_{red}<0.9 is comparable with that calculated from primary events. This important observation is in agreement with the statement of ref. [20] where the authors affirm that the imbalance ratio bypasses also effects due to secondary decays. However, this is not the case at the largest b_{red}, where the secondary decay significantly deforms the trend of R, reaching also values larger than +1, due to the inversion in the average neutron to proton ratio previously observed.

CHAPTER 5

EVENT SELECTION AND GENERAL REACTION CHARACTERIZATION

After the calibration and identification procedure, described in chapter 3, the events accepted for the analysis contain particles (at least one) identified in charge (and mass, when possible). In this chapter the criteria adopted to separate the different reaction channels will be presented, as well as their gross properties. Moreover, the predictions of the transport model AMD, coupled with GEMINI++ as afterburner (in the following labelled only as AMD for sake of brevity), will be compared with the experimental results in order to guide and support the event selection.

Table 5.1: *Some parameters for the studied reactions; center of mass energy and velocity, beam energy and velocity in the laboratory frame, grazing impact parameter and angle in the laboratory frame; reaction and fusion cross section estimated with the Bass model [107].*

Reaction	$\mathbf{E_{cm}}$ [MeV]	$\mathbf{v_{cm}}$ [mm/ns]	$\mathbf{E_{lab}^{beam}}$ [MeV]	$\mathbf{v_{lab}^{beam}}$ [mm/ns]	$\mathbf{b_{gr}}$ [fm]	$\theta_{\mathbf{gr}}^{\mathbf{lab}}$ [deg]	$\sigma_{\mathbf{R}}$ [b]	$\sigma_{\mathbf{F}}$ [b]
^{48}**Ca+**^{48}**Ca**	840	41.12	1680	82.24	10.41	1.89	3.4	0.32
^{48}**Ca+**^{40}**Ca**	763	44.85	1680	82.24	10.06	1.95	3.2	0.29
^{40}**Ca+**^{40}**Ca**	700	41.12	1400	82.24	9.7	2.42	3.0	0.26

In table 5.1 some important reaction parameters are reported as indicated in the caption. We underline that the reaction[1] σ_R and fusion σ_F cross section are estimated with the Bass model [107]. We observe that the fusion channel (both complete and incomplete fusion) is a minority part of the total reaction channel, approximately $\sigma_{fus}/\sigma_{reac} \approx 9\%$. Although we know that this model is not optimized for the Fermi beam energies, the calculated value is in agreement with the experimental results reported in ref. [108], where the trend of $\sigma_{fus}/\sigma_{reac}$ as a function of the bombarding energies is shown for various

[1]The reaction cross section is defined as the difference between the total cross section σ_T and the elastic cross section σ_{el}, $\sigma_R = \sigma_T - \sigma_{el}$.

Table 5.2: *Number of events with at least one particle identified for each system.*

Reaction	^{48}**Ca+**^{48}**Ca**	^{48}**Ca+**^{40}**Ca**	^{40}**Ca+**^{40}**Ca**
Millions of events	110	70	13

systems. Moreover, such values are also in agreement with the systematics proposed in ref. [109], where the authors extract an "universal" fusion excitation function and show that, at the bombarding energies considered in this work, the fusion cross section is negligible part of the reaction one.

As done in chap. 4, since the grazing impact parameters slightly differ from system to system, decreasing as the total size of the system decreases, we will attempt to compare reactions as a function of the reduced impact parameter b_{red}. The impact parameter is not directly accessible as experimental observable, thus only an estimator of b_{red}, a kind of order variable, will be used during the analysis (sec. 6.1).

The available statistics of each system is reported in tab. 5.2. We remind that all the events have been acquired with a minimum bias condition, i.e. trigger multiplicity greater than or equal to one.

From now on, if not differently stated, errors on the y-axis are only statistical: if not visible, they are smaller than the marker size (line width).

5.1 Event selection

In this section the data selection is presented. Since the n-rich system is the most abundant one, we exploit this data set to present the adopted criteria. For sake of clarity, we introduce (or remind) some abbreviation used in the following:

- LCP - Light Charge Particles, $Z = 1$ and $Z = 2$;
- IMF - Intermediate Mass Fragment, $Z = 3$ and $Z = 4$;
- BF - Big Fragment, $Z \geq 5$.

In particular, we underline that the choice to select only $Z = 3$ and 4 as IMF is due to the fact that, according to GEMINI (cfr. sec. 4.2), they can be evaporated from the QP, while heavier fragments can be breakup products.

Fig. 5.1(a) shows the event multiplicity distribution (M) considering all the ejectiles identified in charge (black line), without requiring the mass identification. Once the detection of at least one BF is imposed, the red filled histogram is obtained. These are around 60% of the total detect events. The remaining 40% is related to events where only LCP and/or IMF are detected: this class of events is not used in the following analysis as we are interested to the QP characterization, and it will be only used for normalization purposes. For events with at least one BF ($M_{\mathrm{BF}} \geq 1$), LCP and IMF multiplicities are

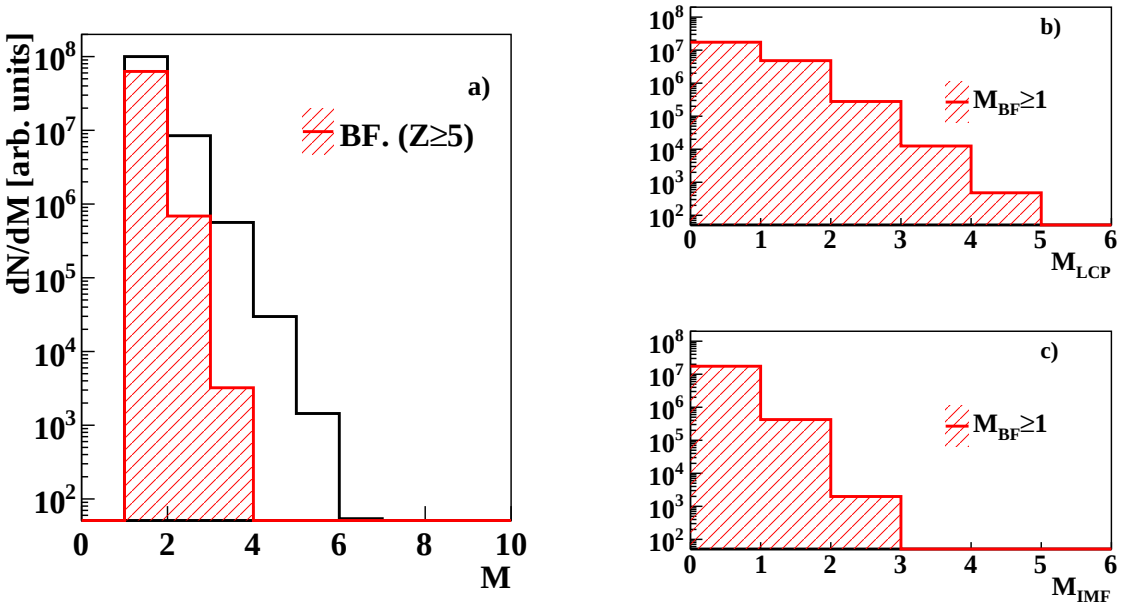

Figure 5.1: *(a) Multiplicity for all ejectiles (black) and for events with at least one Big Fragments (BF, red filled area). (b,c) LCP and IMF multiplicity distributions for events with at least one BF detected in coincidence.*

shown in figg. 5.1(b,c), respectively. We observe that in most cases the BF is detected alone: this is mainly due to the limited angular acceptance of the experiment (cfr. sec. 3.2) and to the trigger condition. Despite that, there is a sizable fraction of events where the BF is accompanied by other species.

5.1.1 Selection of the QP evaporation and breakup channels

As explained in the chap. 3, we aim to explore the isospin dynamics for two different event classes: the first one where the projectile interacts with the target and then decays through the emission of only LCP and/or IMF; the second one where the projectile splits in two comparable fragments. A first rough selection of such classes can be done via BF multiplicity conditions. $M_{\mathrm{BF}} = 1$ selection contains events where the QP remnant is detected, without any condition on possible accompanying LCP and/or IMF; $M_{\mathrm{BF}} = 2$ selection contains the QP breakup. These two classes are the most populated, according to fig. 5.1(a). We observe that such multiplicity condition is just a starting point to our event selection: indeed, due to the scarce angular coverage of our experimental apparatus we can miss another or more fragments per event. In the following we will characterize these two selected classes in order to properly select, with additional cuts, the QP remnant and the QP breakup channels.

As a first inspection of these two event classes, the correlation between the charge (Z) and the parallel velocity (v_{par}) in the laboratory frame [64, 110, 111] is presented in

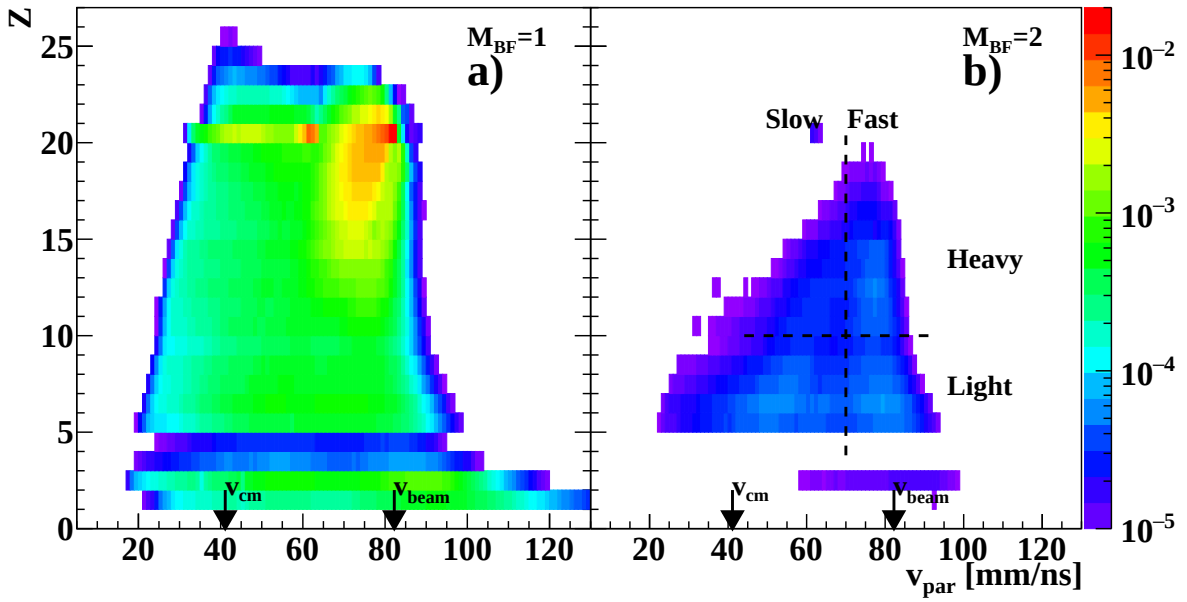

Figure 5.2: *Experimental correlation between the charge and the parallel velocity, for event classes BF=1 (a) and BF=2 (b). The center of mass velocity v_{cm} and the beam velocity v_{beam} are indicated. The counts are normalized to the number of events with at least one fragment.*

fig. 5.2(a,b). Both are normalized to the number of events with at least one BF, i.e. the area of the red filled distribution in fig 5.1(a). The "charge *vs.* parallel velocity" correlation presents different characteristics for the two selections. The correlation shown if fig. 5.2(a) is similar to those presented in literature (see for instance fig. 1 of ref. [110]). It mainly fills the charge region $12 \leq Z \leq 22$, with parallel velocity between 60 and 80 mm/ns. Both charge and velocity are compatible with a BF that is the QP remnant after the de-excitation through the emission of LCP and/or IMF. In particular, it corresponds to a projectile which, after the interaction with the target and the decay, retains up to 60% of its initial charge: such charge range complies with the typical QP charge domain adopted in literature [64, 111]. Thus we define QP, a BF with $Z = 12 \div 22$.

Since this QP charge range is somewhat arbitrary we will explore how this choice affects the main results of chap. 6 varying the QP charge range. This will be discussed afterwards but we anticipate that the conclusions are essentially unaffected by reasonably different QP charge range definition. Moreover, we observe that, once $M_{\mathrm{BF}} = 1$, the FAZIA data can be compared with the INDRA+VAMOS data, since we remind that VAMOS spectrometer detects only one (big) fragment per event.

Fig. 5.2(b) shows the "charge *vs.* parallel velocity" correlation for events that we mostly ascribe to QP decay via a process similar to breakup. We note that in this selection additional IMF are negligible whilst some LCP can be present in the events. We observe, in the plot, the presence of four loci:

- Heavy-Fast fragments → fragments with $Z \geq 10$ and v_{par} >70 mm/ns;

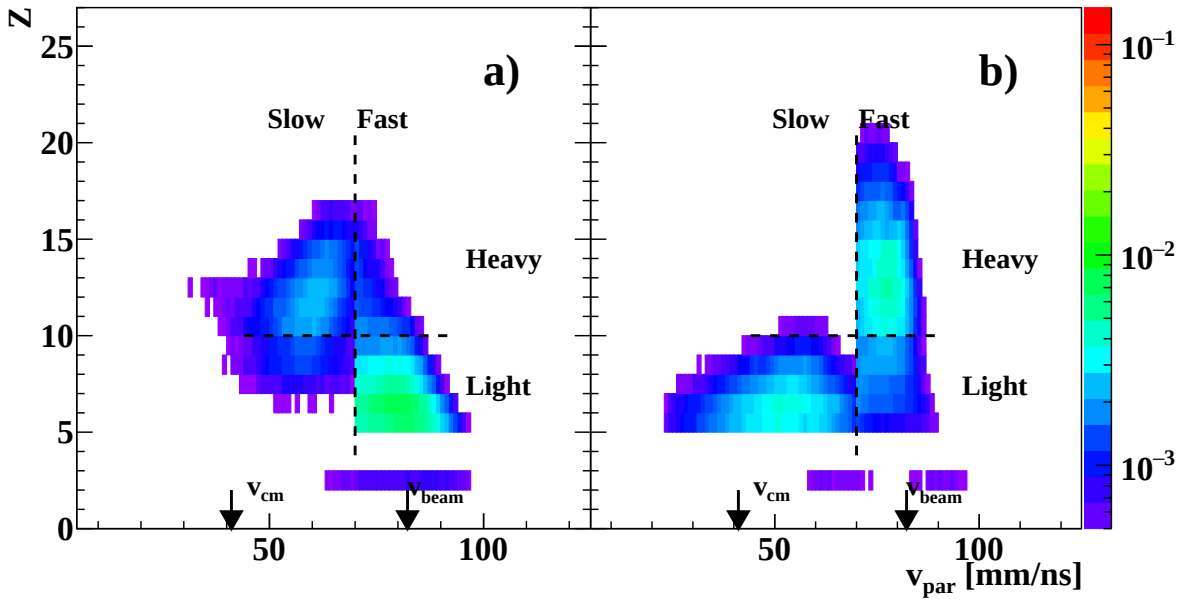

Figure 5.3: *Correlation between the charge and the parallel velocity for events with M_{Frag}=2, (a) gating on the Light-Fast fragments, (b) gating on the Heavy-Fast fragments. See text for details. Both histograms are normalized to unitary area.*

- Heavy-Slow fragments → fragments with $Z \geq 10$ and v_{par} <70 mm/ns;
- Light-Fast fragments → fragments with $Z < 10$ and v_{par} >70 mm/ns;
- Light-Slow fragments → fragments with $Z < 10$ and v_{par} <70 mm/ns;

In order to understand how these four loci are correlated, we gate on the Light-Fast and Heavy-Fast fragments (according to the gates shown in fig. 5.2), and the results are shown in fig. 5.3(a,b), respectively. One sees that Light-Fast fragments are mainly correlated to Heavy-Slow fragments, while Heavy-Fast fragments with Light-Slow ones.

We can imagine three possible scenarios, depicted in fig. 5.4, corresponding to the three main output channels of a dissipative collision. First (panel a), we are detecting both BFs related to the QP breakup. Second (panel b), we are detecting a QP remnant in coincidence with a Light-Slow fragment related to the QT split (and emitted toward the CM). Third (panel c), we are detecting both the QP and the QT remnants of a two-body event. This last scenario can be easily excluded. Indeed, since we are dealing with a symmetric system, the QT charge range is, on average, equal to the previously defined QP charge range. Since the only BF moving with $v_{par} < v_{cm}$ are with $Z < 10$ (fig. 5.2(b)), they are not associated to the QT remnants.

We have now to distinguish between the scenarios depicted in fig. 5.4(a,b). In order to do that, we can correlate the relative angle, in the CM frame, between the two detected BFs (θ_{rel}) and their relative velocity (v_{rel}), as done in the fig. 5.5 for the experimental

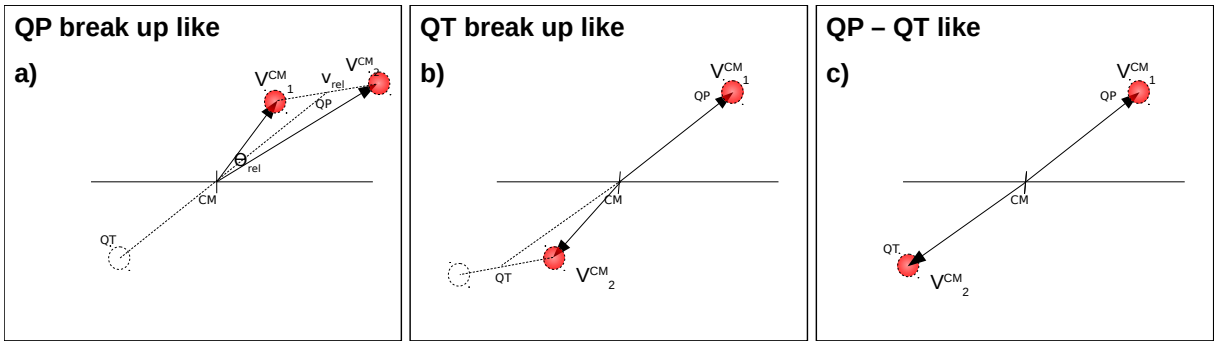

Figure 5.4: *Scheme of the possible scenarios. a) Detection of both fragment related to the QP breakup. b) Detection of the QP remnant and of a fragment related to the QT breakup. c) Detection of QP and QT remnants. The two detected fragments are shown in red.*

data. If both BF are compatible with a QP split, θ_{rel} has to be small and v_{rel} values should correspond to a Coulomb-driven repulsion [112]. On the contrary, if one of the two detected BF comes from a QT breakup, θ_{rel} assumes values close to 180° and v_{rel} is not ruled by the Viola systematics.

In fig. 5.5 we observe that the events mainly fill the region compatible with a QP breakup scenario; only a small fraction of events ($< 10\%$) are ascribable to coincidence between a QP and a fragment from a QT breakup. In order to clean the class of events containing the QP breakup, we select the good events as those contained in the red rectangle of fig. 5.5. Such selection represent the 70% of the events related to the QP phase-space: the exclusion of the remnant part does not bias the results described in the following of this work.

Having verified a common origin for the two BF (a QP rupture in two pieces) one can reconstruct the assumed parent nucleus by summing the charge ($Z^{rec} = Z^H + Z^L$, with Z^H and Z^L the charge of the Heavy and Light fragment) and the corresponding masses of the two fragments. Also we can assign to the parent QP the velocity of the CM of the pair. We consider as good QP candidates those with Z^{rec} falling in the previously assumed QP charge range ($12 \div 22$).

Summarizing, two event classes have been selected: QP remnant (QP_R) and QP breakup (QP_B) selection.

1. QP_R - events where the projectile interacts with the target and then decay trough the emission of LCP and/or IMF; this class of events is selected with the cuts
   - $M_{\mathrm{BF}} = 1$;
   - $12 \leq Z \leq 22$
   - fragment with $v_{par} > v_{cm}$;
2. QP_B - events where we detect two BF, compatible with a QP splits. This class of events is selected with the cuts
   - $M_{\mathrm{BF}} = 2$;

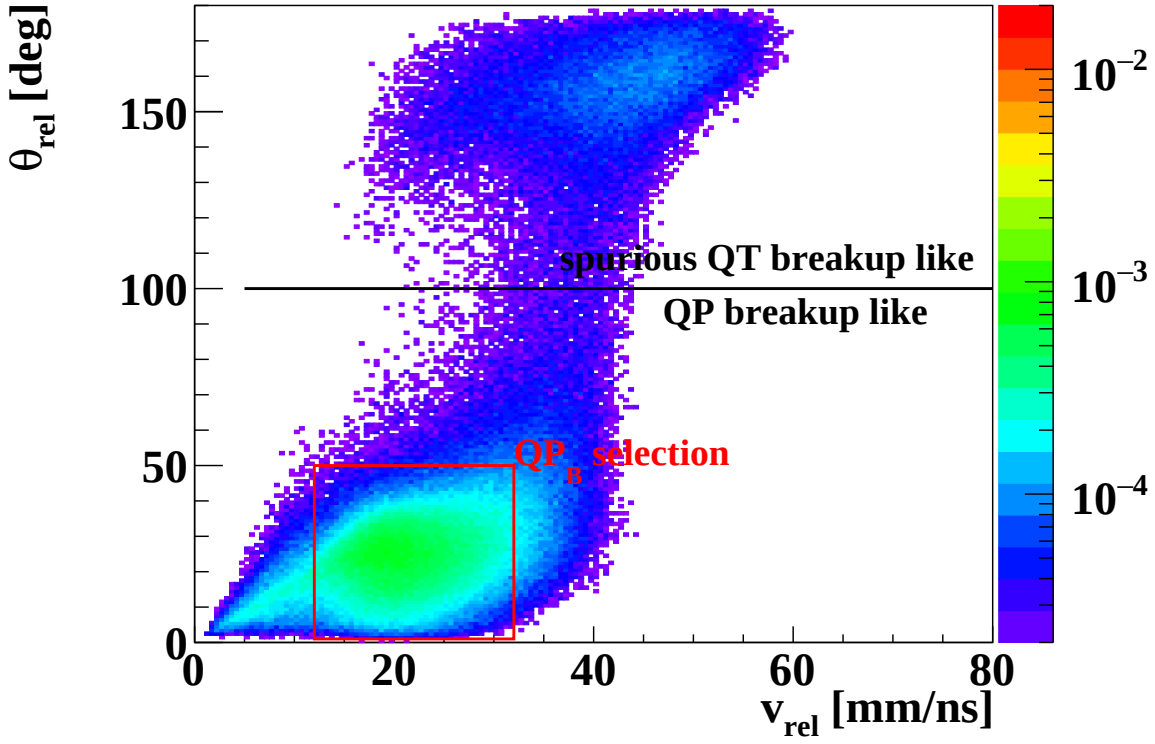

Figure 5.5: *Experimental correlation between the relative angle in the CM frame and the relative velocity, for the event class BF=2.*

- $12 \leq Z^{rec} \leq 22$
- $\theta_{rel} < 50°$ and $v_{rel} \in [12, 32]$ mm/ns

We conclude this section by remarking the underlying symmetries in our reactions. The reactions are almost or exactly symmetric; therefore whatever event class we imagine for the QP, there is the equal corresponding class for the QT. However the QT classes are strongly unfavoured due to the detector geometry and thresholds, thus they are here completely neglected.

5.2 Gross properties of the reaction mechanism

While the details of the isospin dynamics will be carefully examined in the chap. 6, we will present and discuss here many properties of the selected reaction channels. The characterization will concentrate on the ^{48}Ca+^{48}Ca and ^{40}Ca+^{40}Ca systems for both the QP$_R$ and QP$_B$ selections. The mixed system ^{48}Ca+^{40}Ca, as expected, behaves quite similarly to the n-rich one, since we focus on the QP properties and that in both cases the projectile is the same.

The important aspect is that our experimental results will be compared with the AMD filtered predictions (cfr. chap. 4), both to check the selections and to shed light on the reaction mechanisms. From now on we retain only fragments identified both in charge and mass, as this exclusive sample will we used to explore the isospin dynamics. Since we are interested to dissipative collisions where isospin transport mechanism occurs, we removed elastic events still present in the QP_R selection: on the other side, AMD simulation does not contain the elastic scattering, thus the removal of such events allows a more trustworthy comparison. We mention that this is one of the first attempts to systematically compare the experimental results with the AMD prediction in non central collisions, and it follows the recent publication of our group on Nb+Nb peripheral and semi-peripheral collisions [75].

Preliminary, the measured relative percentages of the event classes can be compared with the model predictions, as quoted in tab. 5.3, for both filtered and unfiltered (AMD 4π) events (cfr. chap. 4). The percentages are evaluated with respect to the total number of events for each system. On the experimental side, the dominant event class is the QP_R selection, which represents most of the measured yield[2]. The QP_B selection is a minority part of the statistics (as seen also in fig. 5.2(a,b)) due to the low production probability (the AMD 4π predicts about 10% with respect to the QP_R case) and to the limited experimental efficiency. As for the model, it fairly well reproduces the branching ratios of the events of the n-rich system, while it underestimates the n-deficient probabilities.

Table 5.3: *Experimental and model predicted percentages of the two QP_R and QP_B event classes as selected from a total amount of data.*

	Exp. data		**AMD data**		**AMD 4π data**	
	n-rich	**n-deficient**	**n-rich**	**n-deficient**	**n-rich**	**n-deficient**
QP_R	44%	43%	44%	34%	62%	62%
QP_B	0.5%	1.4%	0.4%	0.3%	5.7%	2.5%

5.2.1 QP remnants

Fig. 5.6(a) and fig. 5.7(a) show charge of the QP remnants Z^{QP} *vs.* v_{par}, for the n-rich and n-deficient systems respectively. We remind that only nuclei identified both in charge and mass are here considered. We note that the QP distribution extends to heavier species for the n-rich system with respect to the ^{40}Ca reaction. The parallel velocity distribution is similar in both cases. These features seem to be well reproduced by the AMD (filtered) simulations, as we can see comparing the simulated results in fig. 5.6(b) and fig. 5.7(b), for the n-rich and n-deficient system, respectively.

Major details can be appreciated by looking at the QP charge (fig. 5.8), velocity (fig. 5.9) and the diffusion agle (fig. 5.10) distributions. The histograms are represented

[2]We remind that the approximately 40% of the total detected events consist of only LCP and/or IMF (cfr. sec. 5.1)

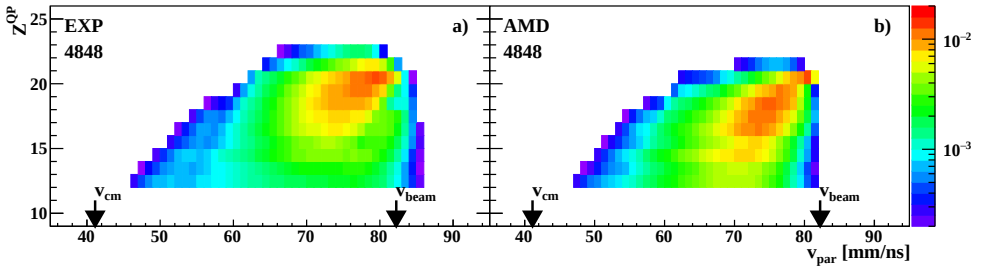

Figure 5.6: *QP_R selection. Charge vs. parallel velocity distribution for the ^{48}Ca+^{48}Ca system. Only fragments identified both in charge and mass are considered. Histograms are normalized to unitary integral.*

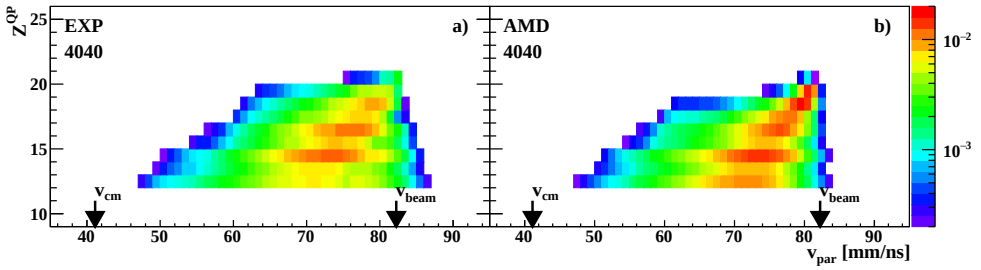

Figure 5.7: *QP_R selection. Same as fig. 5.6 for the ^{40}Ca+^{40}Ca system*

in black for the n-rich and in red for the n-deficient reaction, respectively, and this choice is the default choice that we adopt in the following, unless otherwise declared.

As for the charge distributions, they clearly appear different (as it could be already seen in the bi-dimensional plots). In particular, as said, the n-rich reaction can form QP_R heavier than the projectile with sizable cross section while the yield beyond $Z = 20$ is quite low for the ^{40}Ca system. This lack is related to the deficit of neutrons of ^{40}Ca with respect to ^{48}Ca, that does not allow the production of QP_R heavier then the projectile. The same evidences have been found in ref. [69] in the INDRA+VAMOS data. Moreover, the shape of the distribution for the n-rich system is smooth (evidently for experimental data) while a strong odd-even staggering effect is appreciable in the ^{40}Ca reaction.

The staggering effect is a quite general phenomenon and it has been observed in other systems by the FAZIA collaboration [113], as well as by the CHIMERA collaboration in Kr+Ca [114] and in Ca+Ca [115] reactions at lower bombarding energies. As found in our data, Lombardo *et al.* showed that the charge staggering effect is more evident in the n-deficient system. Qualitatively, this effect seems to be due to the last steps of the de-excitation chain that leads to the QP residue [115, 116].

The QP diffusion angle (θ_{cm}^{QP}) distribution (in the CM frame) is peaked at angles closed to the grazing angle and then the probability rapidly decreases at larger diffusion angles, as expected for binary dissipative collisions [1, 75].

Rather interestingly, the AMD model quite nicely reproduces the charge distribution for the n-deficient system while it follows less accurately that for ^{48}Ca. In general, AMD

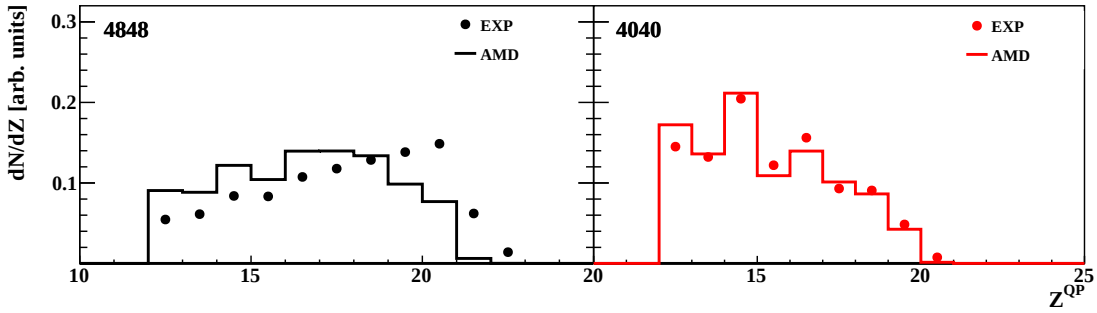

Figure 5.8: *QP_R selection. Experimental and simulated QP charge distribution for the ^{48}Ca+^{48}Ca (left) and the ^{40}Ca+^{40}Ca (right) system. Only fragments identified both in charge and mass are considered. Histograms are normalized to unitary integral.*

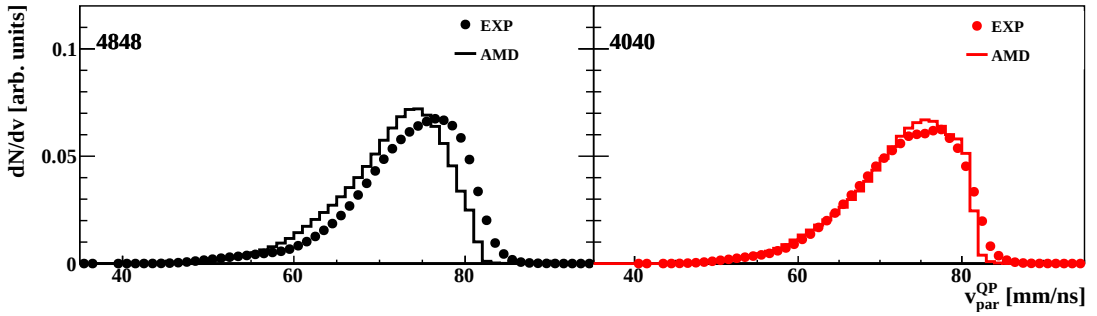

Figure 5.9: *QP_R selection. Experimental and simulated QP parallel velocity distribution for the ^{48}Ca+^{48}Ca (left) and the ^{40}Ca+^{40}Ca (right) system. Only fragments identified both in charge and mass are considered. Histograms are normalized to unitary integral.*

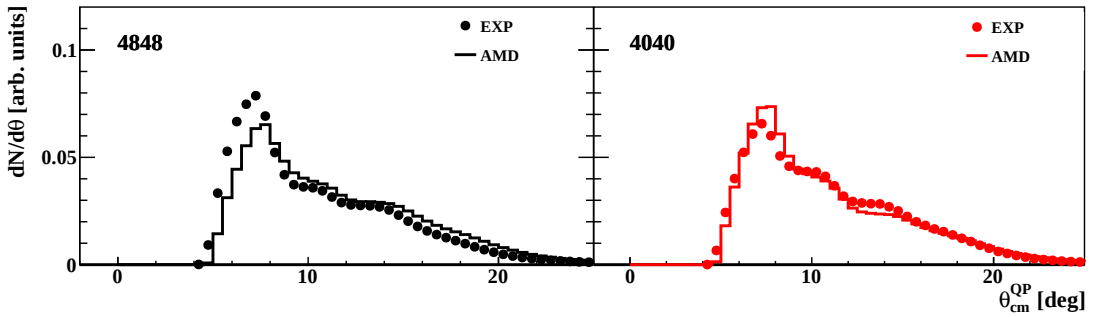

Figure 5.10: *QP_R selection. Experimental and simulated QP polar angle distribution for the ^{48}Ca+^{48}Ca (left) and the ^{40}Ca+^{40}Ca (right) system. Only fragments identified both in charge and mass are considered. Histograms are normalized to unitary integral.*

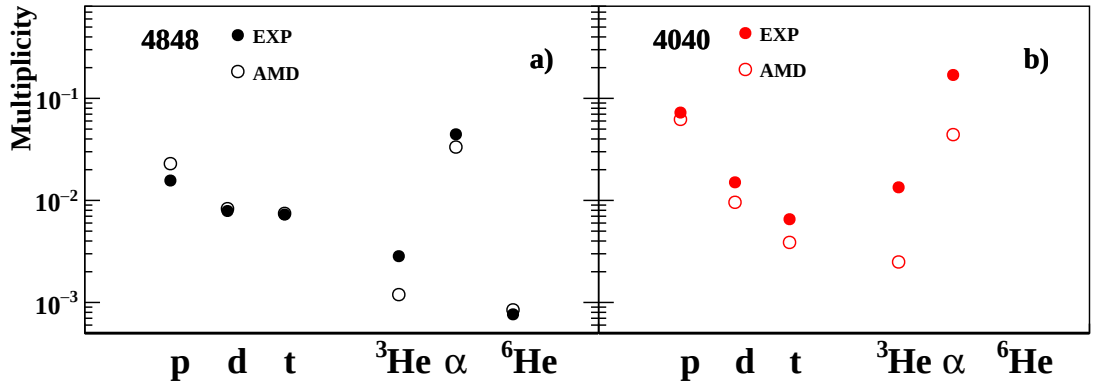

Figure 5.11: *QP_R selection. Average LCP multiplicity. Symbols according to the legend.*

penalizes the high-Z yield. Concerning the parallel velocity, AMD nicely reproduces the n-deficient distribution, while a shift towards lower velocity is present in the n-rich case. As for the diffusion angle, AMD nicely reproduced the n-deficient distribution but it unfavor events closer to the grazing angle in the n-rich system. These latter observations (similarly reported in ref. [30]) could suggest a stronger degree of dissipation in the model than that observed in the experimental data.

A further characterization can be done looking at the LCPs detected in coincidence with the QP_R. Fig. 5.11(a,b) shows the average LCP multiplicity, for the n-rich and n-deficient system, respectively. Each value is normalized to the total number of events belonging to the QP selection.

In both systems we observe that α particles are the most abundant emitted LCPs. This is a typical feature of reactions in the Fermi energy domain, as the produced excited fragment prefers to emit α particles to lose energy and angular momentum [117–119]. Moreover, in the n-deficient system, such characteristic has been related with a signature of the α-cluster nature of the ^{40}Ca. Indeed, Schmidt *et al.* [120], in an exclusive analysis on the ^{40}Ca exit channell, fully detected in charge and mass with the NIMROD-ISiS 4π detector array [121], show that the most probable decay modes are those with one heavy fragment and several accompanying α particles in the exit channel. They conclude that the α-conjugate nature of the ^{40}Ca can have an important dynamic contributions, and most of the α particles observed in such events are originated from α-conjugate neck structures formed during the collision.

We also observe that the LCP multiplicity is globally larger in the n-deficient system with respect to the n-rich one. Exceptions are tritons and ^{6}He ions that are more probably emitted in the n-rich case: in particular ^{6}He ions are undetected in the n-deficient system. Such characteristics is somewhat expected. Indeed, the neutron content differences of the entrance channels are reflected in the neutron composition of the emitted LCP (as well as in neutron multiplicity, but such particles are not detected by the apparatus). The AMD simulation globally well reproduces the experimental results in the ^{48}Ca+^{48}Ca case,

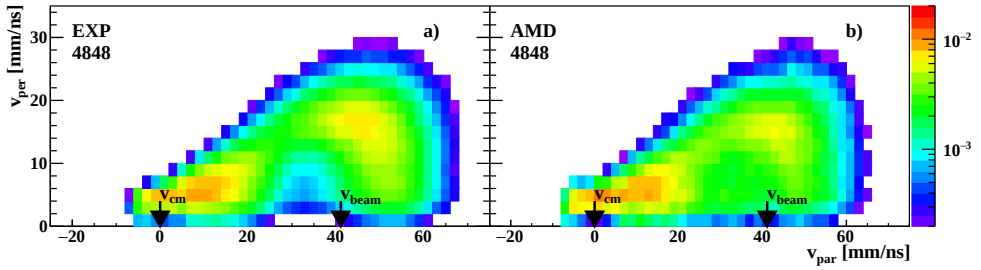

Figure 5.12: *QP_R selection. Correlation between the parallel (v_{par}) and perpendicular (v_{per})components of the velocity of the α particles with respect to the QP direction in the CM.*

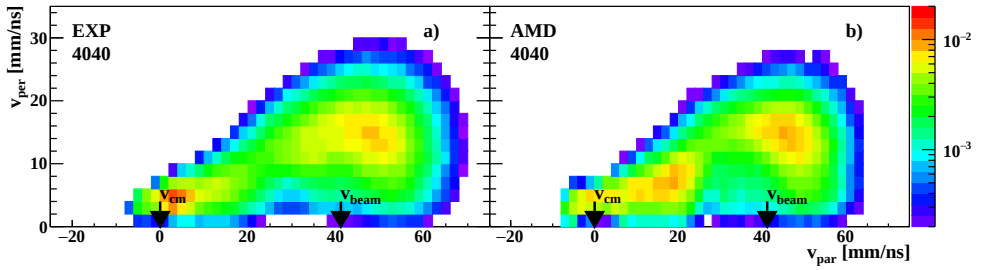

Figure 5.13: *QP_R selection. Same as fig. 5.12 for the ^{40}Ca+^{40}Ca system.*

while some underestimation for the ^{40}Ca+^{40}Ca reaction is present. This general behavior agrees with the results published in ref. [75] for Nb+Nb collisions: in the systematic comparison of the AMD+GEMINI predictions with the experimental data, the authors show that the total emitted charge by means of LCPs is generally reproduced by the models, while some discrepancies remains for the multiplicities of the various species. They attempted to recover such lacks varying some parameters of the AMD+GEMINI simulation, as the screening parameter of the in-medium cross section, the switching time between the primary simulation and the afterburner, as well as to different versions of the GEMINI code. Since the observed discrepancies have not been recovered modifying such parameters, we decided here to continue the analysis with the (standard) values described in sec. 4.1.

Fig. 5.12 and fig. 5.13 show the correlation between the parallel v_{par} and the perpendicular v_{perp} velocities of α particles with respect to the QP direction in the CM frame, both for the experimental (panel a) and simulated (panel b) results. The QP Coulomb ridges are evident in the pictures, while the corresponding ridges for the QT are practically absent. Only some marginal contribution could be ascribed to the QT emission in the region close to the CM. Of course this fact reflects the low efficiency of the setup to detect QT fragments and decay products. The yield thickenings and humps seen in the data are due to the discontinuous geometric efficiency. These effects are correctly taken into account in the simulation which rather faithfully reproduces the shape of the distributions.

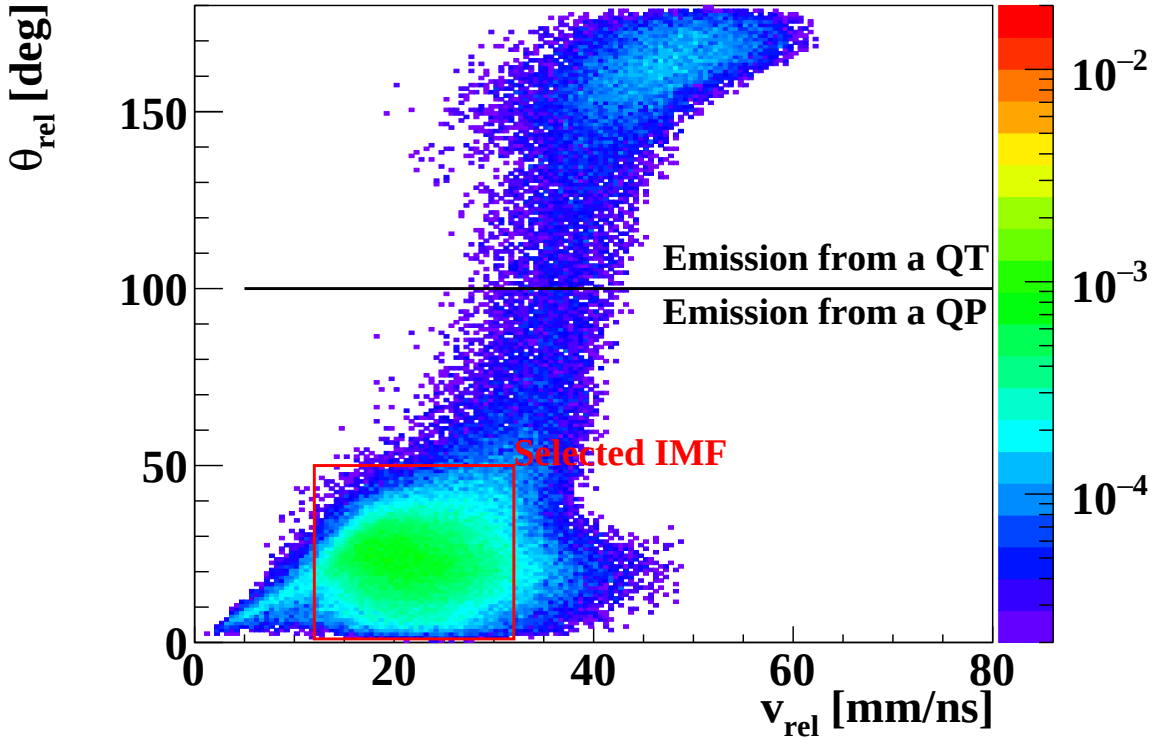

Figure 5.14: *QP_R selection. Experimental correlation between the relative angle in the CM frame and the relative velocity of QP_R and the IMF in coincidence.*

5.2.2 QP remnant with IMF in coincidence

We can consider the case of emission of an IMF from the QP as an intermediate channel between the QP emitting only LCP and QP splitting in two comparable pieces. When dealing with this subset of QP_R events with IMFs detected in coincidence, we have to take into account the contribution from the QT emission although penalized by the efficiency. Indeed, the θ_{rel} *vs.* v_{rel} correlation reveals (fig. 5.14) the presence of two regions compatible with the QP and QT emissions. Adopting the same criteria presented in sec.5.1, we select the IMFs compatible with an emission from a QP by means of the red contour. In the following the characteristics of such IMF will be presented.

The IMF multiplicities are quoted in fig. 5.15. As already observed for the LCPs, the measured IMF emission is larger for the ^{40}Ca case than for the ^{48}Ca reaction (fin detail or each species: $M_{Li}^{4848} = 1.8‰$, $M_{Li}^{4040} = 3.2‰$ and $M_{Be}^{4848} = 0.8‰$ $M_{Be}^{4040} = 1.8‰$). Moreover, the initial different neutron abundances is reflected in the neutron composition of the IMF. The AMD simulation reproduces the relative multiplicity, however in the n-deficient system the absolute values are underestimated of at least a factor three. A better agreement is found for the n-rich system, especially for the Be ions. The discrepancy is similar to what observed for the LCPs.

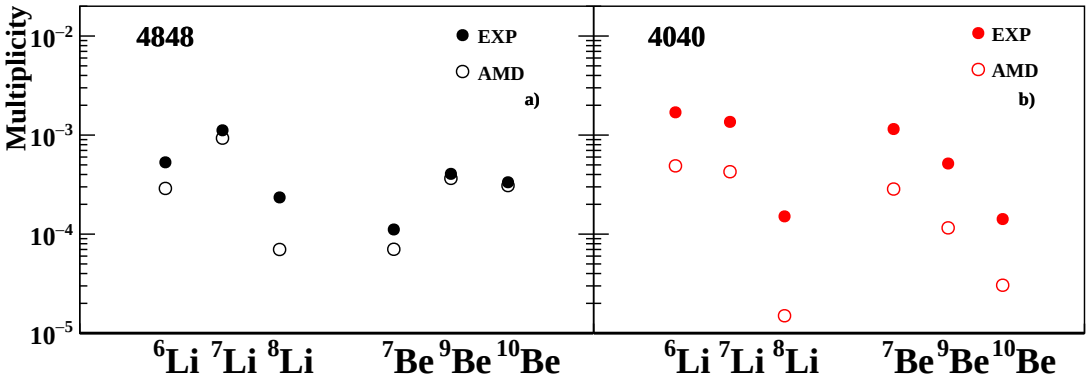

Figure 5.15: *QP_R selection. Average IMF multiplicity. Symbols according to the legend.*

In order to characterize the IMF emissions we introduce the α angle frequently used in this field (see refs. [14, 102, 110, 122]). Assuming an emission of the IMF from an excited (and possibly deformed) QP, the α angle corresponds to the angle between the direction of the center of mass velocity of the original emitting nucleus ($\vec{v}^{QP^*}$) and the direction of the relative (asymptotic) velocity ($\vec{v}_{rel} = \vec{v}^{QP^*} - \vec{v}^{IMF}$) after the split:

$$\alpha = \arccos\left(\frac{\vec{v}^{QP^*} \cdot \vec{v}_{rel}}{|v^{QP^*} v_{rel}|}\right) \tag{5.1}$$

We assume $\alpha = 0°$ when the IMF is emitted aligned with the $\vec{v}^{QP*}$ backward towards the CM, while for $\alpha = 180°$ the IMF is forward emitted with respect to the QP. In a semi-classical picture, the α angle is related to the time scale of the process: the smaller the α angle, the faster the emission mechanism, provided we can assume a rather constant rotation velocity. In particular, IMF emitted backward, towards the CM, could manifest features more related to the interaction dynamics (a kind of neck breakup); IMF flying forward with respect to the QP are expected to be emitted through the "standard" statistical decay of a hot spinning QP source. A dedicated investigation taking into account the chemistry of the emitted fragments will be presented in chap. 6.

The experimental results are shown in fig. 5.16, together with the simulated ones. Each distribution is normalized to unitary area for a shape comparison. Due to the limited angular coverage of the apparatus, as expected, we observe a strong deformation of such distribution. In particular, emission configuration with large transverse momenta ($\alpha \sim 90°$) are unfavoured, as shown comparing the AMD 4π distribution with the filtered one in panel b). This feature is well taken into account by the geometrical filter, and, indeed, the AMD predictions are in global agreement with the experimental result. Rather interesting, in both systems, the backward emission seems somewhat favored, compatible with the results present in literature [30, 102, 110, 123].

Finally, from the IMF detected in coincidence with the QP_R, a QP can be reconstructed following the same recipe for the QP_B channel (cfr. sec. 5.1). Indeed, this kind

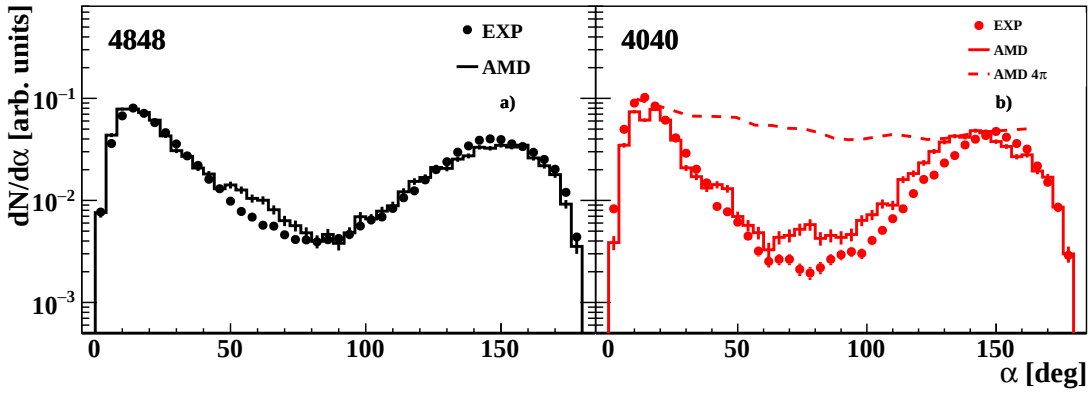

Figure 5.16: *QP selection. α angle distribution for the IMF detected in coincidence with the QP remnant. Each distribution is normalized to unitary area. Panel b) also shows the distribution obtained before the apparatus filter (AMD 4π). Symbol according to the legend*

of emission can be linked with the QP_B channel if we consider it as a very asymmetric breakup of the QP into a QP_R and IMF. In chap. 6 we will compare the isospin dynamics of the QP_R+IMF channel with the QP_B channel; the main properties of QP_B event class are presented in following section.

5.2.3 QP breakup selection

As mentioned before, from the two detected fragments (labelled as Heavy and Light according to their size), event by event the QP can be reconstructed both in charge $Z^{rec} = Z^H + Z^L$ and mass $A^{rec} = A^H + A^L$ (both fragments are isotopically resolved); and we can assign to it the velocity of the center of mass of the pair ($\vec{v}^{rec}$). We note that here $\vec{v}^{rec}$ has the same definition of $\vec{v}^{QP*}$ in the case of IMF. However, to reinforce the operative distinction of the two classes of QP_R and QP_B we prefer to maintain a different symbol. In fig. 5.17 and fig. 5.18 the Z^{rec} *vs.* v_{par}^{rec} correlations are shown, for the n-rich and and n-deficient system respectively, for both the experimental (panel a) and simulated (panel b) data.

Similarly to the QP selection, we observe some differences between the n-rich and n-deficient reactions: in the former the charge distribution is centered around $Z^{rec} = 19$, while in the latter lighter QPs are populated, as more clearly appear in the Z^{rec} distribution in fig. 5.19. In both cases cases, v_{par}^{rec} distributions are centered around 68 mm/ns (fig. 5.20), and the reconstructed diffusion angle (θ_{cm}^{rec}) has an average value of about 7° (fig. 5.21).

The AMD description of QP_B selection is less successful that the QP_R one, showing discrepancies on both the charge and parallel velocity distribution. Smaller reconstructed QP are favored with respect to heavier ones (fig. 5.19) and the v_{par}^{rec} distributions are shifted towards lower velocities of about 5 mm/ns (fig. 5.20); the simulation favors larger reconstructed diffusion angles with respect the experimental results in both systems (fig. 5.21).

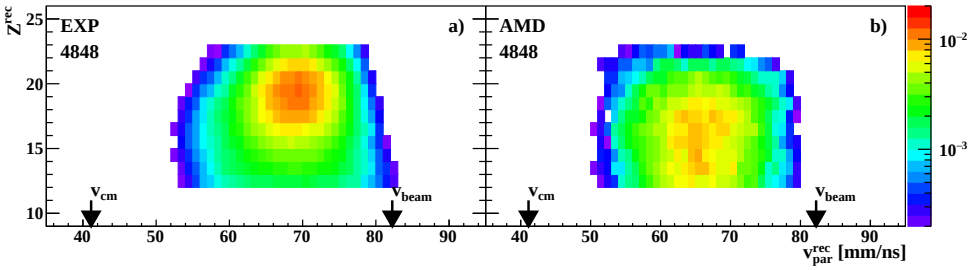

Figure 5.17: *QP_B selection. Charge vs. parallel velocity distribution of the reconstructed QP for the ^{48}Ca+^{48}Ca system. Only fragments identified in charge and mass are considered. Histograms are normalized to unitary integral.*

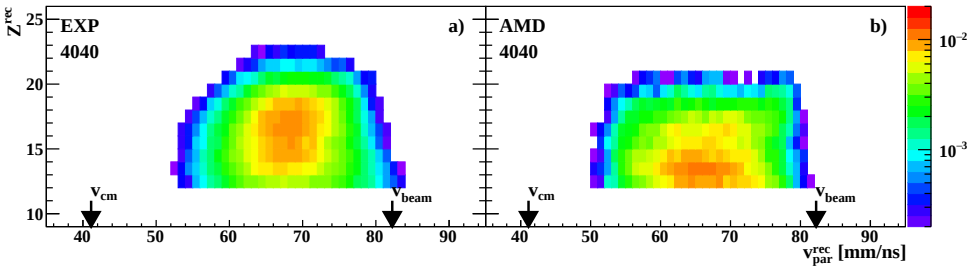

Figure 5.18: *QP_B selection. Same as fig. 5.17 for the ^{40}Ca+^{40}Ca system.*

Consequently, the chosen selections seems to pick out simulated events more damped than the experimental ones: this tendency has also been observed in other experimental data extensively compared with the AMD predictions [30]. However, the global description of the reaction given by the simulation is very reasonable.

In order to better characterize these kind of events we introduce the charge asymmetry parameter η, defined as

$$\eta = \frac{Z^H - Z^L}{Z^H + Z^L} \tag{5.2}$$

Fig. 5.22 shows the η distributions both for the n-rich (panel a) and n-deficient (panel b) system, experimental and simulated results. We can clearly observe that in the ^{48}Ca+^{48}Ca system the breakups populate a wider asymmetry range than for the ^{40}Ca+^{40}Ca; the model follows this results but, in any case, favoring too asymmetric splits.

In order to better address this point, in fig. 5.23 we plot the average reconstructed parallel velocity ($\overline{v_{par}^{rec}}$) as a function of different η bins. Errors on $\overline{v_{par}^{rec}}$ are statistical (smaller than the marker size), while errors on η represent the bin width. Some comments can be done. The more damped the collision, the more symmetric the split, as also observed in previous study (see fig. 2 of ref. [110] where the charge correlation of the fragment is shown for different bin of centrality). The evolution of $\overline{v_{par}^{rec}}$ with η could then signal an impact parameter ordering of the observed fission events, with the more asymmetric splits corresponding to slightly more peripheral collisions. The model follows the trend *vs.* the charge asymmetry of the measured data but it perhaps overestimates the

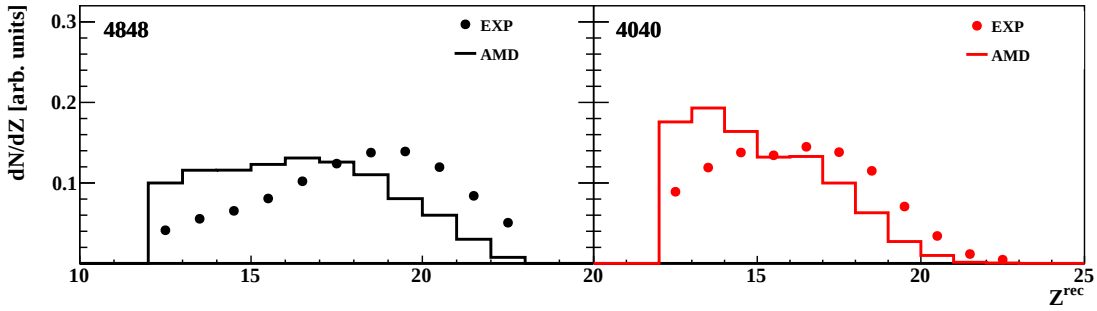

Figure 5.19: *QP_B selection. Experimental and simulated charge distributions for the reconstructed QP for both ^{48}Ca+^{48}Ca and ^{40}Ca+^{40}Ca systems. Histograms are normalized to unitary integral.*

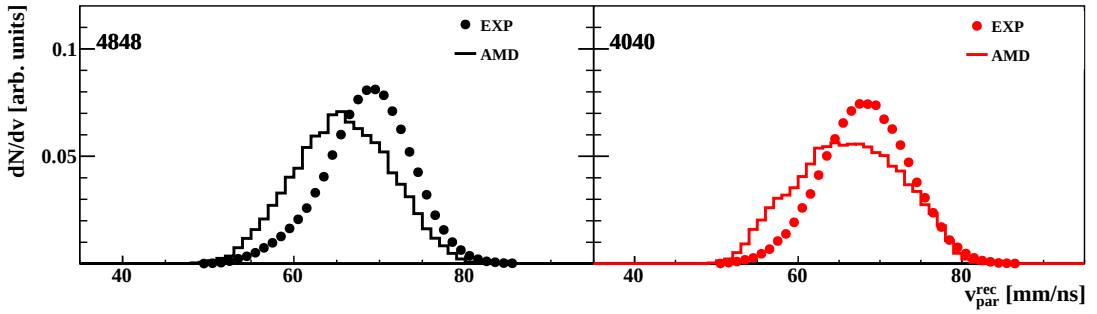

Figure 5.20: *QP_B selection. Experimental and simulated parallel velocity distributions for the reconstructed QP for both ^{48}Ca+^{48}Ca and ^{40}Ca+^{40}Ca systems. Histograms are normalized to unitary integral.*

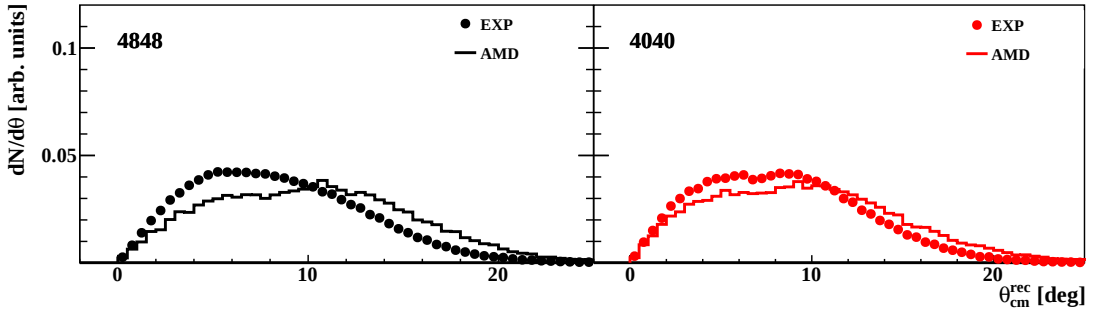

Figure 5.21: *QP_B selection. Experimental and simulated diffusion angle distributions for the reconstructed QP for both ^{48}Ca+^{48}Ca and ^{40}Ca+^{40}Ca systems. Histograms are normalized to unitary integral.*

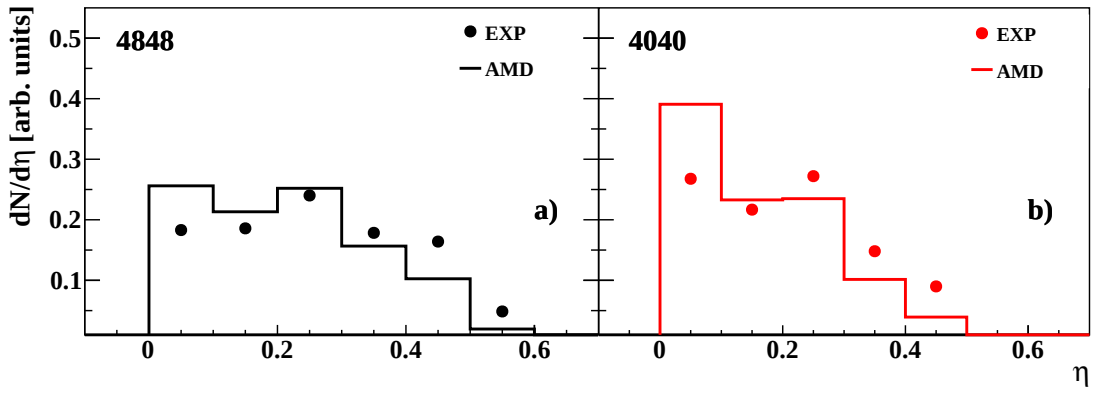

Figure 5.22: *QP_B selection. Probability of the charge asymmetry of the breakup.*

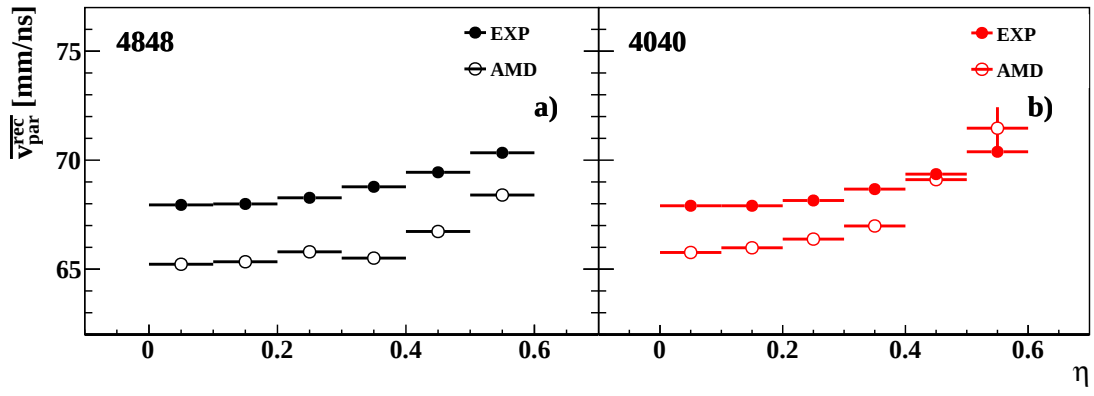

Figure 5.23: *QP_B selection. Average parallel velocity $\overline{v_{par}^{rec}}$ of the reconstructed QP as a function of the charge asymmetry η. Full dots experimental results, open dots AMD results. Errors on $\overline{v_{par}^{rec}}$ are statistical (smaller than the marker size), while errors on η represent the bin width.*

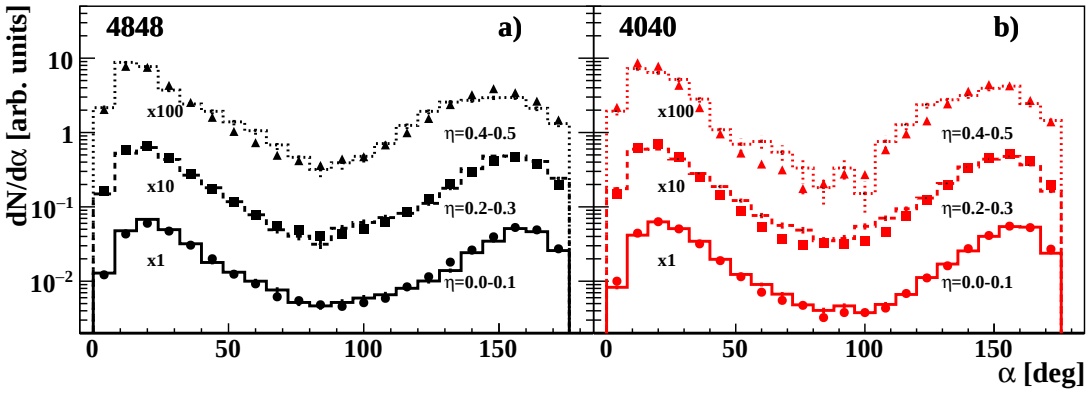

Figure 5.24: *QP_B selection. α angle probability for bins of charge asymmetry. Distribution related to $\eta = 0.2-0.3$ $(0.4-0.5)$ is scaled by a factor 10 (100) for sake of clarity. Experimental results are plotted with full symbols, simulated results with lines. Experimental and simulated distributions normalized to unitary area.*

Table 5.4: *Ratio between the backward emission probability and the forward emission probability of the light fragment with respect to the heavy one. For each η bin, error on the experimental value is 2%, while of 3% in the AMD results.*

	Exp. Data		**AMD Data**	
	n-rich	**n-deficient**	**n-rich**	**n-deficient**
$\eta = \mathbf{0-0.1}$	1.0	1.0	1.0	1.0
$\eta = \mathbf{0.2-0.3}$	1.1	1.1	1.1	1.1
$\eta = \mathbf{0.4-0.5}$	1.3	1.3	1.3	1.3

average dissipation of these events because the corresponding velocities are (on average) 3 mm/ns below the experimental data.

As last characterization of the QP breakup data set we can exploit again the α angle introduced before (eq.(5.1)). Fig. 5.24 shows the α angle distributions for three different bins of charge asymmetry. For sake of clarity, the distribution related to $\eta = 0.2-0.3$ $(0.4-0.5)$ is scaled by a factor 10 (100). Experimental results are plotted with full symbols, simulated results with lines. Before discussing the results, we remind that the depletion of the distributions around $\alpha \sim 90°$ is an artifact due to the limited angular acceptance, that penalize such configurations. We remark the excellent shape agreement between measured and simulated data.

As a comment, we can say that the most polarized splits, at around 0 and 180°deg, are the most populated. Also for more asymmetric splits, we observe a preferential emission of the light fragment towards the CM, in full agreement with the many similar findings in the literature [14, 102, 110, 123]. This is better evidenced in tab. 5.4 where the ratios between the backward and the forward emission yields are reported. At this level, our AMD+GEMINI simulations very well reproduce this finding that has been interpreted as due to the more dynamical nature of fast and asymmetric breakups.

In conclusion, the QP breakup selection contains events compatible with the hypothesized scenario of an excited and possibly deformed system which breaks apart in two fragments. The general measured features of this process are in close agreement with many other similar results reported in the literature [14, 102, 110, 111]. Notably, moreover, the model reasonably well reproduces the experimental findings; this kind of deep and extended comparison of the AMD model (+afterburner) with the characteristics of binary collisions at semi-peripheral collisions, is a specific activity of the FAZIA collaboration in recent years. Now we can even more go further in the study of these reactions and in the comparison with the AMD, also including the isospin degree of freedom of most detected fragments thanks to the unique identification capability of the FAZIA telescopes. The last chapter is devoted just to such investigation.

CHAPTER 6

ISOSPIN DYNAMICS

In this chapter we are going to deeply investigate the QP decay, taking into account the three different categories introduced in chap. 5.The QP evaporation (QP_R), the QP breakup (QP_B) and the QP_R with the emission of an IMF ($Z = 3, 4$), which can be considered as a limiting case of a very asymmetric breakup. In this chapter we will try to particularly investigate the isospin dynamics for those event categories. First, we will discuss the n-p equilibration, investigating how, in the mixed system, the ^{48}Ca QP tends to the equilibrium value of the entire system ^{48}Ca+^{40}Ca. To reinforce our findings, we will compare our results obtained by the INDRA+VAMOS experiment on the same Ca+Ca systems at the same bombarding energy. Second, we will discuss if the experimental results have some sensitivity to the stiffness of the symmetry energy of the nuclear nEoS. Here we use, as said, the molecular dynamics code AMD to predict the collision features and fragment production, with GEMINI++ as afterburner, to describe the decay of the excited products before reaching the ground state (for sake of brevity only the label AMD will be used in the following). Third, for the first time to our knowledge, the n-p equilibration investigation will be extended to the breakup channels and compared with the evaporative one in an homogeneous and consistent way. As last point we will investigate the neutron enrichment of the neck region, the so-called isospin drift, searching for the possible correlation between the neutron enrichment of the mid-velocity emitted fragments and the corresponding neutron depletion of the accompanying QP remnant [14, 25].

6.1 Reaction centrality estimation

Isospin diffusion is expected to drive the system towards the equilibrium as the reaction centrality increases. The subject rose the interest already several decades ago when the path towards equilibrium in various nuclear parameters was investigated with small (but often well designed) setups in dissipative reactions [18, 19, 124]. This physics case, in more

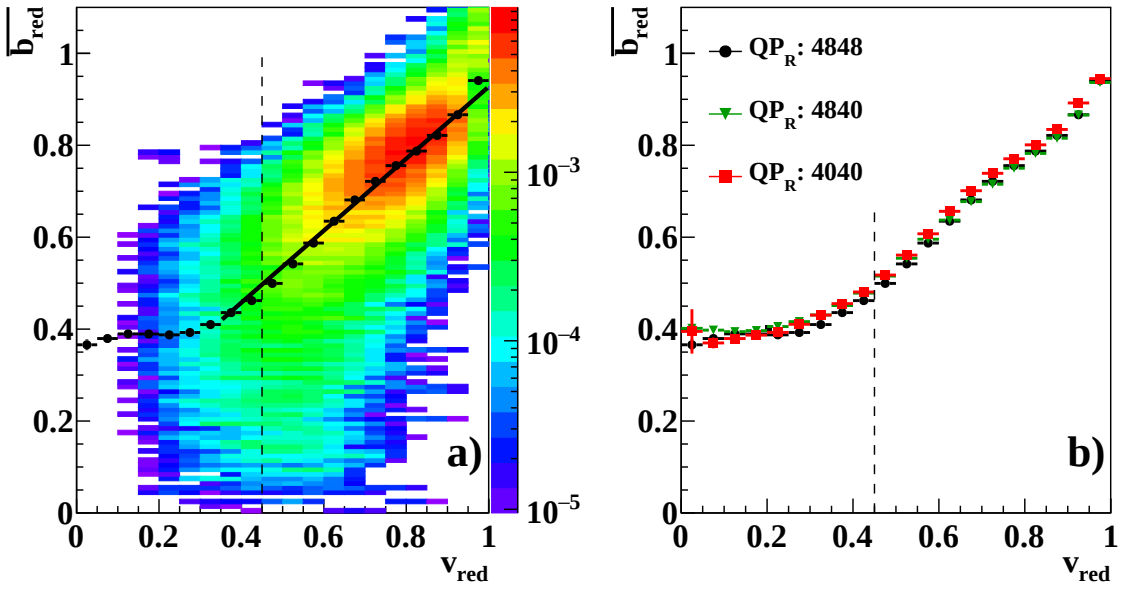

Figure 6.1: *(a) Correlation between the reduced impact parameter and the reduced velocity; distribution is normalized to unitary integral; black circles represent the average reduced impact parameter as function of v_{red}. (b) Average reduced impact parameter as a function of v_{red} for the three systems according to the legend.*

recent past, has been included in a wider theoretical context thanks to the development of models based on stochastic mean field or molecular dynamical approaches. Such kind of experimental and theoretical progresses are found for example in refs. [4, 9, 20]. Also in this thesis we want to investigate the n-p equilibration and for that we need to catalogue the events as a function of an estimator of the reduced impact parameter b_{red} (b/b_{gr}). For this purpose we can exploit as a guide the AMD simulation. Indeed, as observed in sec. 5.2 the simulation globally well reproduces the QP_R characteristics and, although with less accuracy, also the QP_B ones. Such evidences allow us to use the AMD prediction to obtain information on the reaction centrality.

Due to the limited angular coverage of the FAZIA-SYM setup, impact parameter estimators commonly adopted in large acceptance experiments, like the LCP transverse kinetic energy or multiplicity [1], cannot be safely used: they need in general the detection of most emitted species. In this work we choose as estimator of the reaction dissipation degree the parallel velocity of the QP, also exploiting the excellent energy information that we can extract from the FAZIA detector (cfr. sec. 3.4). With respect to ref. [62], where the author used the parallel velocity in the laboratory frame to sort the events as a function of their reaction centrality, we prefer to adopt the reduced velocity (v_{red}), defined in the following way:

$$v_{red} = \left(\frac{v_{par}^{QP}}{v^{beam}} \right)_{CM} \tag{6.1}$$

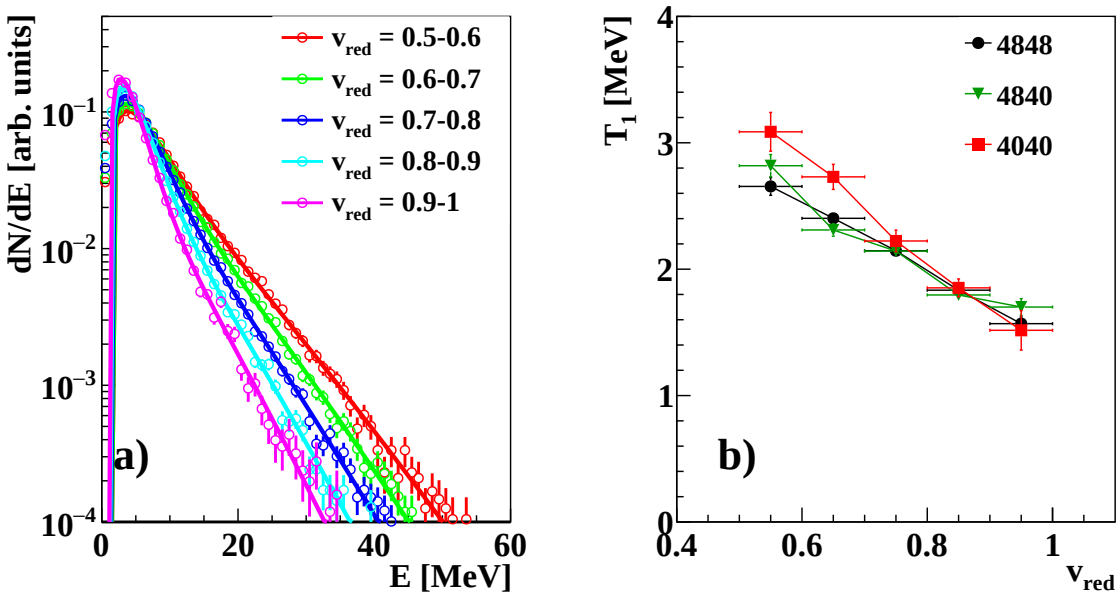

Figure 6.2: *(a) Proton kinetic energy distribution in the QP frame for the ^{48}Ca+^{48}Ca system. Distributions are divided in bins of reduced velocity. Each distribution is normalized to unitary area for a shape comparison. (b) Apparent temperature T_1 (see text for details) extracted from the Maxwellian fit of the proton kinetic energy distribution as a function of the reduced velocity; the results for the three systems are presented. Errors are statistical.*

i.e. the QP parallel velocity in the CM frame (v_{par}^{QP}) normalized to the beam velocity v_{cm}^{beam}, both in the system CM frame. In general, this normalized scale allows a more homogenous comparison of reactions with different entrance channels.

Fig. 6.1(a) shows the correlation between the reduced impact parameter b_{red} and v_{red}, obtained by the AMD simulation for the ^{48}Ca+^{48}Ca reaction. Black circles represent the average value of the reduced impact parameter ($\overline{b_{red}}$) as a function of v_{red}. Globally, according to the AMD simulation, the reduced velocity is well correlated with b_{red} in the range of $v_{red} \in [0.35, 1]$, where the average reduced impact parameter raises from $\overline{b_{red}}$ =0.42 up to $\overline{b_{red}}$ =0.92. For low values of v_{red} the correlation is lost. Very similar results are found for the three systems, confirming the goodness of our choice; in the fig. 6.1(b), we show the three average correlations, according to the legend. The vertical dashed lines marks the range of validity of the correlation that we further adopt for the following studies, therefore excluding the most central collisions.

Since the previous argument is of course based on the AMD predictions, we look for some other further confirmation of this correlation, directly on the experimental data in a model independent way. For such purpose we exploit the LCP detected in coincidence with the QP$_R$. Under the hypothesis of a large contribution from evaporative emission, LCP energy spectra contain information on the temperature of the emitting source. Thus, a variable which follows the reaction evolution as a function of b_{red} should select sources

with increasing temperature, moving from peripheral to more central reactions. The more central the collision, the hotter the source. For this reason, we exploit the LCP forward emitted with respect to the QP_R, as they more clearly reflect the statistical (i.e. secondary) decay of the excited QP after the primary interaction [2, 13, 21, 125].

Fig. 6.2 shows the proton kinetic energy distributions calculated with respect to the QP frame for the ^{48}Ca+^{48}Ca system. According to the legend, the distributions are presented in bin of reduced velocity. Each distribution is normalized to unitary area in order to evidence the differences in the shape at different reduced velocity bins.

We observe that each distribution presents two slopes. Before proceed some comments are in order. The QP frame is the good frame only for protons which contribute to the low energy tail[1], *i.e.* the thermal-part of the distributions [126]; the high energy tail could be due to different mechanism, such as pre-equilibrium emission from the neck [126] or from the deformed QP [127]. In particular, once we are dealing with pre-equilibrium emissions the QP frame could not be suitable. However, a two source fit can be used in order to disentangle the thermal part from the non-thermal one, thus obtaining information on the apparent temperature of the QP source. Indeed, the exact temperature of the excited QP cannot be easily measured: since several particles are emitted, the thermal part is affected by the sequence of cooling of the hot nucleus. We adopted a simple two source Maxwell-Boltzmann distribution [127]:

$$f = N_1 \frac{E - B_1}{T_1^2} e^{-\frac{E-B_1}{T_1}} + N_2 \frac{E - B_2}{T_2^2} e^{-\frac{E-B_2}{T_2}} \tag{6.2}$$

where N_i, B_i, T_i are the normalization factor, the Coulomb barrier and the temperature of the $i = 1, 2$ source, respectively. They are the free parameters of the fit. In particular, the temperature T_1 is the apparent temperature of the source [126], while T_2 is associated to the non-thermal part. The discussion of the T_2 term is out of the aim of this work. The fit results are superimposed in fig. 6.2(a) for each kinetic energy spectrum. For the aim of the present discussion we neglect the "pre-equilibrium" component. Moreover, the pre-equilibrium component predicted by the AMD model is small: this will be shown in the following of this thesis (cfr. sec. 6.5).

The trend of T_1 as a function of v_{red} is presented in fig. 6.2(b), for each investigated system according to the legend. Remarkably, an increase of T_1 as v_{red} decreases is evident, confirming the scaling of the reaction centrality with v_{red}.

In conclusion, these observations prove that the reduced velocity can be used as an estimator of the reaction centrality: indeed, even if the estimation of $\overline{b_{red}}$ from figs. 6.1(a,b) is model dependent, the T_1 scaling as a function of the reduced velocity points out that moving from v_{red}=1 to v_{red} ≈0.5 we progressively select more dissipative (central) collisions. It is worth mentioning that the error of both v_{red} and $\overline{b_{red}}$ is half of the bin width. However, for sake of clarity, except where otherwise stated, in the following plots we do not show it, preferring to connect the experimental points with a line, which guide the eyes. We also remind that error on the y-axis are statistical and smaller to the marker

[1] Recoil effects due to the emissions sequence are not taken into account.

size (ling width) if not visible.

6.2 Isospin equilibration in QP$_R$ channel

The n-p equilibration can be measured by means of the average neutron to proton ratio ($\langle N/Z \rangle$) of the various sources, studied as a function of the reduced velocity introduced in eq.(6.1). We start with the QP remnant, whose experimental results are shown in fig. 6.3. The top x-axis has been calibrated, between v_{red}=0.45 and v_{red}=1, according to the AMD prediction, in order to have an estimation of the average reaction centrality through b_{red}. The experimental data are presented for the three systems ^{48}Ca+^{48}Ca (full black dots), ^{48}Ca+^{40}Ca (full green triangles) and ^{40}Ca+^{40}Ca (full red square). In the following, except where otherwise specified, for the QP$_R$ event class the same symbols will be used. Lines are drawn to guide the eye.

Before discussing the isospin equilibration, we want to comment on the absolute values of $\langle N/Z \rangle$ for the two symmetric systems, remarking the fact that it is strongly impacted by the decay of the hot sources. According to Charity [128], the effect of the statistical evaporation on the final N and Z distributions of residues depends on the N and Z values of the hot nucleus and its excitation energy. In general, the higher the excitation, the closer the final cold residue arrives to the so called Evaporation Attractor Line (EAL). The EAL is the locus, in the $N-Z$ plane, corresponding to the final arrival of very hot nuclei whatever the starting point be. Remarkably, the EAL divides the $N-Z$ plane in two separated parts because this locus cannot be crossed, along any given decay chain. Thus n-rich nuclei approach the EAL from the n-rich side, n-poor nuclei from the n-poor side. For Ca ions, the EAL predicts $N/Z = 1.118$. Therefore, the projectiles of our Ca reactions stay on two different parts with respect to the EAL. We see in fig. 6.3 that indeed QP from ^{40}Ca stays below the EAL and tends to approach it when the centrality increases while the QP from ^{48}Ca shows a similar trend but from the top. The high neutron richness of the ^{48}Ca reflects in the much lower N/Z values, with respect to $N/Z = 1.4$ even for the less central collisions. To give an idea assuming only neutron emission from a primary excited population of ^{48}Ca ions, the first point (on the right of fig. 6.3) corresponds to the emission of 4 neutrons. Taking into account that the systems are symmetric, a part from the possible removing of mass and charge due to a fast pre-equilibrium stage, the initial population should anyway sit close to $Z = 20$ (cfr. sec. 6.5). In any case, for reference in the fig. 6.3 we plot also the EAL for $Z = 12$ which is the charge lower limit for the QP$_R$ selection.

Concerning isospin effects, at a first sight, we observe a hierarchy of the three systems, reflecting both the n-richness of the entrance channel and the isospin diffusion. Indeed, we see a clear gap, as expected, for the neutron content of QP residues in the two extreme cases of ^{40}Ca and ^{48}Ca. Moreover, the QP for the mixed system shows the occurrence of some isospin diffusion [24, 102] even for the most peripheral event class because its average neutron to proton ratio stays below that of the symmetric (n-rich) system where diffusion is not present. Interestingly, the gap between the n-rich and the mixed system

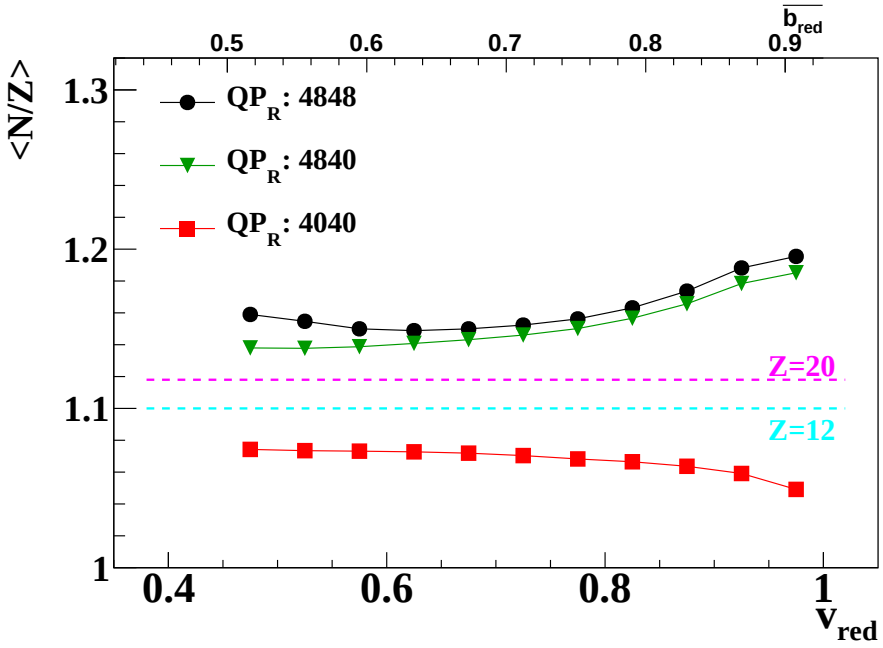

Figure 6.3: *Neutron to proton ratio as a function of the reduced velocity v_{red} for the three systems, according to the legend. The top x-axis has been approximatively calibrated in terms of reduced impact parameters according to the AMD simulations. The EAL [128] for $Z = 20$ and $Z = 12$ are drawn in magenta and cyan, respectively.*

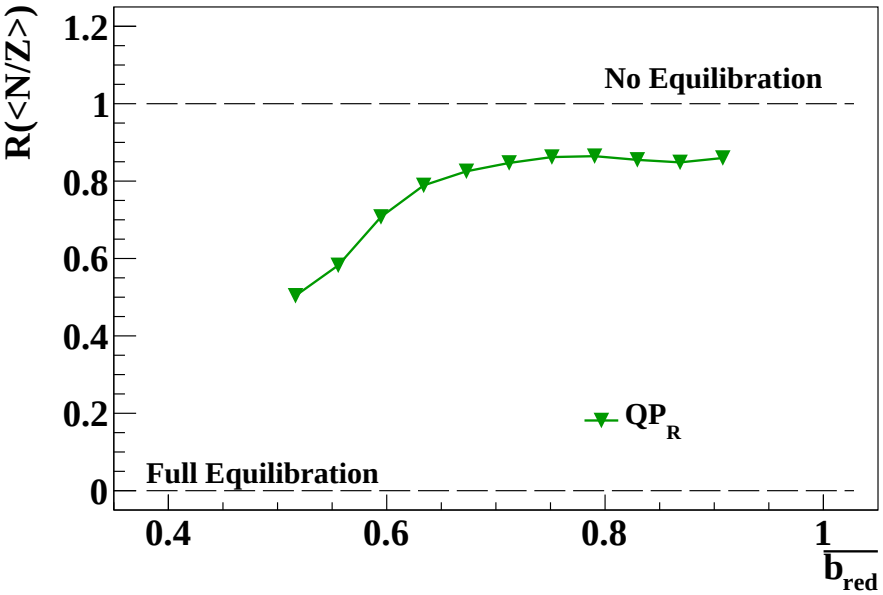

Figure 6.4: *Imbalance ratio of the average neutron to proton ratio of the QP_R as a function of $\overline{b_{red}}$. No Equilibration (+1) and Full Equilibration (0) levels are plotted as dashed lines.*

tends to slightly increase with reaction dissipation, suggesting an evolution towards the isospin equilibration.

In order to accurately evidence the isospin equilibration process we can exploit the imbalance ratio method (eq.(4.11)), introduced in sec. 4.3 of chap. 4. As a sensitive quantity for this equilibration we choose the average neutron to proton ratio of the QP$_R$ (see fig. 6.3), because it is a direct measurement of the fragment isospin. The imbalance ratio of $\langle N/Z \rangle$ as a function of the b_{red} is shown in fig. 6.4: the No Equilibration line (+1) and the Full Equilibration line (0) are underlined. We choose to adopt $\overline{b_{red}}$ and not the measured v_{red} for further better comparisons with the QP breakup channels and the INDRA+VAMOS results presented in the following.

As a consequence of the trend already noted in fig. 6.3, we first observe that the isospin diffusion acts already in the most peripheral reactions: indeed $R(\langle N/Z \rangle) = 0.9$ already in the first bin from the right. The damping process proceeds smoothly and weakly for less central collisions then a faster trend toward n-p equilibration is detected for $b_{red} < 0.7$ and we measure $R(\langle N/Z \rangle) = 0.54$ for the most violent analyzed collisions.

This experimental result is in agreement with the theoretical calculation on the mirror system ^{40}Ca+^{48}Ca at a lower bombarding energy of 25 MeV/u [23]. Here, Lombardo *et al.* performed a CoMD-II (Constrained Molecular Dynamics II) [129] calculation at $b = 7$ fm ($b_{red} \approx 0.7$), showing both the QP and QT isospin equilibration as a function of the primary interaction time. In particular the QT in this reaction correspond to our QP. At the separation time of 150 fm/c they found that the system has reached a valued of $R = 0.5$. However, as shown in the following sec. 6.4, our AMD simulation suggests, for our system at 35 MeV/u, a primary interaction time below 130 fm/c in the range of whole range of centrality, and in particular around 90 fm/c at $b = 7$ fm. For this interaction time, according to the CoMD-II calculation of ref. [23], the expected n-p equilibration is $R = 0.75$, closer to our value, also keeping in mind that the CoMD-II simulation refers to a bombarding energy of 25 MeV/u. However, our data test the process up to semi-central collisions because, as explained in sec. 6.1, the centrality selection towards head-on collisions would be unreliable. Therefore we cannot draw any conclusion on central reactions.

Before comparing our findings on the isospin diffusion with the predictions of the collision model AMD, we want to demonstrate the goodness and the robustness of the result. This is done in the following, first by reasonably changing some selection criteria applied to define our event sets and then with the important comparison with complementary experimental data measured on just the same reactions with the INDRA+VAMOS setup.

6.2.1 Test of the adopted QP$_R$ selection

As explained in sec. 5.1, the size limits to define what is a QP are rather arbitrary. Our decision identifies as a QP a BF with $Z \geq 12$, i.e. down to 60% of the QP. This choice is the same adopted by other authors [64, 111] but, for instance, Theriault [21] fixes a lower limit of 36%. In order to verify if the measured trend for the n-p equilibration could depend on the QP$_R$ definition, we test the result by changing the charge selection limits,

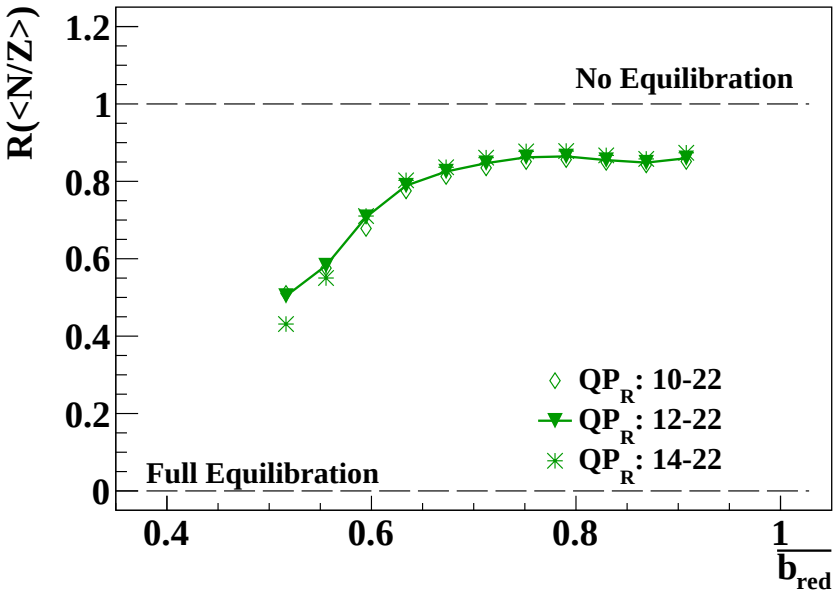

Figure 6.5: *Imbalance ratio of the average neutron to proton ratio of the QP_R as a function of $\overline{b_{red}}$, for the three different QP_R charge range definitions.*

expanding ($Z \geq 10$) or reducing ($Z \geq 14$) the considered sample.

We have verified that the $\langle N/Z \rangle$ *vs.* v_{red} plot is almost unaffected by these variations, in each system. As a consequence, also the imbalance ratio behaves quite the same, as demonstrated in the fig. 6.5. Only the point value at the lowest $b_{red} = 0.52$, for the $Z \in [14, 22]$ selection, is slightly lower than that of our default selection.

In conclusion, we can state that the imbalance ratio of $\langle N/Z \rangle$ of the QP_R is negligibly affected by the charge lower limit of the QP selection, thus in the following we will continue to adopt the standard selection of a QP_R, i.e. a BF with Z$\in [12, 22]$.

6.2.2 Comparison with the INDRA+VAMOS experiment

Now we want to compare the obtained results with those of the INDRA+VAMOS data [69]. For such purpose, thanks to the INDRA Collaboration, we had access to the fully identified and calibrated data set of the investigated Ca+Ca reactions on which we applied the same analysis as for the FAZIA data of this thesis. However, before comparing the n-p equilibration a comment is in order. During the INDRA+VAMOS campaign the main experimental trigger was the coincidence between the INDRA [31] and VAMOS [67, 68] detectors. Consequently the comparison is not straightforward, and some differences between the FAZIA and the INDRA+VAMOS data could be due to that.

Figs. 6.6(a) shows the $\langle N/Z \rangle$ as a function of the LCP transverse kinetic energy normalized to the total available energy in the CM ($E^{cm}_{trans}/E^{cm}_{TOT}$). We notice that, differently from v_{red}, the $E^{cm}_{trans}/E^{cm}_{TOT}$ ratio orders the points from left (peripheral collisions)

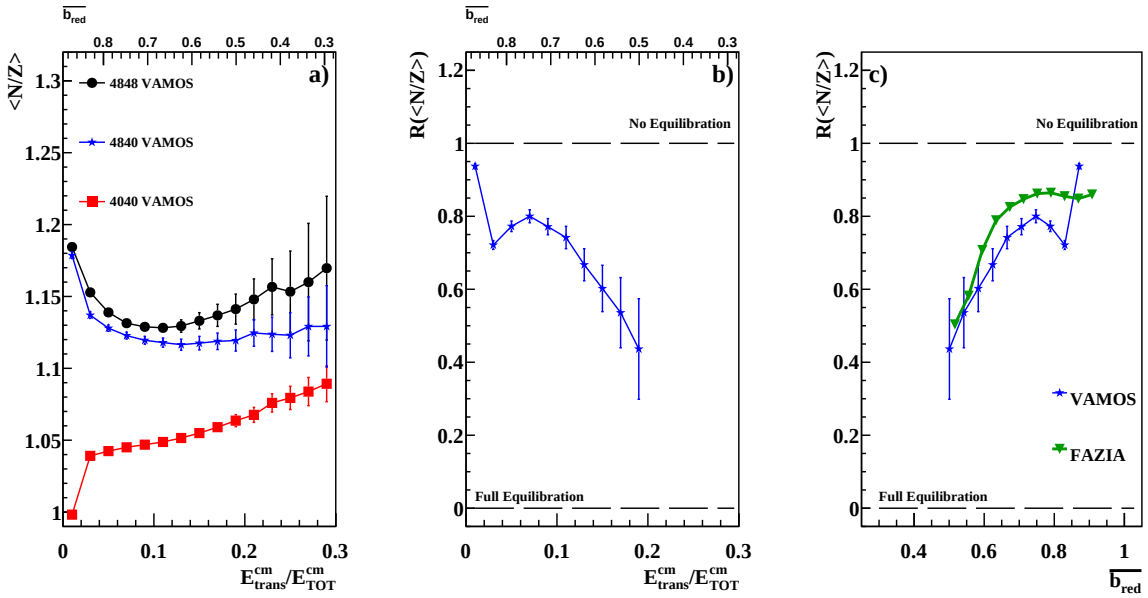

Figure 6.6: *INDRA+VAMOS data on Ca reactions. a) Neutron to proton ratio as a function of the normalized LCP transverse kinetic energy. b) Imbalance ratio of the neutron to proton ratio as a function of the normalized LCP transverse kinetic energy. c) Comparison between the FAZIA and VAMOS n-p equilibration.*

to right (central collisions). The average reduced impact parameter estimation, extracted by means of the AMD simulation[2], is shown in the top x-axis. We choose to adopt a different centrality estimator because the large acceptance of the INDRA multi-detector allows the employ of the LCP transverse kinetic energy which is sensitive also to more central reactions with respect to v_{red}. $E^{cm}_{trans}/E^{cm}_{TOT}$ was demonstrated to be a good variable for event selection and largely adopted also by the same INDRA group in different systems at comparable bombarding energies [2, 130] .

From fig. 6.6(a) we see a trend very similar to our results (see fig. 6.3) for the three systems in the region in which the comparison with FAZIA can be performed (right-hand side with respect to the dashed line). The INDRA+VAMOS data extend up to more central collisions, as expected thanks to the large acceptance of the setup. We note that the VAMOS values of $\langle N/Z \rangle$ are systematically lower than the ones extracted from FAZIA. However, as anticipated, we are comparing data with different main trigger and angular coverage with very different experimental apparatus, thus the discrepancies in the absolute value of $\langle N/Z \rangle$ could be related to different main trigger conditions.

A more straightforward comparison can be done by means of the imbalance ratio: fig. 6.6(b) shows the VAMOS results alone, while in fig. 6.6(c) they are directly compared with our data using the common order parameter $\overline{b_{red}}$. The points at $\overline{b_{red}}$<0.5 have been discarded due to the huge fluctuations probably caused by too low statistics. Overall, we observe a very similar trend: the more the reaction centrality, the more equilibrated the

[2]With a procedure identical to the one adopted in sec. 6.1

isospin of the QP.

However we can note some differences. First, the VAMOS data show a greater degree of equilibration than the FAZIA-SYM results for a given $\overline{b_{red}}$ bin. Such discrepancy could be due to the different event classes selected by the INDRA+VAMOS setup geometry and main trigger condition with respect to FAZIA-SYM. Indeed, the request of at least one particle (or fragment) in INDRA and the complete lack of QP+LCP coincidences at the forward angles can result in somewhat different isotopic distributions. Second, in the very peripheral events of the VAMOS data, a less regular trend is found: this could be due to a finite number effect, as the LCP multiplicity for this very peripheral events is very small ($M_{LCP} = 1 - 2$). As described in literature [1], this could be cause of large fluctuations on the LCP transverse kinetic energy.

From our point of view the comparison is satisfactory. We underline that two independent experiments on the same reactions but with two completely different analyses indicate a quite similar isospin equilibration trend.

6.3 Model predictions about the isospin equilibration

The obtained exclusive data can be compared with the AMD(+GEMINI) transport model results in order to verify the reliability of the general description of the microscopic reaction mechanisms and, more specifically, to test some important parameters that rule the nuclear dynamics and the nEoS far from equilibrium. Indeed, in sec. 5.2 we have seen that the molecular dynamics approach of AMD fairly well reproduces the gross properties of the reaction in both the QP_R and QP_B channels. Now we want to check if the simulation is able to reproduce the details of the reactions, namely the isotopic composition of the QP and the experimentally observed equilibration. We repeat here that this is a challenging effort because the decay from the hot sources strongly affects the final composition of the detected (secondary) ions, thus reducing the sensitivity of the measurements to the initial (primary) interaction effects (cfr. sec. 4.3). Notwithstanding this limitation, the precise event-per-event access to the isotopic composition of (all) the ejectiles is deemed to be an useful tool for this physics [6].

As described in chap. 4, the used Monte Carlo simulation implements a two-step code describing via AMD the dynamical phase up to 500 fm/c and then via GEMINI++ the pure statistical decay calculated for all species which are recognized in each event as excited above the particle emission threshold. We should here remind (cfr. sec. 4.3) that part of the evaporation is also performed in the AMD code because the true interaction time, depending on the impact parameter, approximately ends within 130 fm/c (see sec. 6.4), well before 500 fm/c.

In any case, for a proper comparison the same experimental cuts (cfr. chap. 4) and selections have been applied to the simulated data (cfr. sec. 5.1). In particular the estimation of $\overline{b_{red}}$ following the procedures described in sec. 6.1 is adopted.

Fig 6.7 shows the model predictions for the $\langle N/Z \rangle$ *vs.* v_{red}, also compared with the experimental data. Panel a) with the asy-stiff recipe (dashed lines), panel b) with the

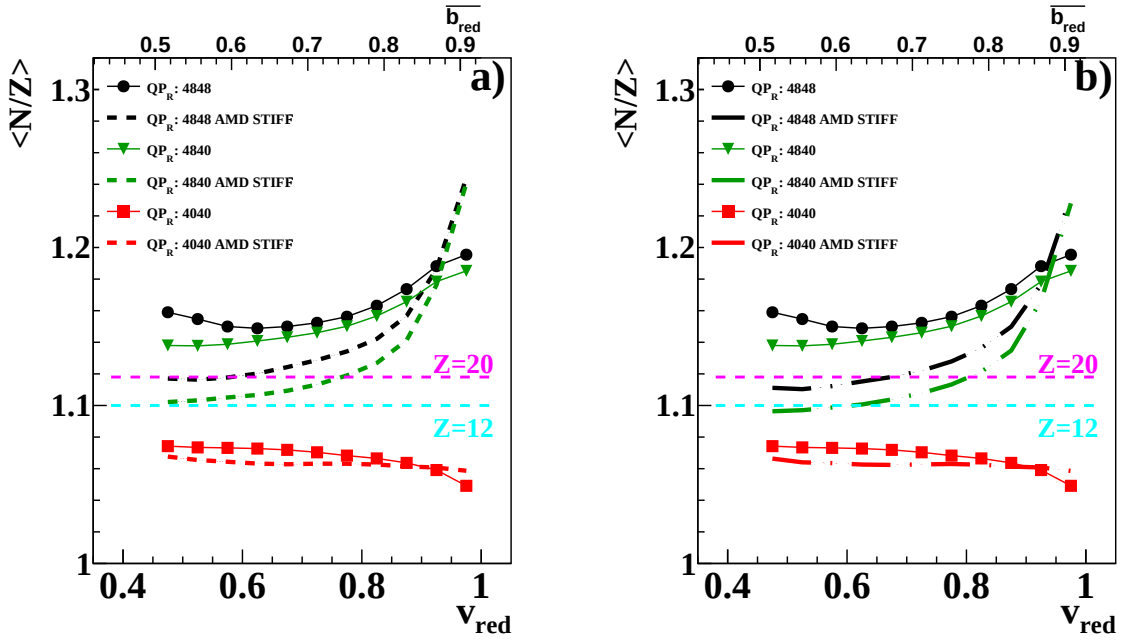

Figure 6.7: *Experimental and simulated, with the AMD asy-stiff (panel a) and asy-soft (panel b) recipe, neutron to proton ratio as a function of the reduced velocity v_{red} for the three systems, according to the legend. The EAL [128] for $Z = 20$ and $Z = 12$ are depicted with magenta and cyan dashed lines, respectively.*

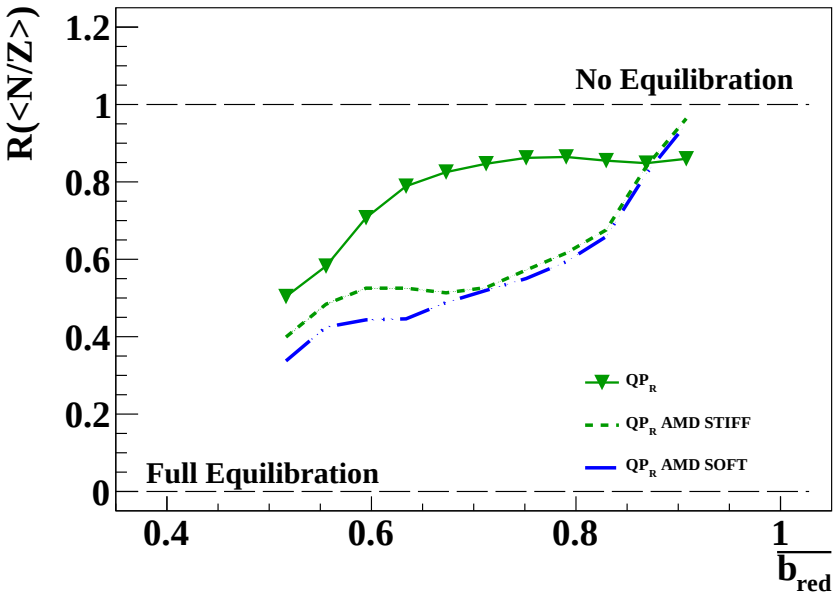

Figure 6.8: *Experimental and simulated imbalance ratio of the average neutron to proton ratio for the QP_R channel.*

asy-soft one (dot-dashed lines). For sake of clarity, for the three reactions the same colors as the experimental points are adopted. Overall we can see that, as expected, the model predicts some isospin diffusion because the same hierarchy of the data is found in all cases. Moreover, the agreement is quite nice for the ^{40}Ca system while the model fails in reproducing the $\langle N/Z \rangle$ trends observed for the ^{48}Ca QPs. In particular, the AMD simulation gives a too fast approach of the n-rich ^{48}Ca QPs to the EAL values [128], in any case a too rapid decrease of the neutron content with centrality. Also a larger gap in $\langle N/Z \rangle$ is predicted between the n-rich and the mixed systems for all v_{red} bins except for the less central ones where the simulated data cross the experimental points. No significant differences can be appreciated changing the recipe of the symmetry energy: as also pointed out in sec. 4.3, the asy-soft parametrization tends to more decrease the neutron content with respect to the asy-stiff one.

The results of fig. 6.7 immediately suggest that an important discrepancy is obtained at the level of the imbalance ratio for $\langle N/Z \rangle$. Indeed, fig 6.8 displays the results for this variable for the considered QP_R class, again compared with the experimental findings (already in fig. 6.4). The curves for the two asy-stiffness choices are represented, in blue the asy-soft in green the asy-stiff. The figure shows that the model predicts a too smooth and fast trend towards isospin equilibrium with respect to measured data.

The discrepancies between the model and the experimental data suggest the following observations. First, as also anticipated in sec. 4.3, the similarity between the asy-stiff and asy-soft recipes indicates that, within our model calculations, the system does not significantly explore sub-saturation regions where larger effects due to the different symmetry energy recipes are expected (see fig. 4.1). A second comment can be on the E_{sym}. This term of the symmetry energy affects the n-p exchanges during the interaction and consequently represents the restoring potential for the isospin (cfr. sec. 1.2.1). One possible interpretation of the too rapid motion towards equilibrium could be that in the model E_{sym} remains at too high values than in the reality, and this can happen if the system remains too close to the saturation density.

In order to investigate the density region explored by AMD during the collision, we went back within the calculation at 60 fm/c (see sec. 6.4 for the time backtracing procedure) and looked at the normalized density (ρ/ρ_0) distribution in the equatorial plane. Results are shown in fig. 6.9, for an event at $b_{red}\approx 0.8$ of the ^{48}Ca+^{48}Ca system. Loci at $z > 0$ fm refers to the QP and $z < 0$ fm to the QT phase-space. We can clearly see that both central regions are at saturation ($\rho/\rho_0 = 1$) or supra-saturation ($\rho/\rho_0 > 1$) and then the density smoothly decreases following the Fermi function profile towards the nucleus edges. The protrusion on the side is an α particle which is already emitted from the system. Rather interesting, even if the density profile along the neck reaches sub-saturation values ($\rho/\rho_0 \approx 0.6$ at $(z, x) = (0, 0)$ fm), the zones in which this happens represent only a fraction of the whole system. Similar distributions have been obtained selecting events at comparable b_{red} and time. Consequently, in the model, too high values of E_{sym} are experienced than in the reality, thus leading to a faster equilibration. Of course, also interaction times play a role because, for a given restoring potential, the duration of the contact favors the path to equilibrium. We will come to this point in the following (sec. 6.4).

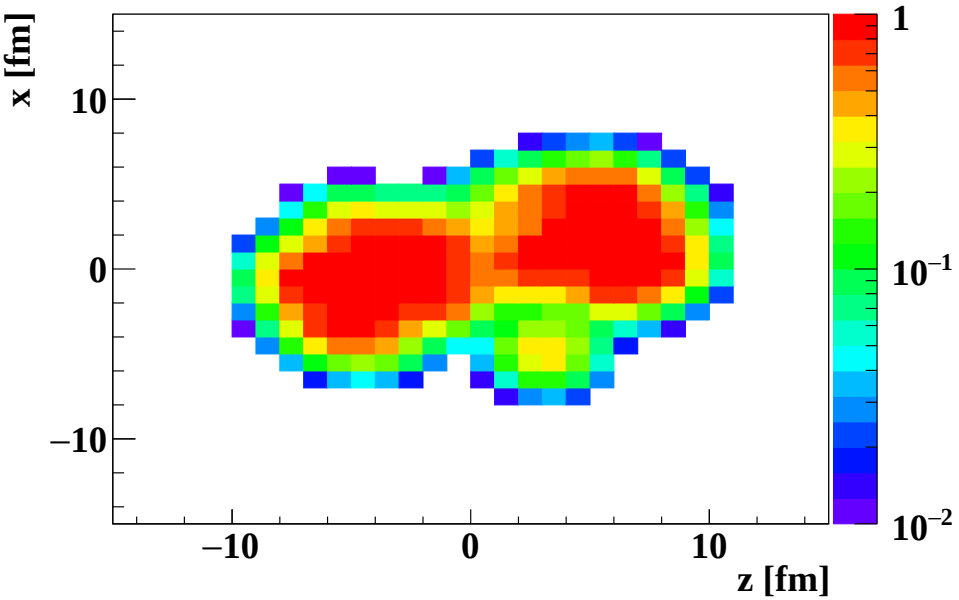

Figure 6.9: *Density plot in the equatorial plane ($y = 0$) for the ^{48}Ca+^{48}Ca system at 60 fm/c. The protrusion on the side is an α particle which is already emitted from the system. Values are normalized to the saturation density. z is the bream direction.*

In conclusion, the used transport model, as expected, predicts that the isospin diffusion is present in the ^{48}Ca+^{40}Ca reaction driving the QP neutron to proton ratio towards lower values due to the presence of an isospin gradient between projectile and target. The model fails to explain the details of the n-p composition of the fragments, and it gives a too rapid trend towards equilibrium than measured. Moreover, almost no sensitivity is found as for the asy-stiffness recipe of the nEoS. Such observations are compatible with the development, within the model, of only small neck regions at sub-saturation density during the interactions. Moreover, as a support of this argument we can take fig. 2 of ref. [6]. Here, for a heavier Ni+Ni systems, at a slightly higher bombarding energy (40 MeV/u), stochastic mean field calculations predicts a neck occurrence in less than 20% of the events in the range $b_{red} = 0.4 - 0.7$. In the same direction points a naive calculation of the overlapping region for various b_{red}. In the ^{48}Ca+^{48}Ca case, the overlapping of two spherical nuclei at $b_{red} = 0.8$ contains only 4 nucleons while this number increases to 8 at $b_{red} = 0.7$. At lower b_{red} the neck probability formation and/or the neck size increases, and then a stronger equilibration is obtained.

6.4 Equilibration in breakup channels

We now move to the second goal of the FAZIA-SYM experiment. Indeed, for the first time we can study the isospin dynamics in the breakup channel and compare its behavior

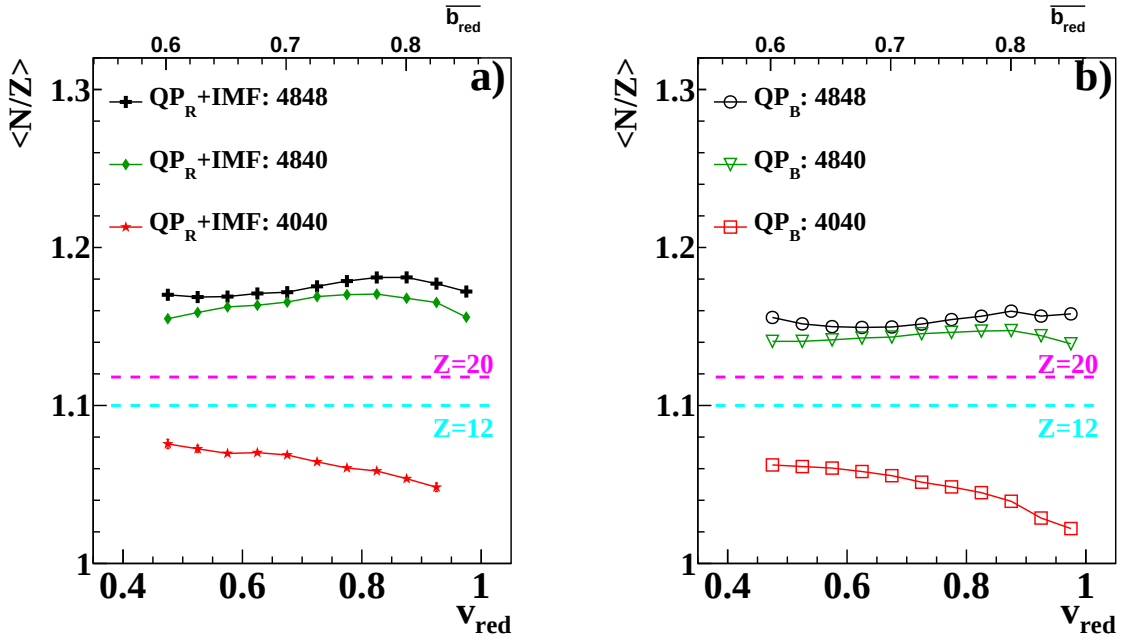

Figure 6.10: *Average neutron to proton ratio for the QP_R+IMF (panel a) and QP_B (panel b) channel as a function of the reduced velocity v_{red} for the three systems, according to the legend. $\overline{b_{red}}$ estimation on the top x-axis. The EAL [128] for $Z = 20$ and $Z = 12$ are pointed out with magenta and cyan dashed lines, respectively.*

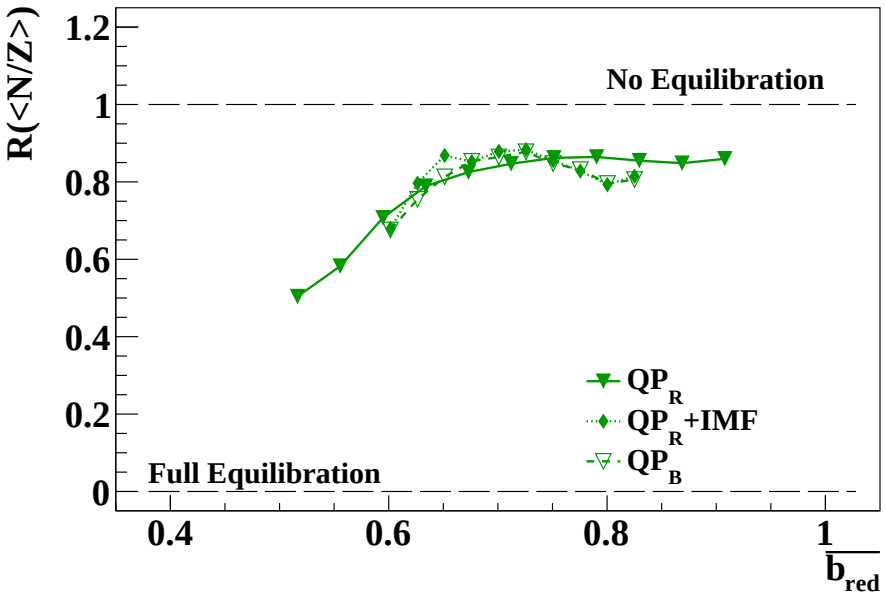

Figure 6.11: *Imbalance ratio of the average neutron to proton ratio of the QP_R, QP_R+IMF and QP_B channels as of $\overline{b_{red}}$. No Equilibration (+1) and Full Equilibration (0) levels are underlined.*

with the QP_R channel. The comparison is also extended to the QP_R+IMF channel, since, as anticipated in sec. 5.2.2, it can be assumed as a very asymmetric breakup of the QP: indeed the charge asymmetry for this kind of splits extends to values up to $\eta = 0.7$ while the maximum η for our selection of QP_B is about 0.5 (cfr. sec. 5.2.3).

Fig. 6.10(a,b) shows the average neutron to proton ratio of the reconstructed QP (from the two fragments) as a function of the v_{red}; v_{red} has been calculated from eq.(6.1), exploiting the velocity of the splitting QP (i.e. the CM velocity of the two detected fragments). Full crosses, diamonds and stars refer to the QP_R+IMF channel, while open circles, triangles, squares to the QP_B selection. Colors are used according to the convention previously introduced. In the following, except where otherwise specified, for the QP_R event class the same symbols will be used.

The corresponding estimation of $\overline{b_{red}}$ is shown in the x-axis on top. It is extracted following the same procedure described in sec. 6.1. We mention that, while if in the QP_R channel we could explore from $\overline{b_{red}} \approx 0.5$ to $\overline{b_{red}} \approx 0.9$, here we are investigating events in a more limited impact parameter range, i.e. $\overline{b_{red}} \in [0.6, 0.84]$. In particular, the most peripheral reactions are not accessible, and this is reasonable considering that those require a certain amount of dissipation.

First of all, comparing the absolute values, the reconstructed QP in the QP_R+IMF channel are more n-rich that those in the QP_B channel, which are instead fully comparable with the QP_R event class values (see fig. 6.3). This is related to the fact that IMFs have larger neutron to proton ratio with respect to heavier fragments [24, 102], and the reconstruction of a QP with this fragments reflects such characteristics ($\langle \frac{N}{Z} \rangle_{IMF} \approx 1.3$ while $\langle \frac{N}{Z} \rangle_{BF} \approx 1.1$). A detailed analysis of the neutron content of the event classes will be presented in the following (cfr. sec. 6.5).

Concerning the n-p equilibration, we observe that the hierarchy found for the three reactions in the QP_R event class is maintained in both classes, suggesting the presence of isospin diffusion. It can be better appreciated by means of the imbalance ratio method, and compared with the QP_R selection. Results are reported in fig. 6.11 with full green diamonds (QP_R+IMF) and open green triangles (QP_B): for sake of comparison also the results of fig. 6.4 are shown.

The results for the three classes are very similar, signaling that a common process of n-p equilibration acts whatever the channel type, in the explored range of centrality. This last observation suggests that both breakups occur after the end of the primary interaction of projectile and target, or in any case after the end of the processes that act to restore the neutron-proton balance between the projectile and target.

Unfortunately, the accumulated statistics of simulated events is not enough to apply the same analysis of imbalance ratio *vs.* impact parameter for the QP_R+IMF and QP_Bselection which represent, each, less than percent of the evaporative channel. The very similar experimental behavior of the n-p equilibration for the three channel can be connected to a similar interaction time. We searched for a support for this reasonable hypothesis using AMD calculations, although being aware that, as discussed before, the exact timescale of the process could be not fine.

The procedure to extract information on the relevant times (especially the interaction

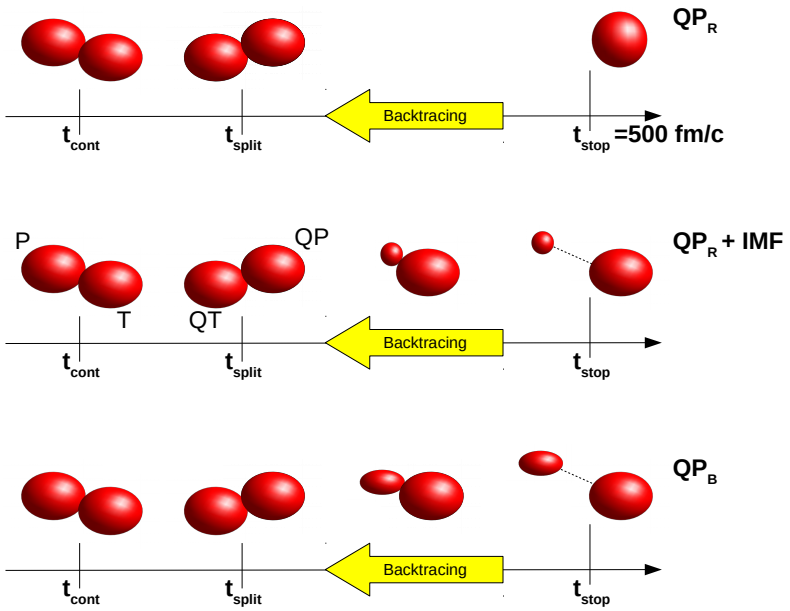

Figure 6.12: *Schematic representation of the backtracing procedure employed to estimate the time at which the primary interaction ends (t_{split}). Primary interaction starts when projectile (P) and target (T) collide (t_{cont}). The interaction time is defined as $t_{int} = t_{split} - t_{cont}$.*

time t_{int}) in AMD is that proposed in ref. [98] and it is briefly explained here. In a typical run of AMD the fragment recognition algorithm is applied every 10 fm/c in the range 20−200 fm/c and then at 20 fm/c time step up to 500 fm/c; two wave packets are taken as belonging to the same fragment if the distance between their centers is within 5 fm. For each events class, we imposed our selection criteria at 500 fm/c: this permits to identify QP_R, QP_R+IMF and QP_B channels. A specific backtracing routine (schematized in fig. 6.12) can be used for all event types, going back in time until a unique fragment with a charge comparable with the interacting projectile+target system is found, thus defining the split time t_{split}. For better accuracy and consistency, in the case of the QP_R+IMF and QP_B channels, before reaching t_{split}, we require the formation of a unique fragment, forward emitted in the CM frame and with size larger than that of reconstructed ion at 500 fm/c.

The obtained results for the three indicated QP decay channels are shown in fig. 6.13 for the ^{48}Ca+^{40}Ca reaction; the figure shows the average interaction time $\langle t_{int} \rangle$ is plotted as a function of the reduced impact parameter b_{red}, where t_{int} is defined by subracting from t_{split} the time when the collision starts in the model. As expected, we observe that the split time increases as the centrality increases. Rather interesting, the obtained values result quite similar varying the event classes with differences below 10÷15 fm/c. Such finding supports our hypothesis is reasonable, i.e. an essentially equal interaction time.

In conclusion the similarity of the imbalance ratio dependence on $\overline{b_{red}}$ in the three QP channel types can be explained, with the support of molecular dynamics calculations, by essentially comparable interaction times between projectile and target resulting in a

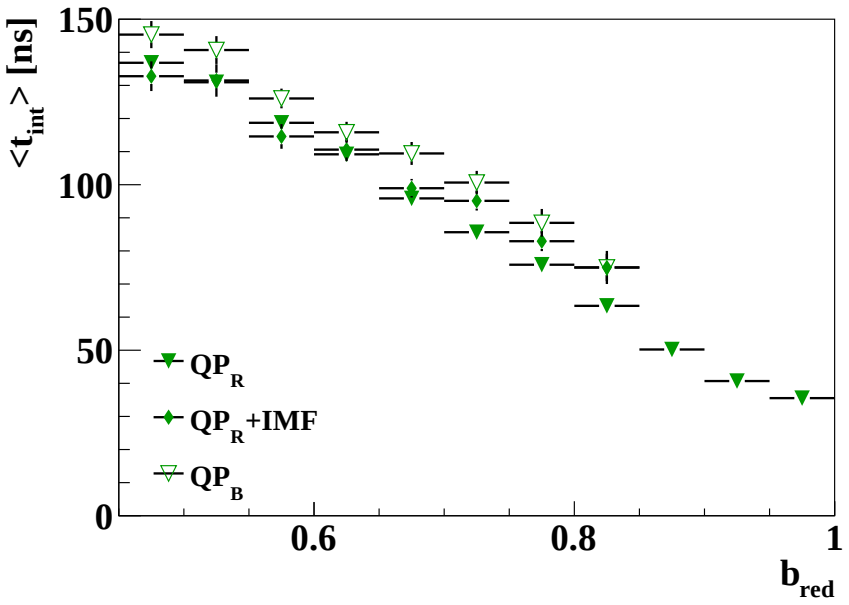

Figure 6.13: *Correlation between the projectile-target interaction time t_{int} and the reduced impact parameter. Data refer to $^{48}Ca+^{40}Ca$ AMD simulated events. Symbols of each channel according to the legend.*

similar level of isospin balance only scaling with the impact parameter.

6.5 Dynamical effects in symmetric collisions

According to the scientific goal of the FAZIA-SYM experiment (cfr. sec. 3.1), we now move to investigate the possible role of dynamical effects in the n-p exchange processes. With this we mean in particular (cfr. sec. 1.2.1) the possibility that in collisions at Fermi energies the excitation energy dissipation is so fast that in the contact region a kind of "fireball" develops. The dinuclear system evolves and expands during the separation phase, also reaching some dilute configuration (for instance predicted by the AMD model in fig. 6.9). At this point an isospin drift process can occur as predicted by theoretical models [3, 4], and suggested by recent experimental observations [14, 25]. The drift is due to the formation of a density gradient between the diluted neck and the neighboring regions (at saturation or supra-saturation). As a matter of fact, since about two decades, experiments have accumulated a rich confirmation that clustered species emitted from the phase-space region in semi-peripheral collisions at Fermi energies are neutron abundant more than when emitted from other sources [13, 21–24, 64, 118]. The search of neutron rich fragments from the neck is particularly well motivated in symmetric systems where the concurrent isospin diffusion is absent[14, 21, 22, 25]. Therefore we concentrate on our symmetric reactions neglecting the mixed system $^{48}Ca+^{40}Ca$.

We would underline that the occurrence of isospin drift in the ^{48}Ca+^{40}Ca system should not appreciably affect the interpretation on the isospin diffusion discussed before. Indeed, thanks to the imbalance ratio, all the effects in common to the three measured systems, including the possible isospin drift, are bypassed [8] and only peculiar characteristics of the mixed system survives.

We notice an important point of this work: we can explore not only the isotopic properties of the light clusters emitted at mid-velocity but even correlate them with the isotopic distributions of the coincident heavier QP remnants. In this investigation we are well aware that detected fragments are typically the remnants formed by the decay of hot parent nuclei. In case of statistical emission, light fragments (as the IMF) are produced as (almost) cold species while heavier ones (i.e. QP remnants or QP breakup fragments) can come from long evaporative chains. On the other hand, IMF formed from a mid-velocity region, before referred qualitatively as "fireball", are probably formed in a hot environment and thus populated as resonances or unbound exotic states. Thus, in this case, the detected neck fragments (eg. Li, Be, B isotopes) might be associated with emitted nucleons which, we argue, are essentially loosely bound neutrons because protons are necessary to form the observed species.

We start to investigate the channel with the production of an IMF because for this the literature reports the largest effects attributable to isospin drift [3, 13, 21–23]. This is easily and obvioulsly motivated by the big effect of adding only one more neutron to a small IMF. For example, ^{6}Li has $N/Z = 1$. As soon as some neutron is included to form n-richer isotopes we can dramatically shift the average N/Z by including ^{7,8,9}Li having $N/Z = 1.33$, 1.67 and 2. Conversely, the variation of one neutron on a ion of mass similar, for example, to that of Ca, generates a variation in N/Z of 0.05.

We try to evidence differences in the IMF isotopic composition using the commonly adopted angular variable α (see ref. [14, 25] also previously introduced in sec. 5.2.2). The idea, and the evidence, is that fragments forward emitted with respect the QP$_R$ are more compatible with a statistical emission from a hot source; instead, fragments backward emitted are more linked with the dynamics of the reaction [64].

We have not enough statistics to densely populate α angle bins as done in other works [14, 25]; also we already discussed on the scarce efficiency for transverse emissions due to the geometric acceptance. Therefore we prefer to define two distinct gross regions: the first when a fragment is backward emitted (BWD, of course with respect to the QP velocity), selected with $\alpha < 70°$, and the second when it is forward emitted (FWD, $\alpha > 110°$). For both configurations, thanks to the FAZIA isotopic resolution, we can access on an event basis to the neutron to proton ratio of both ejectiles and look at the possible correlations.

In particular, an anti-correlation of their neutron contents has been observed [14, 25] for fragment pairs originated by QP breakup. The very interesting results, however, are presented without any link with the impact parameter and this is just we want to attempt now. The study of the evolution of these phenomena *vs.* the impact parameter has been performed in the past but the examples are rather scarce to our knowledge [21–23]. To this aim we order our event sets as a function of the $\overline{b_{red}}$ variable (sec. 6.1) and

a first result is presented in fig. 6.14(a,b). There, we show the $\langle N/Z \rangle$ values of the IMF (blue crosses) and the companion QP_R (red crosses) as a function of $\overline{b_{red}}$, for both the ^{48}Ca+^{48}Ca and ^{40}Ca+^{40}Ca systems in panel a) and b), respectively. Open symbols refer to the BWD configuration, while full symbols to the FWD one. In both panels we also report, with full black dots, the $\langle N/Z \rangle$ values of QP remnants when no IMF are detected in coincidence ("QP_R alone" in the following). The QP_R alone case is a kind of reference for us because we guess it represents the gross average configuration for each $\overline{b_{red}}$. Please, note that the y-scales are the same in the two panels, thus evidencing the effect of the different neutron richness in the two cases.

We start to comment the ^{48}Ca+^{48}Ca system (fig. 6.14(a)). First we observe that the $\langle N/Z \rangle$ of the IMF is larger (around 1.30) than for QPR; as said before, this is a obvious consequence of a population of light species (here $Z = 3, 4$ are considered) when forming them in whatever environment having some neutrons available and thus also independently on their dynamical or statistical origin [102]. The more important finding is that BWD IMF have a greater neutron to proton ratio ($\langle N/Z \rangle \approx 1.32$) with respect to the FWD one ($\langle N/Z \rangle \approx 1.28$). This splitting is just the effect commonly reported in literature [14, 25] and, as said, compatible with an isospin drift [3, 4] scenario. Also we notice that the observed N/Z values are consistent with those in the literature which refer to heavier systems having a larger neutron reservoir. For instance, our FWD and BWD values are quite similar to the corresponding $Z = 3, 4$ fragments reported for ^{84}Kr+^{112}Sn by Barlini [24] or for ^{112}Sn+^{58}Ni by DeFilippo [102]. Instead, they are clearly higher than for n-deficient systems (*e.g.* ^{64}Zn+^{64}Zn [131] or ^{58}Ni+^{12}C [132]).

Concerning the QP_R we can do two comments. First we note a slight decrease with increasing centrality, common to both the QP_R alone and to the QP_R partner of the IMF, in the comparable range $\overline{b_{red}} < 0.8$. Interestingly, this latter event type (QP_R+IMF) produces final QP fragments with a slightly lower N/Z. According to refs. [14, 21, 22, 25], the N/Z values should be somewhat anti-correlated with that of the corresponding IMF, if originated by the same initial nucleus. This characteristics is not clearly present here, and the QP_R assume equal N/Z values, within the error bars, as shown in the zoomed sub-panel of fig. 6.14(a).

Similar features are also visible in the ^{40}Ca+^{40}Ca system presented in fig. 6.14(b), although the scarce availability of neutrons strongly shrinks the values in a reduced N/Z range. Rather interesting, we observe an increase with the centrality of the neutron content of IMFs BWD emitted. By inspecting the zoomed panel for the N/Z of the QP remnants one sees, perhaps, a weak indication of isotopic anti-correlation in particular at $\overline{b_{red}} < 0.75$, i.e. when a clear split between the $\langle N/Z \rangle$ of the BWD and FWD emitted IMF appears. We checked that the very small effect on the QP_R $\langle N/Z \rangle$ is comparable with that extracted from ref. [25], taking into account of the different kind of data presentation and of the fact that we are now grouping several α angle bins in only two rough regions. As for ^{48}Ca, also for ^{40}Ca we see that the emission of an IMF produces slightly more symmetric heavier fragments that can be qualitatively consistent with the fact that the IMF emission requires neutrons that are picked up from both (equal) colliding nuclei.

The previous findings again speak in favor of some dynamic effects in the production

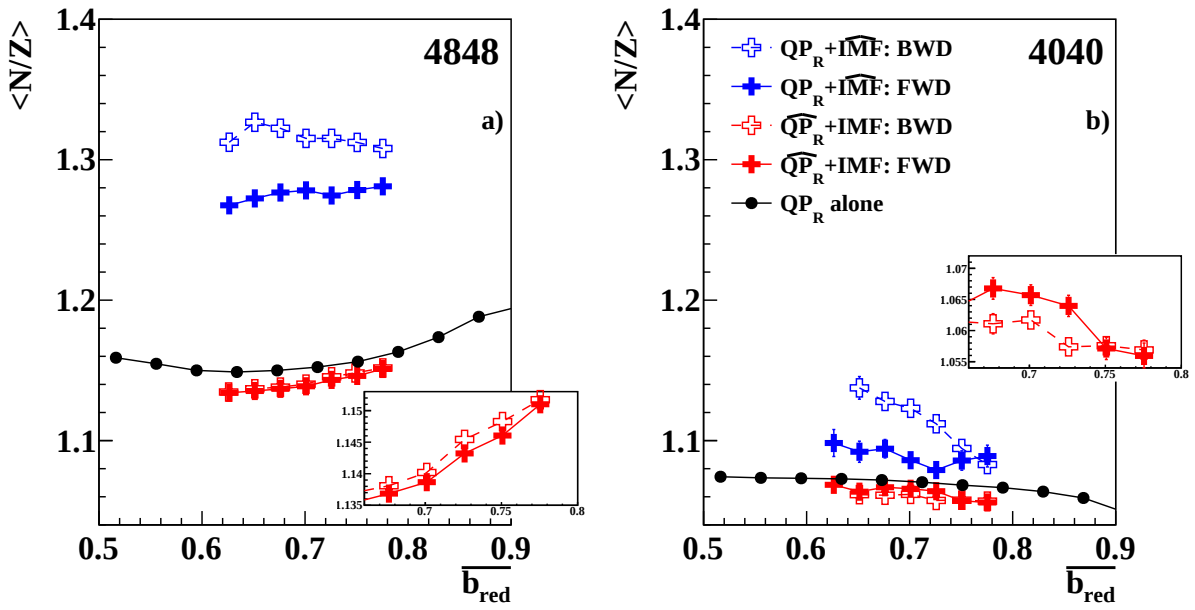

Figure 6.14: *Neutron to proton ratio as a function of $\overline{b_{red}}$ for both the QP_R and IMF in the QP_R+IMF channel, separating the IMF backward (BWD) and forward (FWD) emission (see text). Symbols according to the legend: the "hat" labels fragment type whose $\langle N/Z \rangle$ value is shown. Black full dots show the QP_R alone, i.e. without IMF in coincidence. Panel a) ^{48}Ca+^{48}Ca, Panel b) ^{40}Ca+^{40}Ca reaction. Sub-panels show a zoom on the QP_R values.*

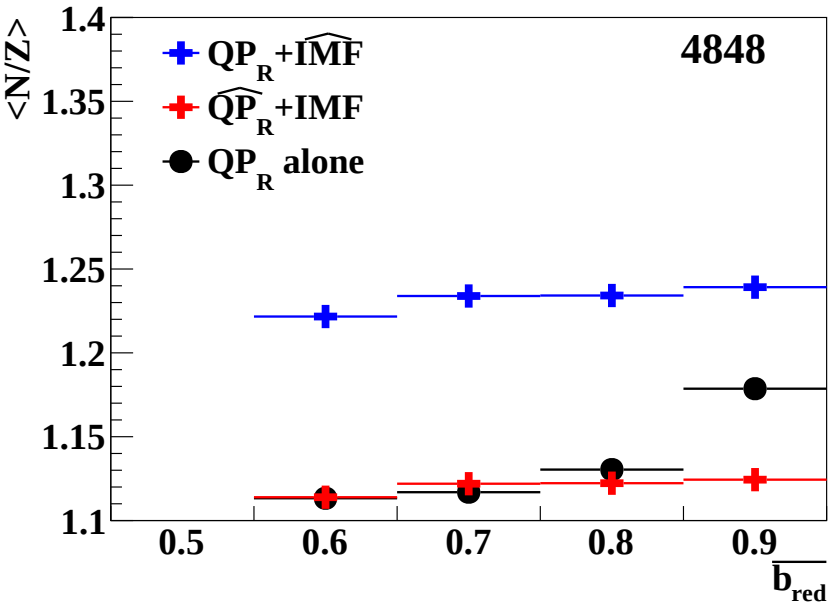

Figure 6.15: *Neutron to proton ratio obtained by the GEMINI++ simulations according to the input of tab. 6.1 (see text) and reported in the same kind of order as fig. 6.14 for an easier comparison.*

Table 6.1: *Average atomic number, neutron number, excitation energy of the QP produced at the split time for both QP_R alone and QP_R+IMF channels selected at 500 fm/c. Values refer to the $^{48}Ca+^{48}Ca$ system.*

	QP_R alone			QP_R+IMF		
$\mathbf{b_{red}}$	**Z**	**N**	$\mathbf{E^*}$ [MeV]	**Z**	**N**	$\mathbf{E^*}$ [MeV]
0.9	20	28	75	22	30	210
0.8	20	28	140	22	30	230
0.7	20	27	170	21	29	260
0.6	20	27	220	21	28	260

of IMF which, however, are rather weak due to the small size of the nuclei. We remind that, to our knowledge, this is the symmetric reaction set with the lightest participating nuclei ever investigated in this context. A naive calculation can give an idea. Indeed, if we calculate the overlapping volume of two Ca-ions (taken as spheres with constant density according to simple liquid drop basis) at various impact parameters we find that in our $\overline{b_{red}}$ range it contains from 4 (3) nucleons at b_{red}=0.8 to 13 (11) nucleons at b_{red}=0.6 for the n-rich (n-deficient) system. The neck size, thus, should not be so large and, consenquently, all phenomena related to the possible compression-expansion of such small nuclear systems should be limited, although still occuring. This is also confirmed by the AMD prediction of fig. 6.9.

The precise reproduction of the details of these results is out of the scope of this thesis. As said, indeed, we are limited by the very CPU-expensive AMD calculations with associated relatively small statistics. Also, we are aware of the problem of the somehow overlapping model usage: while the interaction finishes below 130 fm/c (fig. 6.13), AMD continues its job (including possible IMF emission and break-up steps) up to 500 fm/c where a different statistical code is appended (cfr. sec. 4.3): thus, part of the statistical decay is treated in AMD. As a consequence we tried a simplified approach just to gain some qualitative complementary information on the obtained results. Essentially we would like to see if the pure statistical evaporation can give at least an approximate reproduction of the N/Z results for the "more probably" statistical IMF emissions, i.e. those labeled FWD. This part of the study is important also because it gives an estimation, within the AMD model, of the pre-equilibrium emission which can be a good starting point for further analyses of these data.

By means of the time back-tracing procedure, described in sec. 6.4, we went back to the end of the primary interaction and we looked at the average features of the excited QP. This was done for both the QP_R alone and QP_R+IMF channels, as a function of the centrality. The obtained values, which refer to the $^{48}Ca+^{48}Ca$ reaction and are quoted in tab. 6.1; they are used as input for pure "one-shot" GEMINI++ simulations[3], namely simulating the decay of those precise hot nuclei (sources) indicated in the table. For all cases we assumed nuclear spin of 5 $\hbar$ (cfr. sec. 4.3).

[3]For each "one-shot" GEMINI++ simulation we produced 500000 events.

We can propose some comments about values in the tab. 6.1. First we see that the predicted average pre-equilibrium emission (i.e. deficit of nucleons at the t_{split} time) is almost absent in the considered b_{red} range. Less than 2 neutrons are missing even at $\overline{b_{red}}$=0.6. This result is very difficult to be compared with (very rare) data or other semi-empirical estimations. We can say that the attempts made on ^{58}Ni+^{58}Ni at 52 MeV/u [21] or on ^{64}Zn+^{64}Zn at 45 MeV/u [22] report mid-velocity emissions (probably a part of the pre-equilibrium in general sense) containing from 0.2 to 3 neutrons from roughly peripheral to central collisions. A second comment concerns the fact that primary QP, when emitting an IMF, on average gained more excitation energy and net mass. This is fully consistent with the idea that, by fluctuation, a net transfer of a cluster (or independent nucleons) on the QP, favours a more heavy disassembly than on average (of course the same opposite fluctuations lead to the same conditions for the here neglected QT, by symmetry). A final comment is related to the range of validity of GEMINI++. Looking at the values in tab. 6.1, we see that the energy densities can be above a safe limit for the evaporation framework modeled in this code (around 3 MeV/u) [74]. We must remind this aspect because, even if other authors used GEMINI to predict the decay of nuclei at very high excitation, though this limit must be considered.

Now we can comment the results of the pure "one-shot" evaporation calculation reported in fig. 6.15. The first observation concerns the QP$_R$ alone points. The $\langle N/Z \rangle$ decreases as a consequence of increasing excitation energies (see tab. 6.1) and the final nuclei approach the EAL value (EAL$_{Z=20}$=1.12) from the top. On an absolute scale, the naive modeling here discussed produces too n-p symmetric final products, due to either a too high initial excitation or too high initial neutron abundance. We verified that similar GEMINI spot calculations for the neutron deficient ^{40}Ca nucleus give an opposite trend with N/Z approaching the EAL from the bottom. Almost the same values are obtained in the case of IMF emission for the QP$_R$ while, notably, the IMF are more n-p asymmetric reaching N/Z values above 1.22. The important fact, to our opinion, is that the gap between the IMF and the partner QP is rather well consistent with the data (fig. 6.14(a)). Even not a proof, this supports the idea that IMF FWD emitted have a more statistical nature and the neutron enrichment of the IMF BWD emitted has a different origin from a region experiencing a net neutron gain at mid-velocity.

We now come to the last point concerning the isospin contents of the breakup pairs in the two reactions. The neutron to proton ratio of the Light Fragment (LF) and Heavy Fragment (HF) are shown as a function of $\overline{b_{red}}$, again divided in the BWD and FWD configurations. Results are reported in fig. 6.16(a,b) for the ^{48}Ca and ^{40}Ca systems, respectively. Symbols are according to the legend. The two panels have not the same y-range, but same y scale, because we want here to stress the effects in the ^{40}Ca system. For the n-rich system we do not see any clear signal except the important split for the LF according to their emission direction: when they are emitted BWD they are more neutron rich, as found for the IMF and as well recorded in literature. This, again, is compatible with the hypothesis of a neutron enrichment of the mid-velocity region. However, looking at the heavy partner, no clear isotopic anti-correlation is found in the two opposite velocity orientation. Also, as for the IMF case, the isotopic content is basically independent of

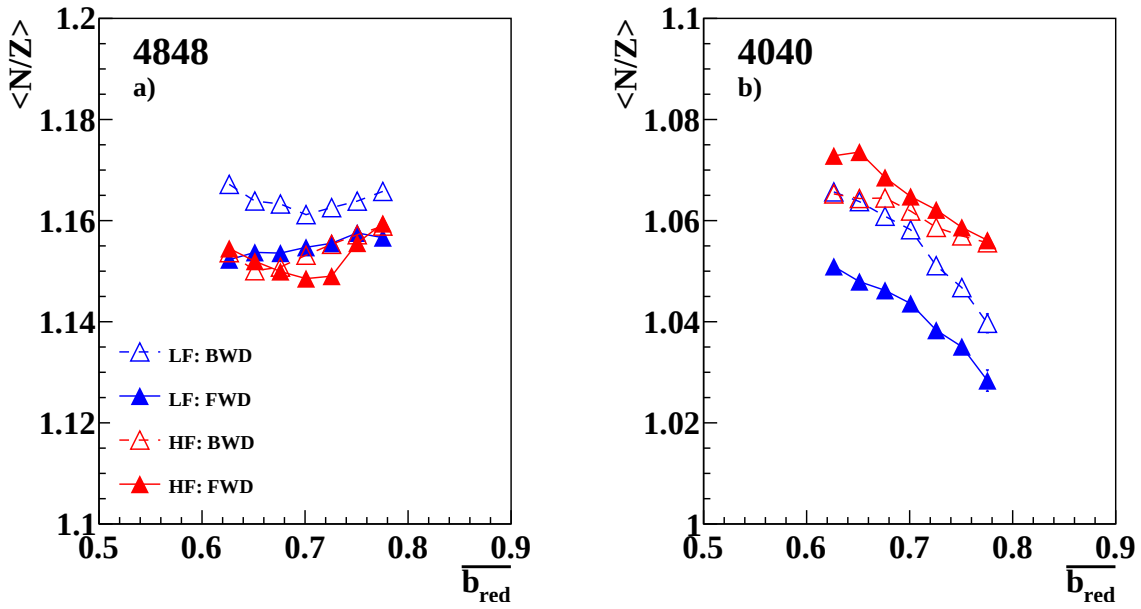

Figure 6.16: *Neutron to proton ratio as a function of $\overline{b_{red}}$ for both the Heavy Fragment (HF) and Light Fragment (LF) in the QP_B channel, separating BWD and FWD emissions (see text). Symbols according to the legend. Panel a) $^{48}Ca+^{48}Ca$, Panel b) $^{40}Ca+^{40}Ca$ reaction.*

the impact parameter.

A more evident scenario appears looking at the ^{40}Ca reaction although, as expected, all detected fragments are more symmetric being all $\langle N/Z \rangle$ values less than 1.08. First we must note that the LF are less neutron rich than the HF. This inversion is not surprising since most the breakup pairs contain, as LF, a Carbon or an Oxygen ions: the isotopic distributions of such ions tend to be rather symmetric being dominated by ^{12}C and ^{16}O[24, 25, 102]. On the other hand the neutron enrichment of BWD emitted IMF is still larger than for FWD emission in full agreement with the other cases. Very importantly here we can appreciate the anti-correlation with the partner: when the LF are BWD emitted and are more n-rich, then the coincident HF are more neutron deficient and vice versa. An other observation can be done: the FWD-BWD gap tends to increase by moving towards more violent collisions, probably, as said, due to the increase of the isospin drift contribution towards a larger dilute region. Again we guess that the anti-correlation is reduced in ^{48}Ca by the initial neutron richness and by the possible free neutron pre-equilibrium (at least in the sense that they are emitted before or during the breakup process).

We remind that in fig. 6.16 we are summing over all breakup asymmetries; as a consequence some of the correlations can be diluted when considering the average behavior. Also, from the figure, we cannot judge how the asymmetry of the breakup evolves with the impact parameter. Therefore, as a last attempt, we tried to isolate, only for the more promising ^{40}Ca reaction, some specific partners for events producing an IMF or a breakup.

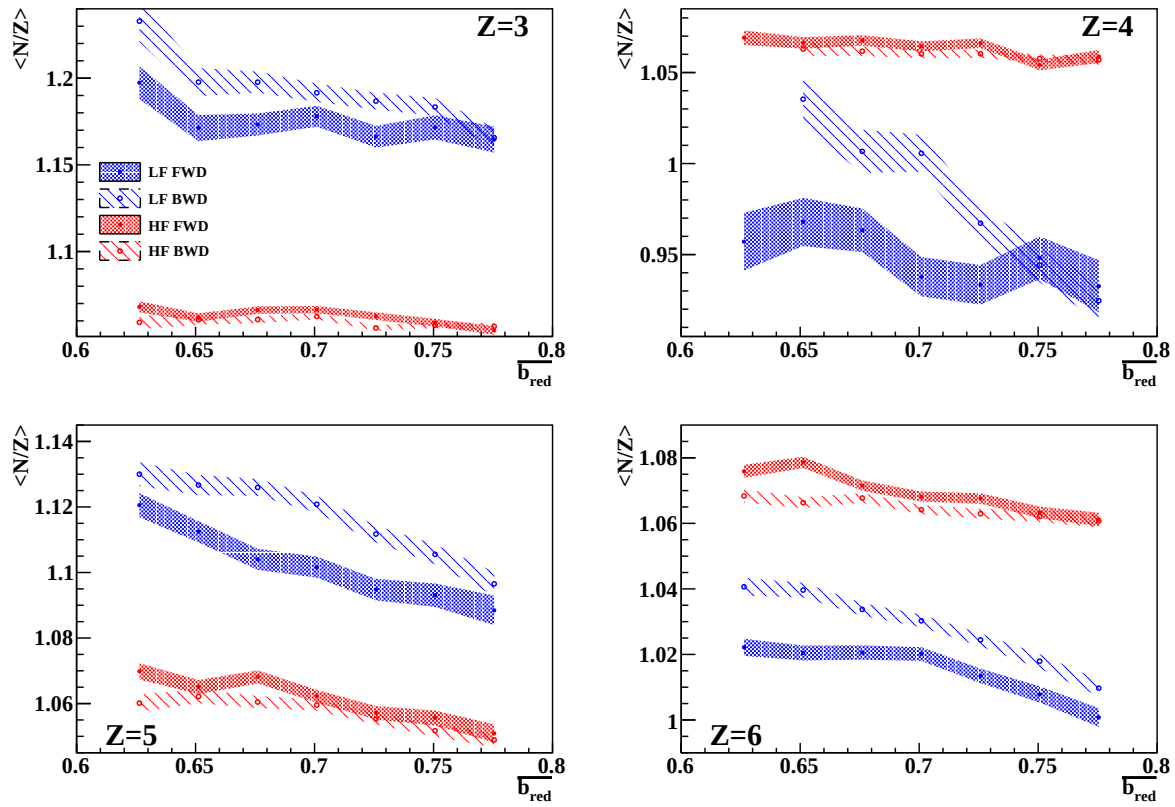

Figure 6.17: *Experimental $\langle N/Z \rangle$ for selected light elements detected in coincidence with a QP. The data refer only for the ^{40}Ca reaction. Each panel reports the $\langle N/Z \rangle$ in the usual bin of $\overline{b_{red}}$ for the indicated element and for the coincident heavy partner. Statistical errors are represented by the band width.*

Fig. 6.17 reports on the results for the separate cases in which we detect a fragment with $Z = 3$, 4, 5 and 6; each panel shows the result for the indicated selected element. This is in general the LF of the QP decay. The resulting scenario is quite clear, even considering that for each light fragment we integrate over the (expected narrow) size distribution of the heavy one. In all cases we observe that fragments emitted BWD are more neutron rich than when emitted in the QP direction. The gap is small at the largest $\overline{b_{red}}$ and grows with centrality. The effect is quite large for Be, because the lack of ^{8}Be (due to the immediate decay in two alphas) enhances the jump from ^{7}Be e ^{9}Be or heavier isotopes. Finally, in a clear and elegant way, we put in evidence the isospin anti-correlation between light and heavy fragment, depending on their emission polarization.

We can thus conclude this section, claiming a well demonstrated evidence of neutron enrichment of clustered matter towards mid-velocity, anti-correlated with the neutron depletion of the donor fragments, even in these relatively small systems, where probably only a rather small dilute neck is formed. However, the fact of investigating a so neutron-deficient reaction combined with optimum detectors and refined analyses, permit to clearly demonstrate the associated effects. These results are promising about next experiments

with the FAZIA detectors, possibly coupled to large acceptance centrality-selector arrays (as INDRA at GANIL). Indeed one could attempt some very strict detailed balance not only of the N/Z ratio of fragments but also of the total mass and charge of the sources, expecially for $N = Z$ (or anyhow n-deficient) systems where free neutron emission is strongly reduced.

SUMMARY AND CONCLUSIONS

This thesis is part of the studies that the international FAZIA collaboration is performing on heavy ion collision experiments using the new setup of telescopes developed in the last decade, capable of excellent capabilities in term of ion identification. In this thesis we analyzed the data of Ca+Ca reactions, collected in one of the first experiments using the new FAZIA telescopes, *i.e.* ^{48}Ca+^{48}Ca and ^{40,48}Ca+^{40}Ca. The beams were accelerated at 35 MeV/u, well within the so called Fermi energy range. The main goal of the experiment was an accurate study of the peripheral and semi-peripheral collisions in particular from the point of view of the mechanisms that intervene in the neutron-to-proton equilibration. Indeed, Ca ions allow to span, with stable species, a rather large range of isospin, from 1 up to 1.4 for the n-deficient and n-rich reactions, respectively. In this thesis, how it is commonly done in this field [24, 62, 102], the isospin is measured with the N/Z ratio of the nuclei.

This thesis was exactly motivated by the purpose of study, with our powerful new apparatus, the isospin dynamics (cfr. chap 1) exploiting a proper combination of Ca isotopes, both as beams and targets. The two symmetric systems represent the limiting scenarios for the neutron rich and neutron deficient system. In either case the isospin diffusion is absent thus these symmetric reactions are an optimum playground to highlight isospin drift, if present [3, 14]. On the other hand, the mixed system, ^{48}Ca+^{40}Ca, is the candidate to study the isospin equilibration, provided that we can follow the trend of isospin related variables *vs.* the reaction centrality [4]. For this purpose, it is of special value the use of the imbalance ratio, a variable introduced years ago in order to evidence the isospin diffusion [8, 9]. Indeed this quantity, that implies the measurements of a combination of at least three systems at the same energy (as we did), allows to reduce the effect of any other unwanted process but the n-p equilibration itself. The data refer to the "Quasi-Projectile", QP, phase-space covered by our detector. Similarly to most other published cases, the Quasi-Target phase-space is almost undetected so that it has been neglected in our analysis.

All above considered, the following golden points of this experimental work should be remarked. The use of the FAZIA telescopes (chap. 2) permits to study isospin dynamics

not only from the footprints offered by the particles and light fragments as very often done in the past. Here, we indeed extend the analysis to the major reaction products, *i.e.* the QP and the QP breakup fragments in coincidence, as underlined by the FAZIA-SYM scientific goal in chap. 3. This is one of the main experimental advance permitted by the new telescopes and strongly chased in our analysis. The set of reactions with Ca isotopes allows the maximum span of N/Z from 1 to 1.4, and moreover, it is the first time, to our knowledge, that isospin drift has been studied accurately in a $N = Z$ system, as ^{40}Ca. The comparison of experimental findings with extensive simulations based on one of the best reaction models, presented in chap. 4, in the world (AMD [10]) is an essential part of the thesis. Such a comparison helps in guiding our event selections (chap. 5) and permits to draw some conclusions on the observed phenomena.

After going through the data reduction phase, described in chap 3, the main achievements and findings of this thesis are amply reported in chap. 5 and chap. 6. Here we summarize them.

We accurately selected the various channels related to QP and we show their main features. The most populated channels is the evaporative one, with a QP remnant left after the decay; the other two cases are the QP accompanied also by one intermediate mass fragment (IMF, $Z = 3$ and 4 in our definition) and the QP which fragments in two comparable pieces (QP breakup). These two cases are only of the order of percent of the only evaporative channel. The emission of an IMF can be view as a limiting case of the breakup. The AMD code [10], followed by the necessary statistical evaporative phase (GEMINI++ code [74]), quite well reproduces many measured distributions. It also predicts rather well the branching ratios of the three channels and the multiplicities of charged particles and fragments. Globally, the agreement with data is better for the neutron deficient system. The features of the breakup scenario are worse predicted, in particular the model fails the mass and charge asymmetry. In any case the capability of the model to reproduce many observables encourages us to use it to study specific details of the nEoS.

Notwithstanding the relatively small coverage of the setup[4] (polar angle form 2° to 8° in the laboratory frame), we built and used an impact parameter estimator, controlled with the AMD simulations and also proven with specific experimental checks (sec. 6.1). This step is of paramount relevance to study the isospin dynamics and, however, we must underline that this is not often performed in published data: some findings (even important) are presented without a clearly attempted impact parameter estimation. The limited acceptance of the detector and the intrinsic spread of most variable towards head-on collisions, prevent us to extend our analysis toward central collisions.

As for isospin equilibration, the expected relaxation of this degree of freedom has been observed in the mixed system, via the use of the imbalance ratio of the variable N/Z. The neutron content of the QP remnant from ^{48}Ca projectile is modified by the interaction with ^{40}Ca since the observed most peripheral collisions. Moving toward centrality we found initially a rather slow relaxation and then a faster trend to the equilibrium

[4]We remind that we deal with one of the first experiments made with an incomplete FAZIA device.

value (cfr. sec. 6.2). The AMD+GEMINI model also shows the isospin equilibration which however proceeds at a more smooth pace towards equilibrium from peripheral to semi-central reactions. Within the model we used two prescriptions about the symmetry energy dependence; an asy-soft and an asy-stiff were tested corresponding to two different repulsive field for neutrons at low densities. These two prescriptions can have an impact in the details of isospin diffusion. Importantly we observed no difference in the behavior of the predicted N/Z imbalance ratio in the two cases. This suggests the fact that, within the model, the interacting system does not reach significant regions at sub-saturation density, as it would needed to have a sensitivity to disentangle about asy-stiffness (sec. 6.3). In this respect we performed a specific investigation within the AMD output files with the aim to verify the presence of (possible) diluted system parts, i.e. at densities below the saturation value. We qualitatively discovered that indeed these parts can be formed but in any case they are quite small not having the shape of a well defined neck bridging the two QP-QT main nuclei.

For the first time to our knowledge, the imbalance ratio method has been applied for three channels related to QP in a quite coherent and homogeneous way (sec. 6.4). Remarkably, we find that the measured trend is basically the same whatever the final QP channel (remnant or split); this suggests that the interaction times are essentially the same; the model prediction supports this argument because it indicates interaction times equal within 15 fm/c for the three channels.

Concerning mid-velocity emissions, we carefully examined the data of the two symmetric systems, where no net isospin diffusion should occur. Our study puts in evidence the the neutron enrichment for fragments emerging at velocities in between those of the QP and QT and the neutron depletion of corresponding partner. The effects are small due to the small size of the systems, but they persist more in the ^{40}Ca+^{40}Ca than for ^{48}Ca+^{48}Ca reaction. Indeed, in the n-rich system one can imagine a larger abundance of neutrons in the mid-velocity region favored by the neutron skin of ^{48}Ca nuclei and by isospin drift. This hot asymmetric nuclear system can emit unbound neutrons rapidly lowering the N/Z of the species, so that only the smallest IMF keeps memory of the initial asymmetry. Instead a clear signal persist in the $N = Z$ ^{40}Ca+^{40}Ca system; due to the lack of neutrons, it preserves more the anti-correlation between the neutron enrichment of the fragment at mid-velocity and the neutron depletion of the donor QP. Remarkably, we followed this effect as a function of the reaction centrality, pointing out a neutron enrichment more effective moving towards central collisions, where the neck formation probability and/or size are deemed to grow, and consequently the effects due to a possible density gradient.

In conclusion, in this thesis we presented a detailed analysis of Ca+Ca reactions at 35 MeV/u exploiting four blocks of the FAZIA multi-telescope array, which allowed the complete isotopic identification of QP fragments. Such analysis opened the path towards the INDRA+FAZIA experimental campaign in GANIL, in which both the angular acceptance of the INDRA multi-detector, and the high isotopic resolution of FAZIA are combined. This coupling will allow to investigate both isospin diffusion and isospin drift mechanisms covering a larger solid angle and, in particular up to almost head-on collision, so as a complete characterization of isospin transport phenomena will be obtained.

APPENDIX A

CONTAMINANTS ON THE MAIN REACTIONS

In this Appendix we will deal with the background reaction due the target carbon backing and with the Al target frame. In order to try to estimate their effect on the main reaction (namely ^{48}Ca+^{48}Ca), sufficiently long runs have been performed for the following reaction: approximately 4 and 1 millions events for ^{48}Ca on ^{12}C 300 μm thick and ^{48}Ca+empty frame, respectively. In particular we will look at ions identified both in charge and mass, as this more complete sample of events has been used for the analysis.

A.0.1 Reaction on the target carbon backing

The charge *vs.* parallel velocity in the laboratory frame correlations for the carbon background reactions is presented presented in fig. A.1(a), together with the main Ca+Ca data for a quick comparison. Each distribution is normalized to unitary integral. The magenta arrow, in fig. A.1(a), labelled as v^*_{cm} points at the respective CM velocity, while v_{cm} always indicates the CM velocity of the ^{48}Ca+^{48}Ca system. We observe that data for ^{12}C look very similar to those of the ^{48}Ca+^{48}Ca system. Same charge and parallel velocity regions are populated, between 60 mm/ns and v_{beam}, for fragment with $Z \geq 12$.

We remind that Ca targets was sandwiched between two carbon layers, in a three layer configuration of thickness 10−500−10 μg/cm^2 respectively. In order to perform the correct subtraction of the ^{12}C contaminants, we aim to estimate the ratio between the reaction number with the carbon backing N_C and the total reaction number with the sandwiched target N_{TOT}. For a charge Q impinging on the sandwiched target, N_{TOT} can be evaluated as:

$$N_{TOT} = N_a Q \left(\sigma_{Ca} \frac{T_{Ca}}{M_{Ca}} + \sigma_C \frac{T_C}{M_C} \right) \tag{A.1}$$

where, σ_{Ca} and σ_C are the reaction cross section of the impinging beam on Ca and C target, T_{Ca} and T_C the sandwiched target thicknesses and M_{Ca} M_C the molar mass of Ca and C; N_a is the Avogadro number. To obtain the quantity N_C we can use the reaction on the pure ^{12}C target 300 μg/cm^2 thick. In particular, the ratio between the number of

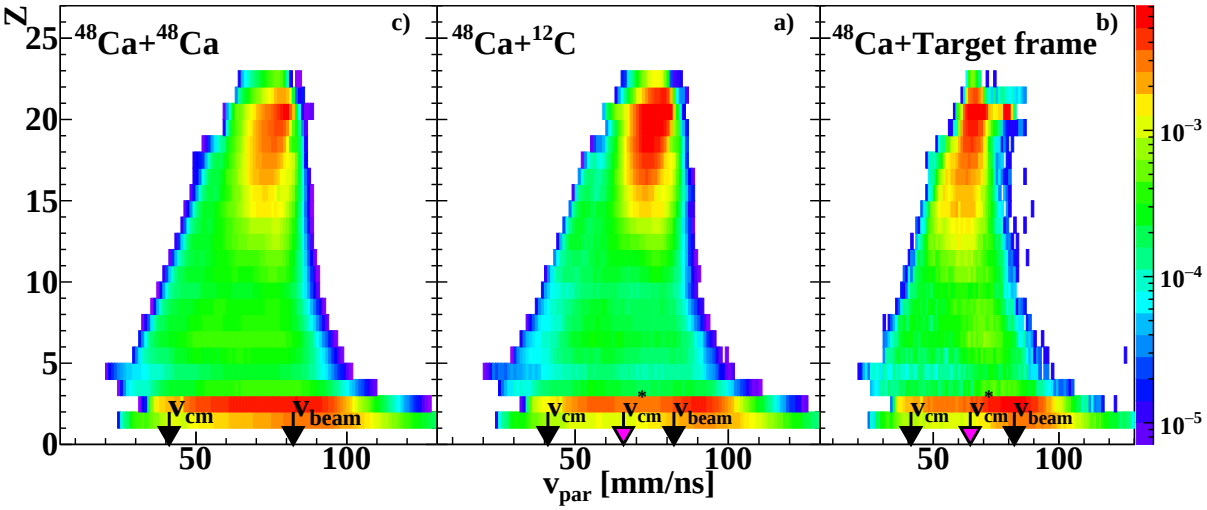

Figure A.1: *Charge v.s. parallel velocity in the laboratory frame correlation for the ions identified in charge and mass. Each panel refers to different reaction according to the legend. Each distribution is normalized to unitary area.*

reactions with the ^{12}C pure target ($N_{C'}$) and the number of reactions with the carbon backing N_C can be estimated as:

$$\frac{N_{C'}}{N_C} = \frac{Q_{C'}T_{C'}}{QT_C} \tag{A.2}$$

where $Q_{C'}$ is the charge impinging on the ^{12}C and $T_{C'}$ its thickness. Thus combining eq.(A.1) and eq.(A.2) we obtain:

$$\frac{N_C}{N_{TOT}} = \frac{1}{1 + \frac{\sigma_{Ca}T_{Ca}M_C}{\sigma_C T_C M_{Ca}}} \tag{A.3}$$

Thus, calculating the reaction cross section from a pure geometrical model[1], we obtain a percentage of carbon backing event in the total acquired sample of 9%.

Fig. A.2 shows the charge distribution for the ^{48}Ca+^{48}Ca and ^{48}Ca+^{12}C systems[2], according to the legend. The ^{48}Ca+^{48}Ca charge distribution is normalized to unitary area, while the ^{48}Ca+^{12}C one is scaled by the carbon percentage in the Ca target, to show the relative contribution to the total distribution. Subtracting the latter to the former we obtain the distribution shown with green lines.

Comparing the results before and after the subtraction we observe that the influence of the carbon backing in the main reaction seems to be negligible (according to the percentage of carbon in the target). Of course, it's impossible to disentangle event by

[1] $\sigma_{reac} = \pi b_{gr}^2$, where b_{gr} is the grazing impact parameter.
[2] Both are obtained projecting on the y-axis the correlations of fig. A.1(c,a).

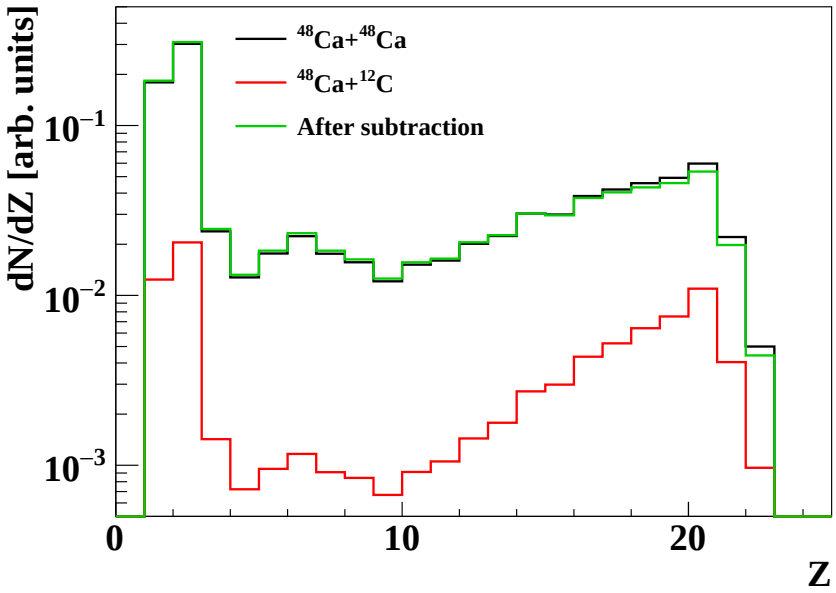

Figure A.2: *Charge distribution for the ^{48}Ca+^{48}Ca and ^{48}Ca+^{12}C reactions. ^{48}Ca+^{12}C distribution has been scaled according to the ^{12}C percentage in the ^{48}Ca target. Green line represents the distribution after the subtraction.*

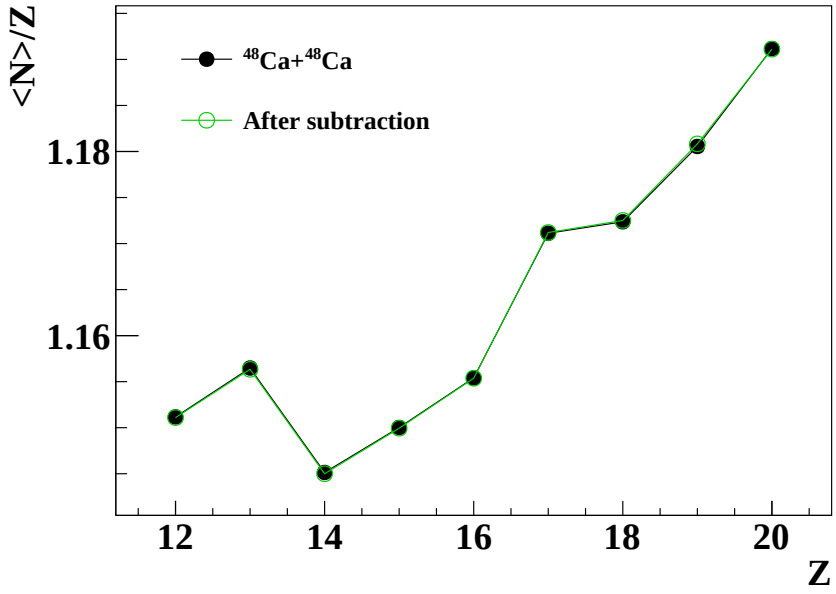

Figure A.3: *Average neutron number per charge unit as a function of the charge of the QP remnants. Black dots for the ^{48}Ca+^{48}Ca, green lines after the subtraction of the ^{48}Ca+^{12}C background.*

event the two reactions, but the results obtained seems to show that the carbon backing does not bias the ^{48}Ca+^{48}Ca results.

However, this estimation is based on a very inclusive sample. According to the FAZIA-SYM scientific goal (cfr. sec.3.1), in the analysis presented in chap. 5 and chap. 6 two main event selections have been investigated: the first contains the detection of the QP remnant, the second ascribable to QP break up events (cfr. sec. 5.1). Considering the selection efficiencies of such channels for both the ^{48}Ca+^{48}Ca and ^{48}Ca+^{12}C system we obtain a further reduction factor of 0.8 and 0.1, respectively. Thus the percentage of polluting events is about 7% and less than 1% in the QP remnant and QP break up selection. We verified that the presence of this background do not bias the events within the two channels. For instance, fig. A.3 shows the average neutron number of the QP remnants, selected according to the criteria exposed in sec. 5.1. As we can see, the chemistry of the QP remnants is not affected at all by the presence of the ^{12}C target backing, since the average neutron number per charge units of the QP remnants is basically the same before and after the subtraction procedure.

It is worth mentioning that the same targets were also used during the ISO-FAZIA experiment, performed few months before the FAZIA-SYM runs. In ref. [30, 98], the contribution of reaction on carbon ions was estimated taking into account the HIPSE simulation [133, 134]. The results from HIPSE, suggested that the the carbon contamination could be neglected in the analysis. Thus, according to our current estimation, and supported by the conclusion of [30], we can neglect in the analysis the carbon backing contribution.

A.0.2 Reaction on the Al target frame

We can finally deal with the spurious reactions on the thick Al target frame (approximately 0.5 mm). First of all a procedure as that described in the previous section cannot be applied. Indeed, the effective current impinging on the Al target frame can not be evaluate and consequently no subtraction can be attempted.

$$N_{TOT} = N_a \left(Q\sigma_{Ca}\frac{T_{Ca}}{M_{Ca}} + Q'\sigma_{Al}\frac{T_{Al}}{M_{Al}} \right) \tag{A.4}$$

where $Q = It$ is the charge deposited by the main beam current I in a time t, while $Q' = I't$ is the charge deposited by the beam impinging on the Al target frame I' in the same interval. Since the current I' is not known any subtraction procedure cannot be attempted. We can only hypothesize that if we are dealing with a faint beam halo its current I' can be much smaller than the main beam current I.

However, part of those events corresponding to ^{48}Ca (in)elastic scattering can be directly see from the Si1-Si2 ΔE-E matrices. Fig. A.4 shows the ΔE-E correlation obtained from the silicon layers of the telescope 211, where such events are particularly visible. The $Z = 20$, $A = 48$ locus is shown with red contour. It identifies ^{48}Ca ions ions elastically scattered by the thick Al target frame. Due to the target frame thickness such events are

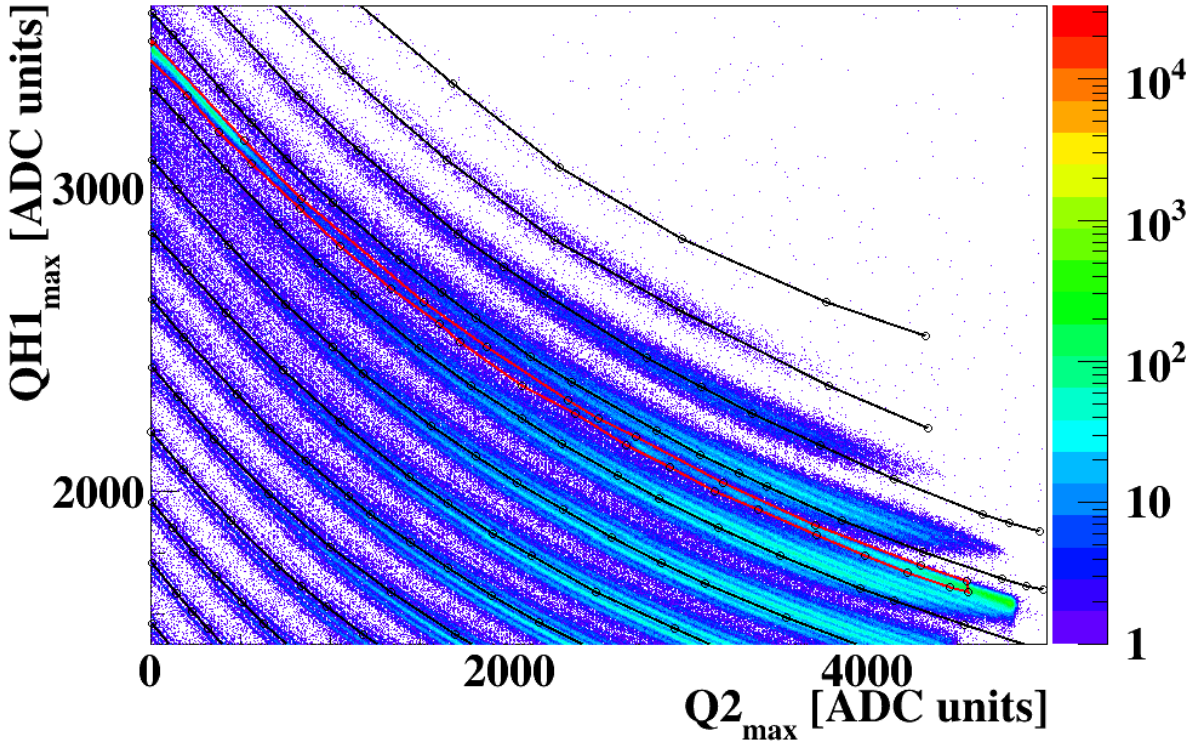

Figure A.4: *Si1-Si2 ΔE-E matrix for the telescope 211. The red contour contains events of ^{48}Ca elastically scattered by the Al target frame. The y-axis origins is suppressed in order to better show the region of interest.*

broaden in energy, as the beam losses energy crossing the target frame. By means of of graphical cuts such events are easily removed from the ΔE-E Si1-Si2 matrices, as they are separated by the other Ca isotopes. As anticipated (see fig. 3.11 in sec. 3.5) also in PSA matrix in Si1 similar effects are visible, but they cannot be removed with graphical cuts as the $Z = 20$ line is not isotopicaly resolved. However, as mentioned, they are cut once the isotopic identification of the ions is requested (see fig. 3.11).

Eventually fragments produced in the reaction between the beam and the Al target frame could lay in correspondence of the experimental line of lower Z, thus a graphical contour cannot help to cut them out.

In order to get some estimation of this background, we can look at the charge *vs.* parallel velocity correlation of the acquired events with the empy target frame. It is shown in fig. A.1(b). Reaction with the Al target frame is quite different with respect to that of ^{48}Ca+^{48}Ca (fig. A.1(c)). This is largely due to the fact that the Al frame is a thick target and that it is hit by a beam halo with characteristics and details which are not known. For sure there is track of some elastic scattering for $Z = 20$ and large velocities ($\approx v_{beam}$) but the main contribution is related to strongly energy degraded Ca ions, with velocities from 70 mm/ns downward. As a consequence of this thick-target effects one can

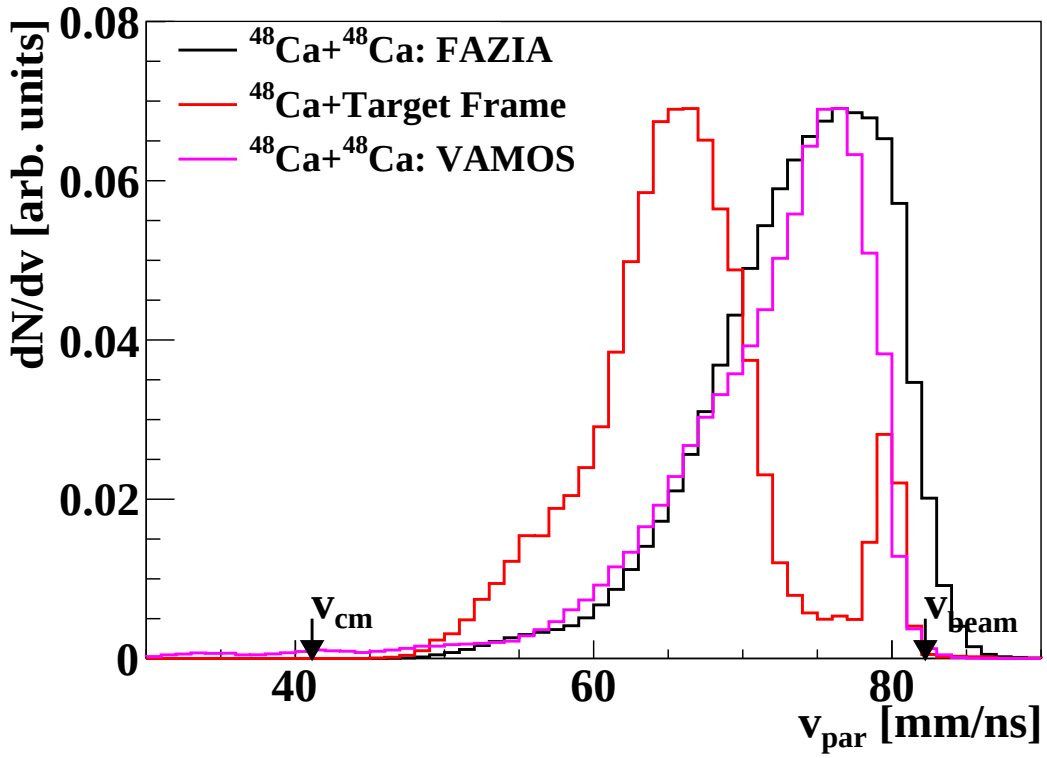

Figure A.5: *Parallel velocity distribution for $Z \geq 10$. Colors according to the legend: in particular magenta line represents the results obtained by the INDRA+VAMOS experiment for the ^{48}Ca+^{48}Ca system. All the distributions are normalized to the maximum of the black distribution.*

have degraded Ca ions scattered into the telescopes and also ions produced in nuclear reactions on Al nuclei which can be produced at any stage of the beam penetration in the Al material. In any case, either because the beam is degraded and produces a low energy reaction on Al, either because the beam interacts early in the frame but then the reaction products are slowed down by the rest of the foil, the background events should mainly contribute at low velocities, say below the value 70 mm/ns corresponding to the yield maximum for $Z = 20$.

Starting from this observation, in fig. A.5 the v_{par} distribution is shown for ions with $Z \geq 10$ mostly corresponding to fragments originated from QP decay and where the bkg could be significant.

Comparing the black and red distributions, it is not easy to evince how and if the reactions with the target frame bias the the reaction with the ^{48}Ca target. However, we can observe that the distribution for the ^{48}Ca+^{48}Ca system is smooth, and it does not show any clear structure attributable to the background, especially at $v_{par} \leq 70$ mm/ns where the yield of the reaction on the empty frame is large. One can question about the shoulder visible in the data at $v_{par} < 60$ mm/ns, for the reaction both on the ^{48}Ca and

on the empty frame. However, as observed in independent papers [110], it corresponds to the QP break up channel. When the excited QP breaks up in two fragments, at forward angles one can observe a bimodality in the parallel velocity distribution: a lobe due to the fragment emitted towards the center of mass, another lobe at parallel velocity closer to the beam one [14, 123, 135].

The previous arguments are qualitative and do not prove that the background due to the spurious reactions on the target frame are really negligible. A better and stronger support in this direction has been found using the experimental data of ^{48}Ca+^{48}Ca data measured with the INDRA+VAMOS experiment, which have been specifically analyzed in order to independently verify the similarity of the two experimental cases. Since in the VAMOS data the beam optics was good and no background from target frame was reported, the similarity of the results in the two cases would confirm that also in our experiment at LNS the effects of the frame, if any, would be negligible. The parallel velocity distribution measured with VAMOS, for fragments $Z \geq 10$ is shown in fig. A.5 with magenta line: it is normalized to the maximum of the FAZIA distribution. Globally VAMOS data looks very similar to ours, thus strengthen our previous observations. The VAMOS data extend to lower v_{par} values than in our case, probably due to the lower energy thresholds for isotopic separation guaranteed by the focal plane detector which has a gas chamber as a first active layer. On the other side the FAZIA data extend to higher parallel velocities: probably, this is due to the trigger condition on the INDRA+VAMOS experiment where the main trigger was the coincidence between the INDRA and VAMOS. Events where only VAMOS detected an ejectile have been acquired downscaled [69]. Such condition bias the events toward more dissipative collision with respect the FAZIA data, thus lacking on the more peripheral reactions.

In conclusions, both the analysis of our data for the Ca reaction on the blank frame and the comparison with the data of INDRA+VAMOS, strongly suggest that the background of the reactions on the target frame due to the bad beam optics has a very slight impact on the distributions of the here studied Ca+Ca collisions.

ACKNOWLEDGMENT

This work required the use of a lot of computation time for the production of the simulated data. We would like to thank the GARR Consortium for the kind use of the cloud computing infrastructure on the platform cloud.garr.it. We would like to thank also the INFN-CNAF for the use of its cloud computing infrastructure. Finally, we would like to thank the INDRA Collaboration for let us compare the FAZIA-SYM data with that of the INDRA+VAMOS experiment.

BIBLIOGRAPHY

[1] D. Durand et al., *Nuclear dynamics in the nucleonic regime*, Series in Fundamental and Applied Nuclear Physics (Taylor & Francis, 2000).

[2] J. Łukasik et al., Phys. Rev. C **55**, 1906 (1997).

[3] R. Lionti et al., Physics Letters B **625**, 33 (2005).

[4] V. Baran et al., Physics Reports **410**, 335 (2005).

[5] J. Margueron et al., Phys. Rev. C **97**, 025805 (2018).

[6] P. Napolitani et al., Phys. Rev. C **81**, 044619 (2010).

[7] The FAZIA Collaboration et al., Eur. Phys. J. A **50**, 47 (2014).

[8] F. Rami et al., Phys. Rev. Lett. **84**, 1120 (2000).

[9] M. B. Tsang et al., Phys. Rev. Lett. **92**, 062701 (2004).

[10] A. Ono et al., Progress of Theoretical Physics **87**, 1185 (1992).

[11] R. Charity et al., Nuclear Physics A **483**, 371 (1988).

[12] D. Durand, Nucl. Phys. A **630** (1998).

[13] S. Piantelli et al., Phys. Rev. Lett. **88**, 052701 (2002).

[14] A. Jedele et al., Phys. Rev. Lett. **118**, 062501 (2017).

[15] C. Bertulani et al., *Introduction to nuclear reactions*, Graduate Student Series in Physics (Taylor & Francis, 2004).

[16] K. Krane, *Introductory nuclear physics* (Wiley, 1987).

[17] B.-A. Li et al., Physics Letters B **727**, 276 (2013).

[18] H. Madani et al., Phys. Rev. C **51**, 2562 (1995).

[19] R. Planeta et al., Phys. Rev. C **38**, 195 (1988).

[20] M. B. Tsang et al., Phys. Rev. Lett. **102**, 122701 (2009).

[21] D. Thériault et al., Phys. Rev. C **71**, 014610 (2005).

[22] D. Thériault et al., Phys. Rev. C **74**, 051602 (2006).

[23] I. Lombardo et al., Phys. Rev. C **82**, 014608 (2010).

[24] S. Barlini et al., Phys. Rev. C **87**, 054607 (2013).

[25] A. Rodriguez Manso et al., Phys. Rev. C **95**, 044604 (2017).

[26] P. M. Pizzocchero, arXiv:1609.07587 (2016).

[27] J. Margueron et al., Phys. Rev. C **97**, 025806 (2018).

[28] B. K. Harrison et al., *La structure et l'evolution de l'univers* (Brussels: Stoops, 1958).

[29] S. Valdre et al., Nuclear Instruments and Methods in Physics Research Section A: Accelerators, Spectrometers, Detectors and Associated Equipment **930**, 27 (2019).

[30] G. Pastore, PhD thesis (Università degli Studi di Firenze, 2017).

[31] J. Pouthas et al., Nucl. Instr. and Methods A **357**, 418 (1995).

[32] G. Pausch et al., Nucl.Instr.and Methods A **349**, 281 (1994).

[33] G. Poggi et al., Nucl. Instr. and Methods A **119**, 375 (1996).

[34] L. Bardelli et al., Nucl. Instr. and Methods A **605**, 353 (2009).

[35] L. Bardelli et al., Nucl. Instr. and Methods A **654**, 272 (2011).

[36] G. F. Knoll, *Radiation detection and measurement* (Wiley, 2010).

[37] L. Bardelli et al., Nucl. Instr. and Methods A **602**, 501 (2009).

[38] `www.cismst.org`.

[39] `https://www.fbk.eu/it/`.

[40] L. Bardelli et al., Nucl. Inst. and Methods A **560**, 524 (2006).

[41] G. Pastore et al., Nucl. Instr. and Methods A **860**, 42 (2017).

[42] T. Kurahashi et al., Nucl. Instr. and Methods A **422**, 385 (1999).

[43] H. Hou et al., IEEE Transactions on Acoustics, Speech, and Signal Processing **26**, 508 (1978).

[44] `http://wiki.ganil.fr/gap/wiki/Documentation/VXI/CENTRUM`.

[45] `http://wiki.ganil.fr/gap/wiki/GANIL-SPIRAL2-DAQ-Packages-Distribution`.

[46] A. Pagano et al., Nucl. Phys. A **734**, 504 (2004).

[47] I. Lombardo et al., Nuclear Physics B - Proceedings Supplements **215**, Proceedings of the 12th Topical Seminar on Innovative Particle and Radiation Detectors (IPRD10), 272 (2011).

[48] S. Valdré et al., Il Nuovo Cimento, in Proceedings of the International Workshop on Multifragmentation IWM-EC 2018 **041** (2018).

[49] C. Ammerlaan et al., Nuclear Instruments and Methods **22**, 189 (1963).

[50] J. England et al., Nuclear Instruments and Methods in Physics Research Section A: Accelerators, Spectrometers, Detectors and Associated Equipment **280**, 291 (1989).

[51] G. Pausch et al., Nuclear Instruments and Methods in Physics Research Section A: Accelerators, Spectrometers, Detectors and Associated Equipment **322**, 43 (1992).

[52] S. Barlini et al., Nuclear Instruments and Methods in Physics Research Section A: Accelerators, Spectrometers, Detectors and Associated Equipment **600**, 644 (2009).

[53] Pasquali, G. et al., Eur. Phys. J. A **50**, 86 (2014).

[54] D. Gruyer, PhD thesis (Université de Caen Normandie, 2014).

[55] P. Tove et al., Nuclear Instruments and Methods **51**, 261 (1967).

[56] H. O. Neidel et al., Nucl. Inst. and Methods A **212**, 299 (1983).

[57] W. Bohne et al., Nuclear Instruments and Methods in Physics Research Section A: Accelerators, Spectrometers, Detectors and Associated Equipment **240**, 145 (1985).

[58] N. L. Neindre et al., Nucl. Instr. and Methods A **701**, 145 (2013).

[59] S. Carboni et al., Nucl. Instr. and Methods A **664**, 251 (2012).

[60] M. B. Tsang et al., Phys. Rev. Lett. **86**, 5023 (2001).

[61] T. X. Liu et al., Phys. Rev. C **76**, 034603 (2007).

[62] L. W. May et al., Phys. Rev. C **98**, 044602 (2018).

[63] R. D. Souza et al., Nuclear Instruments and Methods in Physics Research Section A: Accelerators, Spectrometers, Detectors and Associated Equipment **295**, 109 (1990).

[64] E. Galichet et al., Phys. Rev. C **79**, 064614 (2009).

[65] G. A. Souliotis et al., Phys. Rev. C **73**, 024606 (2006).

[66] G. A. Souliotis et al., Phys. Rev. C **90**, 064612 (2014).

[67] S. Pullanhiotan et al., Nucl. Instr. and Methods A **593**, 343 (2008).

[68] M. Rejmund et al., Nuclear Instruments and Methods in Physics Research Section A: Accelerators, Spectrometers, Detectors and Associated Equipment **646**, 184 (2011).

[69] Q. Fable, PhD thesis (Université de Caen Normandie, 2018).

[70] Wigg, P.C. et al., EPJ Web of Conferences **31**, 00015 (2012).

[71] Boisjoli, M. et al., EPJ Web of Conferences **31**, 00040 (2012).

[72] A. Ono, Phys. Rev. C **59**, 853 (1999).

[73] A. Ono, Journal of Physics: Conference Series **420**, 012103 (2013).

[74] R. J. Charity, Phys. Rev. C **82**, 014610 (2010).

[75] S. Piantelli et al., Phys. Rev. C **99**, 064616 (2019).

[76] https://cc.in2p3.fr.

[77] http://indra.in2p3.fr/kaliveda/.

[78] https://root.cern.ch.

[79] C. Frosin et al., accepted by Nucl. Inst. and Methods A.

[80] http://indra.in2p3.fr/kaliveda/KVedaLossDoc/KVedaLoss.html.

[81] F. Hubert et al., Atomic Data and Nuclear Data Tables **46**, 1 (1990).

[82] http://www.srim.org.

[83] M. Pârlog et al., Nuclear Instruments and Methods in Physics Research Section A: Accelerators, Spectrometers, Detectors and Associated Equipment **482**, 674 (2002).

[84] M. Pârlog et al., Nuclear Instruments and Methods in Physics Research Section A: Accelerators, Spectrometers, Detectors and Associated Equipment **482**, 693 (2002).

[85] G. Casini et al., LNL Annual Report.

[86] D. Dell'Aquila et al., Nuclear Instruments and Methods in Physics Research Section A: Accelerators, Spectrometers, Detectors and Associated Equipment **929**, 162 (2019).

[87] L Morelli et al., Journal of Physics G: Nuclear and Particle Physics **43**, 045110 (2016).

[88] B. Borderie et al., Physics Letters B **755**, 475 (2016).

[89] L. Morelli et al., Phys. Rev. C **99**, 054610 (2019).

[90] www.nndc.bnl.gov/nudat2/.

[91] A. Camaiani et al., Phys. Rev. C **97**, 044607 (2018).

[92] M. Colonna et al., Nuclear Physics A **642**, 449 (1998).

[93] P. Napolitani et al., Physics Letters B **726**, 382 (2013).

[94] A. Ono et al., Phys. Rev. C **53**, 2958 (1996).

[95] N. Ikeno et al., Phys. Rev. C **93**, 044612 (2016).

[96] G. Tian et al., Phys. Rev. C **95**, 044613 (2017).

[97] G. Tian et al., Phys. Rev. C **97**, 034610 (2018).

[98] S. Piantelli et al., Phys. Rev. C, submitted.

[99] E. Chabanat et al., Nuclear Physics A **627**, 710 (1997).

[100] D. D. S. Coupland et al., Phys. Rev. C **84**, 054603 (2011).

[101] O. Lopez et al., Phys. Rev. C **90**, 064602 (2014).

[102] De Filippo, E. et al., Phys. Rev. C **86**, 014610 (2012).

[103] W. Hauser et al., Phys. Rev. **87**, 366 (1952).
[104] N. Bohr et al., Phys. Rev. **56**, 426 (1939).
[105] L. G. Moretto, Nucl. Phys. A **247**, 211 (1975).
[106] A. Ono et al., Phys. Rev. C **70**, 041604 (2004).
[107] R. Bass, Nuclear Physics A **231**, 45 (1974).
[108] P. Lautesse et al., Eur. Phys. Journal A **27**, 349 (2006).
[109] P. Eudes et al., Phys. Rev. C **90**, 034609 (2014).
[110] B. Davin et al., Phys. Rev. C **65**, 064614 (2002).
[111] S. Galanopoulos et al., Nuclear Physics A **837**, 145 (2010).
[112] V. E. Viola et al., Phys. Rev. C **31**, 1550 (1985).
[113] S. Piantelli et al., Phys. Rev. C **88**, 064607 (2013).
[114] S. Pirrone et al., EPJ Web of Conferences **11**, 16010 (2011).
[115] I. Lombardo et al., Phys. Rev. C **84**, 024613 (2011).
[116] M. D'Agostino et al., Nucl. Phys. A **861**, 47 (2011).
[117] S. Piantelli et al., Phys. Rev. C **74**, 034609 (2006).
[118] E. Plagnol et al., Phys. Rev. C **61**, 014606 (1999).
[119] S. Valdré et al., Phys. Rev. C **93**, 034617 (2016).
[120] K. Schmidt et al., Phys. Rev. C **95**, 054618 (2017).
[121] S. Wuenschel et al., Nucl. Instr. and Methods A **604**, 578 (2009).
[122] A. B. McIntosh et al., Phys. Rev. C **81**, 034603 (2010).
[123] G. Casini et al., Phys. Rev. Lett. **71**, 2567 (1993).
[124] P. Gippner et al., Zeit. fur Phys. A **330** (1988).
[125] A. Mangiarotti et al., Phys. Rev. Lett. **93**, 232701 (2004).
[126] E. Vient et al., The European Physical Journal A **54**, 96 (2018).
[127] S. Piantelli et al., Phys. Rev. C **76**, 061601 (2007).
[128] R. J. Charity, Phys. Rev. C **58**, 1073 (1998).
[129] M. Papa et al., The European Physical Journal A **39**, 117 (2009).
[130] A. Lefèvre et al., Nuclear Physics A **735**, 219 (2004).
[131] Hudan, S. et al., Eur. Phys. J. A **50**, 36 (2014).
[132] Y. Larochelle et al., Phys. Rev. C **62**, 051602 (2000).
[133] D. Lacroix et al., Phys. Rev. C **69**, 054604 (2004).
[134] D. Lacroix et al., Phys. Rev. C **71**, 024601 (2005).
[135] E. D. Filippo et al., Phys. Rev. C **71**, 064604 (2005).